DIRECT NUCLEAR HEATING MEASUREMENTS AND ANALYSES FOR PLASMA-FACING MATERIALS

A. KUMAR *University of California, Los Angeles*
School of Engineering and Applied Science
Mechanical, Aerospace, and Nuclear Engineering Department
Los Angeles, California 90095

Y. IKEDA *Japan Atomic Energy Research Institute*
Department of Reactor Engineering, Tokai Research Establishment
Tokai-mura, Naka-gun, Ibaraki-ken 319-11 Japan

M. A. ABDOU and M. Z. YOUSSEF *University of California, Los Angeles*
School of Engineering and Applied Science
Mechanical, Aerospace, and Nuclear Engineering Department
Los Angeles, California 90095

C. KONNO, K. KOSAKO, Y. OYAMA, T. NAKAMURA,
and H. MAEKAWA *Japan Atomic Energy Research Institute*
Department of Reactor Engineering, Tokai Research Establishment
Tokai-mura, Naka-gun, Ibaraki-ken 319-11 Japan

Experimental measurement of nuclear heating rates was carried out in a simulated D-T fusion neutron environment from 1989 through 1992 under the U.S. DOE/JAERI collaborative program at the Fusion Neutronics Source Facility. Small probes of materials were irradiated in close vicinity of a rotating target. A sophisticated microcalorimetric technique was developed for on-line measurements of total nuclear heating in a mixed neutron plus photon field. Measurements with probes of graphite, titanium, copper, zirconium, niobium, molybdenum, tin, tungsten, and lead are presented. These measurements have been analyzed using the three-dimensional Monte Carlo code MCNP and various heating number/kerma factor libraries. The ra-
tio of calculated to experimental (C/E) heating rates shows a large deviation from 1 for all the materials except tungsten. For example, C/E's for graphite range from 1.14 ($\sigma = 10\%$) to 1.36 (10%) for various kerma factor libraries. Uncertainty estimates on total nuclear heating using a sensitivity approach are presented. Interestingly, C/E data for all libraries and materials can be consolidated to obtain a probability density distribution of C/E's that very much resembles a Gaussian distribution centered at 1.04. The concept of "quality factor" is defined and elaborated so as to take cognizance of observed uncertainties on prediction of nuclear heating for all the nine materials.

I. INTRODUCTION

Reliable prediction of nuclear heating in D-T neutron driven fusion reactors has long been recognized as a critical design issue. The methodologies to compute kerma factors from evaluated nuclear data files have been elaborated, and kerma factor libraries have been made available from time to time.[1-9] However, until very recently, practically no data were available on experimentally measured nuclear heat deposition rates, in a D-T neutron field, to test the kerma factor libraries. To fill this need, an effort to measure total nuclear heating using microcalorimetric technique in a simulated D-T fusion neutron environment was launched in

1988 under the U.S. DOE/JAERI collaborative program. It was continued in the following years and was culminated in 1993. Although calorimeters have been used in the past to measure total nuclear heating,[10-18] it was required to develop a sophisticated technique to measure very low temperature changes produced in a mixed neutron and photons field produced by a limited number of D-T neutrons. The source neutron intensity ranged from 1.5×10^{12} to 3×10^{12} n/s, and a typical calorimetric probe was kept at a distance of ~4 cm to enhance the signal for measurement purposes.[19-23]

A number of materials, in contention as leading candidates for various applications, i.e., molybdenum, tungsten, titanium, graphite (plasma-facing components), copper (magnet coils), iron, stainless steel, nickel (structural material components), aluminum, etc., were chosen for experiments. Bead thermistors and platinum resistance temperature detectors were employed as thermal sensors within calorimeters made of single materials (or probes). The first experiments were conducted during June 1989, and the tested materials included: Fe, Al, C, Cu. Each of these calorimeters was placed inside a vacuum chamber, and the mean distance from the target was ~8 cm. Experiments were also conducted on iron probe without vacuum chamber. The calorimeters were subjected to spaced neutron pulses of 3 to 10 min duration. The measured heat deposition rates ranged from 7 to 30 μW/g for a normalized source strength of 10^{12} n/s, with iron and graphite providing the lowest and the highest rates, respectively. The single-probe experiments were carried out again in December 1989. This allowed us to verify the reproducibility. This time, the average target-probe distance was shortened to ~5 cm, which led to 2 to 3 times higher rates. Tungsten was also included. More recently, during November 1990 and October-November 1991, experimental measurements were conducted on small single probes of graphite, titanium, stainless steel 304, nickel, zinc, zirconium, niobium, molybdenum, tin, tungsten, lead, and lithium carbonate. The typical distance from target to probe was brought down further to ~3.7 cm.

We will be confining ourselves to measurements made on plasma-facing materials. These materials include graphite, titanium, copper, zirconium, niobium, molybdenum, tin, tungsten, and lead. Remaining materials will be covered in a companion paper. First of all, features of the experimental technique will be presented, followed by measured data for a number of probe materials. Later, results of analysis using neutron and photon energy spectra obtained from neutral particle transport code MCNP (Ref. 24), and various kerma factor libraries, are presented and discussed for all nine materials. For almost every material, ratio of calculation (C) to experimental measurement (E) shows a large spread as one compares various kerma factor libraries. We also provide uncertainty estimates on total nuclear heating using a sensitivity approach. Interestingly, C/E data for all libraries and materials can be

consolidated to obtain a probability density distribution of C/E's that very much resembles a Gaussian distribution centered at 1.04. Also, we define and elaborate on the concept of "quality factor" for total nuclear heating. This factor helps in qualitatively understanding the status of uncertainty involved in predicting total nuclear heating in different materials using currently available kerma factor libraries.

II. CALORIMETRIC EXPERIMENTS

The microcalorimetric technique has earlier been applied for neutron/gamma dosimetry[10-14] and nuclear heat deposition rate measurements in fission reactors.[15-17] However, the application of this technique to measure nuclear heat deposition rate with currently available D-T neutron sources, maximum source strength being ~10^{12} n/s, requires careful experimentation owing to significant noise from the ambient temperature fluctuations.[19-23]

Important experimental considerations include: (a) simple and flexible design of calorimeter, (b) sensitive, fast, automated, and reliable instrumentation, (c) sensor characterization, (d) calorimeter calibration, (e) neutron source pulsing and monitoring, (f) measurement, (g) data processing-determination of heating rate and associated error.

II.A. Probe Design

A good probe design leads to good calorimetric measurements.[10,13] In this context, it is critical to understand heat transport pathways involving the probe vis-a-vis its surroundings. It helps very much if the following desirable considerations can be met: (a) thermal diffusion time across the probe should be as small as possible, (b) heat losses to the surroundings should be minimized, and (c) temperature change rate due to external heating source should be significantly larger than that due to ambience. The surroundings include also wires connecting a heated sensor to a measuring instrument. For our experiments, we took long, thin, insulated copper wires. A quick comparison of heat loss terms through various pathways showed that the heat loss through the connecting wires was negligible compared to the radiative heat loss from heated sensor. As a result, the former pathway is not elaborated in the considerations to follow.

Materialwise temperature change rates resulting from application of pulsed heating to the probe were simulated for a number of probe materials. A simplified sketch of a single-probe calorimeter is shown in Fig. 1. Figure 2 explains the basic operational principle of an ideal calorimeter operated in pulsed mode such that the probe is thermally decoupled from its surroundings. The temperature of the probe will stay constant in the absence of a neutron source, a heating source. When a constant neutron heating of the probe
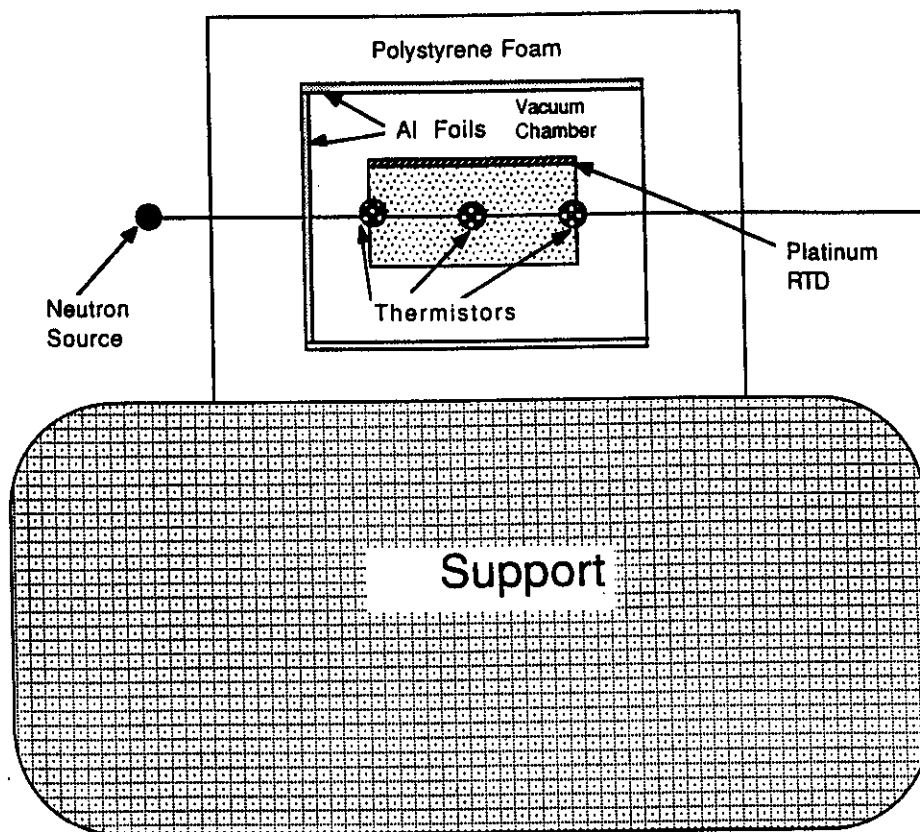
Fig. 1. Simplified picture of a single-probe calorimeter.

starts, the temperature of the probe rises linearly. In other words, if one looks at time derivative of the probe temperature, it will show a sudden and constant jump, from a baseline value of zero, each time the neutron
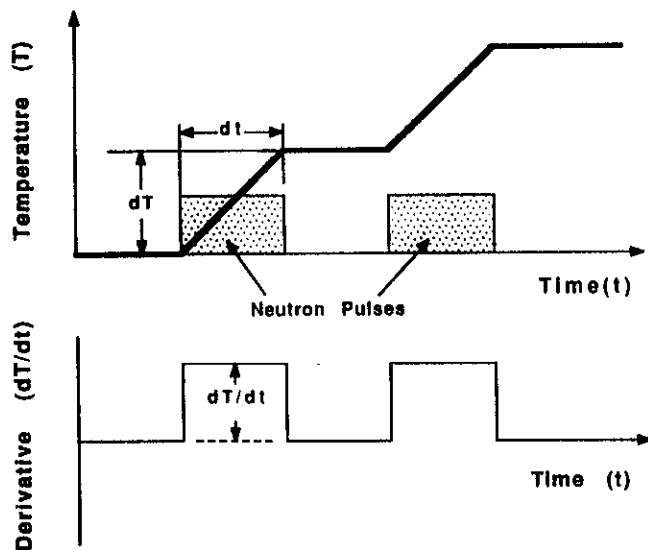

Fig. 2. Basic operational principle of the calorimetric method in pulsed mode.

source pulse is on. This derivative is directly proportional to the heating rate produced by the neutron source. However, even for a simplified calorimeter design shown in Fig. 1, the time derivative of the probe temperature is not expected to be a constant both during the pulse and its absence. A thermal analysis of the calorimeter design proves handy in understanding the variation of this derivative and its relationship to the external heating rate. One-dimensional thermal conduction analysis was carried out, for the arrangement shown in Fig. 1, in the probe medium along the system axis. The probe dimensions measured either 20 mm diameter by 20 mm length, or 50 mm diameter by 50 mm length. The neutron source was simulated by a pulsed heating source that followed $1/d^2$ dependence, where d is axial distance from the simulated point neutron source. The distance between simulated point neutron source and the front surface of the probe medium was taken as 3.8 cm. The simulated, pulsed heating rate averaged over the probe-mass was expressed in units of W/g, and was usually set at 100μW/g. A constant resistive heating source power, usually 100μW, was dissipated uniformly throughout the probe medium. This corresponds to a 100Ω RTD sensor drawing 1 mA current all the time. The probe was thermally coupled to its surroundings through simplified modeling of conductive and radiative processes. Time constants for thermal responses of

the sensors were assumed to be one second each. Johnson's noise was accounted while calculating time derivative of electrical resistance of a sensor as a function of time. A customized code TEMP was written up to calculate the temperature and resistance profiles of the sensors by incorporating all the considerations mentioned above.

Figure 3 shows temporal derivative of sensor temperature as a function of time for a 50 mm diameter by 50 mm long iron probe, subjected to three heat pulses of 300 s each, and spaced by 300 s. Also shown in the same figure is the temporal derivative of (volume-averaged) instantaneous probe temperature. Three sensors were considered to be located at the front, middle, and rear surfaces of the probe. A spike is seen for the front sensor as soon as a heat pulse sets in or goes off. The relative thermal responses of the three sensors are better seen in Figs. 4 and 5, which respectively show leading and trailing edges of the second D-T pulse (heat pulse). The middle sensor follows the heat pulse shape most faithfully. The front sensor overshoots the middle sensor during the leading edge phase and undershoots it following the trailing edge. The rear sensor is the slowest each time. Also, the times taken by the front and rear sensors to equilibrate to the middle sensor temperature derivative are quite comparable. The impact of probe size on relative thermal responses of the three sensors is brought out in Figs. 6 and 7 for an iron probe measuring 20 mm diameter by 20 mm length. It is to be emphasized here that all the three sensors predict

much closer responses for this smaller probe medium. After ~10 s of onset of the leading edge, the responses of the three sensors are hardly distinguishable; the same observation applies to the trailing edge.

Figures 8 and 9 show temperature derivatives for graphite (low atomic number) and tungsten (high atomic number) probes, respectively. Each probe measures 20 mm diameter × 20 mm length. It is to be noted that there is hardly any difference among the three sensors. This may be attributed to high diffusion lengths in the two media that, in turn, lead to low thermal diffusion times across the probes and, hence, fast thermal equilibration. An additional point that needs to be answered by these simulation studies is: how are pulse-wise temperature change rates related to external heating power? In this regard, it is to be stressed that instantaneous temperature change rate is directly proportional to external heating power, and, hence, it is adequate to compare the net temperature change rate during a pulse to the instantaneous temperature change rate. The net temperature change rate, say $\langle dT/dt \rangle_H^{net}$, during a pulse is derived using the following relation:

$$\left\langle \frac{dT}{dt} \right\rangle_H^{net} = \left\langle \frac{dT}{dt} \right\rangle_H - 0.5 \left[\left\langle \frac{dT}{dt} \right\rangle_{<H}^{D} + \left\langle \frac{dT}{dt} \right\rangle_{>H}^{D} \right] ,$$

(1)

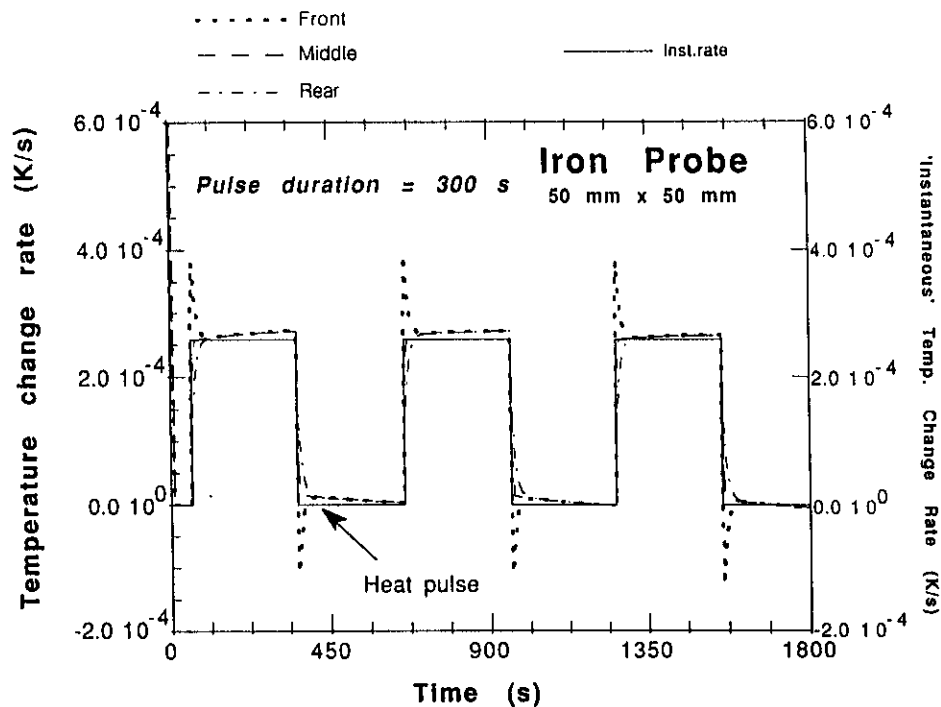and net external heating power dissipated in the probe medium, H^{net}, is given as

Fig. 3. Simulated temperature change rate versus time for a 50 mm long × 50 mm diameter iron probe (pulse duration = 300 s).
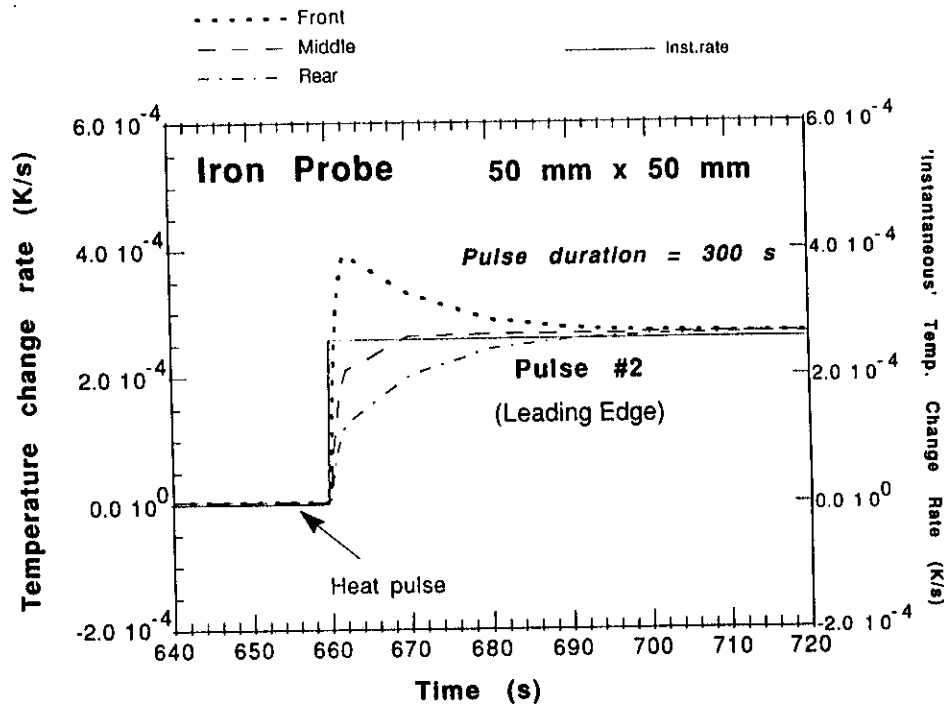
Fig. 4. Simulated temperature change rate versus time for a 50 mm long × 50 mm diameter iron probe near the leading edge (pulse duration = 300 s).

$$H^{net} = \left\langle \frac{dT}{dt} \right\rangle_H^{net} mC_p \ , \qquad (2)$$

where

$\langle dT/dt \rangle_H$ = time-averaged probe temperature derivative during the heat pulse

$\langle dT/dt \rangle_{<H}^D , \langle dT/dt \rangle_{>H}^D$

= time-averaged probe temperature derivatives in the drift periods immediately preceding and succeeding the heat pulse in question

m = mass of probe

C_p = specific heat of probe.

Figure 10 shows the normalized net temperature change rates as a function of pulse-sequence number for graphite, titanium, iron, molybdenum, and tungsten. Each probe measures 20 mm in diameter by 20 mm in length, except for graphite, which has an additional size measuring 50 mm in diameter by 50 mm in length. While the pulsed heating power is 100 μW/g, the constant resistive power is 100 μW. It is to be remarked here that graphite shows the largest deviation from unity. Also, the deviation is smaller for smaller graphite probe, and it declines fast as the pulse-sequence number rises. For all other probe media, the deviation from unity is generally less than one per cent. The impact of pulse heat-

ing power and resistive heating power was studied for titanium. The normalized net temperature change rate during a pulse depends more critically on pulse heating power. The results of the study are shown in Fig. 11. For example, for pulse heat power of 5 μW/g, the normalized temperature change rate is as low as ~0.93 for the first pulse even though it rises to 1.01 for the second pulse.

Before we move on, it is important to mention here that an alternative way to get net temperature change rate due to nuclear heating could consist of carrying out the following procedure, called the "integral method": First, fit a straight line through a set of time-dependent thermistor/RTD temperature changes for each beam-off (source neutrons are off) and beam-on (source neutrons are on) period; and second, take the difference of the slopes in contiguous beam-on and beam-off periods to get the net temperature change rate due to nuclear heating alone. But there are problems with this method. First of all, it is not correct to assume that a straight line fit is a good fit of the measured temperature changes. Secondly, it is very well possible that this integral method might even miss a nuclear heating pulse altogether if either (a) the drift rate were high or (b) the nuclear heating rate were low. In either event, one would be dealing with two slopes that would be dangerously close. This would lead to large errors. In our assessment, it is highly desirable to avoid using this integral method altogether, and, instead, follow our differential method as explained earlier in this work.
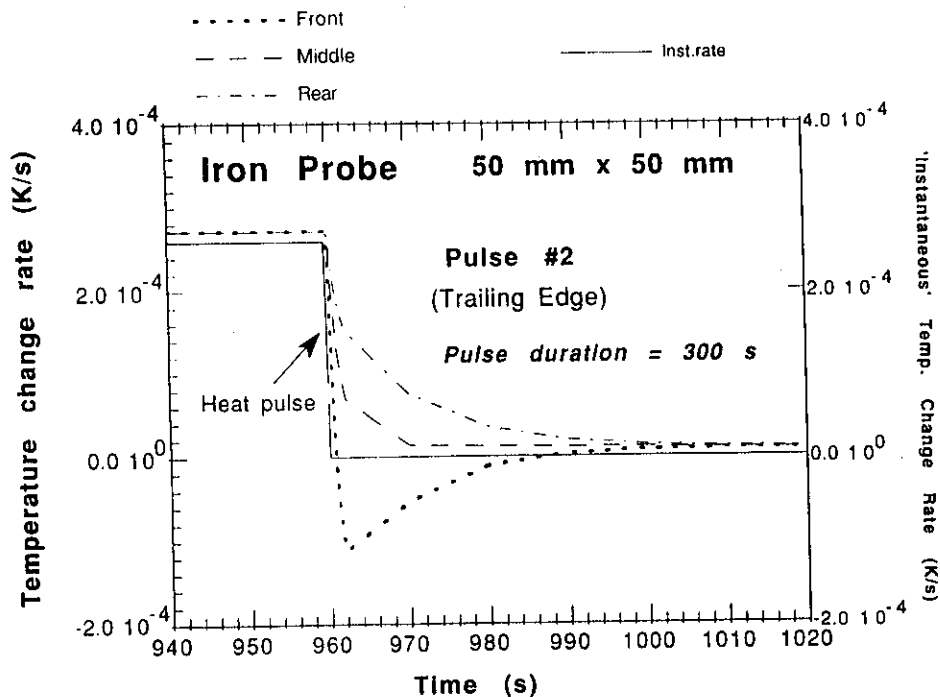
Fig. 5. Simulated temperature change rate versus time for a 50 mm long × 50 mm diameter iron probe near the trailing edge (pulse duration = 300 s).

II.B. Sensor Selection

Bead (point-size) thermistors (TM) and platinum resistance temperature detectors (RTD) were employed as thermal sensors. Four types of thermistors were employed, having 25°C resistances of 2.252 KΩ, 10 KΩ, 22 KΩ, and 30 KΩ. Thermistors with resistances of 2.252 KΩ and 30 KΩ were obtained from Omega
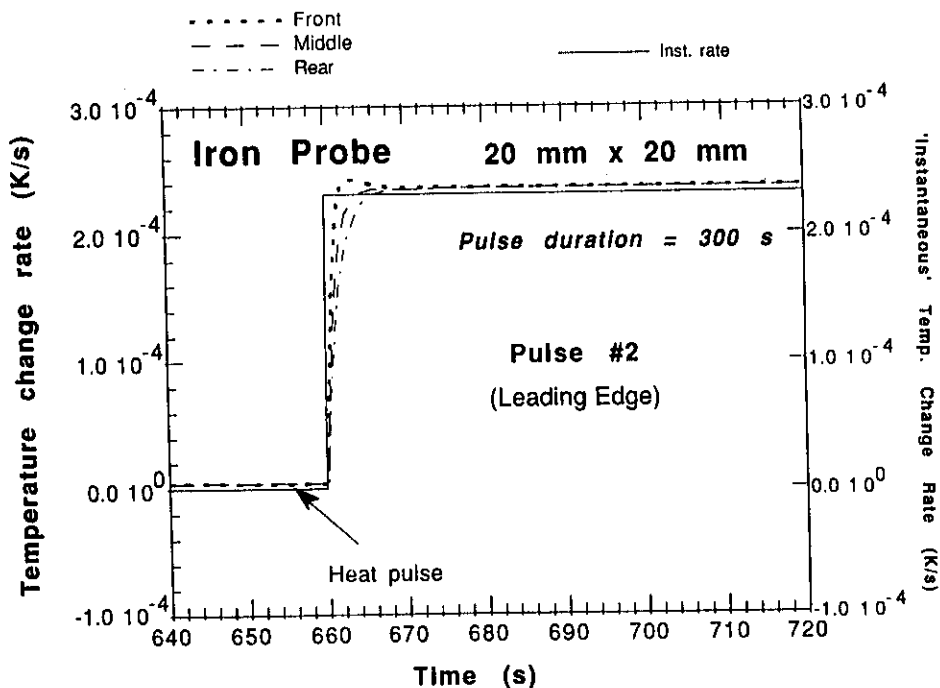

Fig. 6. Simulated temperature change rate versus time for a 20 mm long × 20 mm diameter iron probe near the leading edge (pulse duration = 300 s).
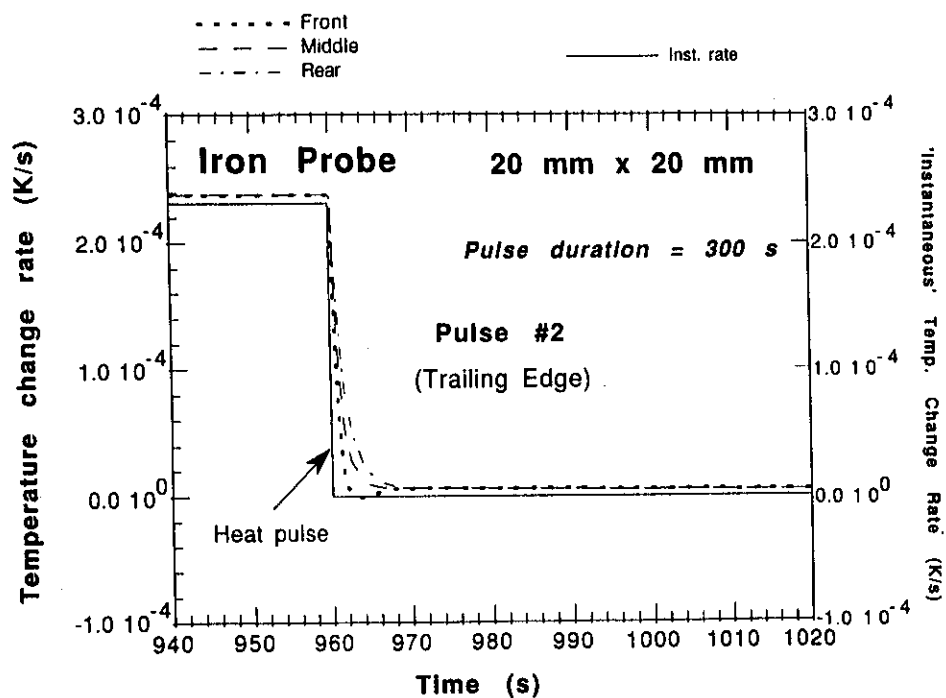
Front
Middle
Rear

Inst. rate

Fig. 7. Simulated temperature change rate versus time for a 20 mm long × 20 mm diameter iron probe near the trailing edge (pulse duration = 300 s).

Engineering Corporation and 10 KΩ and 22 KΩ thermistors came from Alpha Thermistor Company. A platinum RTD had resistance of 100 Ω at 0°C. The temperature coefficient of resistance for a thermistor and a platinum RTD were -4.4×10^{-2} per °C (at 25°C) and $+4.0 \times 10^{-3}$ per °C (at 0°C), respectively.

There have been concerns regarding fast neutron induced damage adversely affecting the performance of
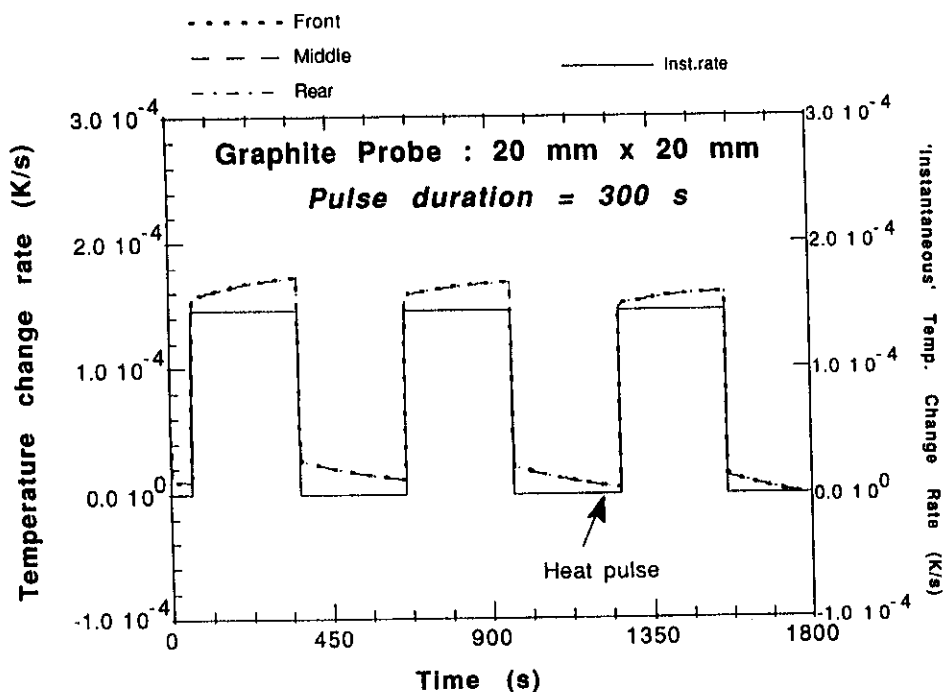
Front
Middle
Rear

Inst.rate

Fig. 8. Simulated temperature change rate versus time for a 20 mm long × 20 mm diameter graphite probe (pulse duration = 300 s).
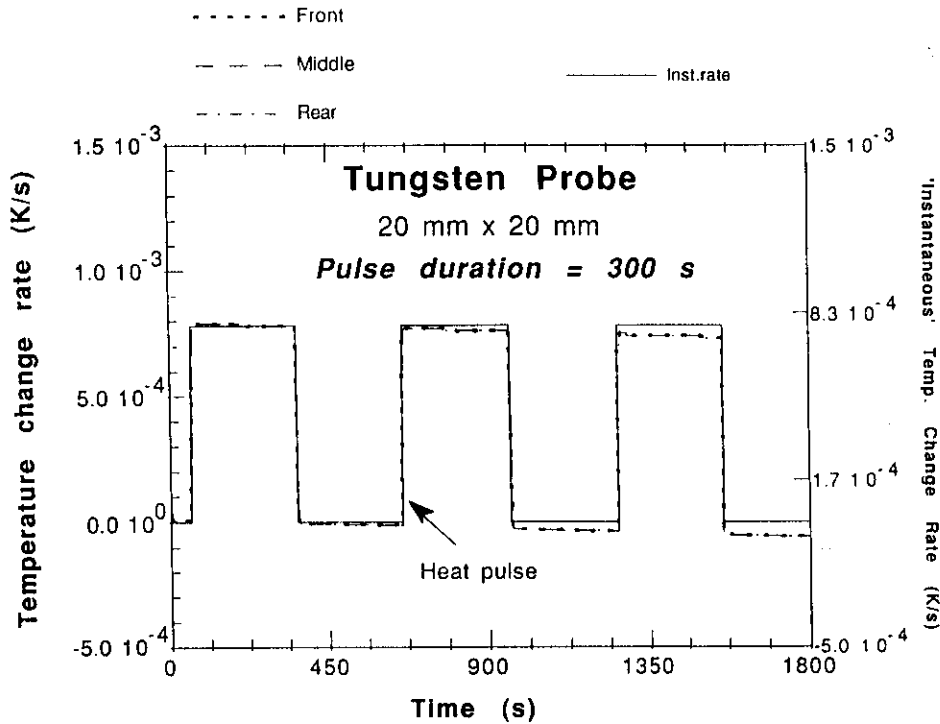
Fig. 9. Simulated temperature change rate versus time for a 20 mm long × 20 mm diameter tungsten probe (pulse duration = 300 s).

a thermistor. This was addressed before proceeding with thermistor use in first experiments done during June 1989.[20,21] It was experimentally demonstrated that there was a negligible likelihood of a thermistor
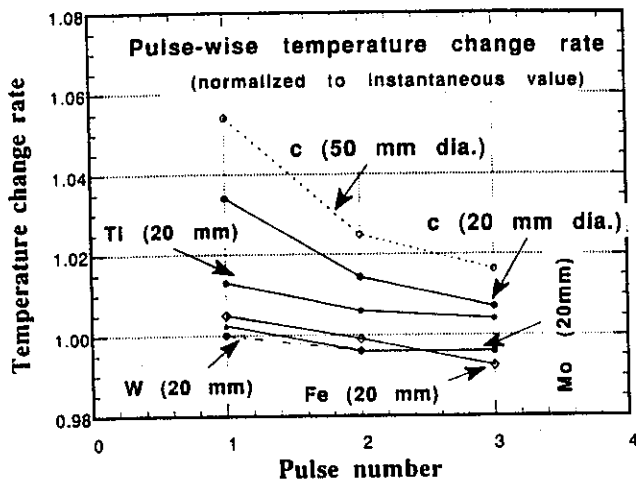

Fig. 10. Pulsewise temperature change rate, normalized to instantaneous value, versus pulse sequence number for probes of graphite (50 mm diameter × 50 mm long and 20 mm diameter × 20 mm long), titanium, iron, molybdenum, and tungsten. Pulsed heating power = 100 μW/g, and constant resistive power = 100 μW.

suffering any degradation as long as neutron fluence was below 3×10^{14} n/cm^2 — a safe limit for measurements to follow.[20,21]

II.C. Irradiation Geometry

Single-probe experiments were conducted during June 1989, December 1989, November 1990, and October-November 1991. Figure 12 shows a schematic of single-probe experiments conducted in June and December 1989. In these experiments, a typical probe consisted of a core, measuring 20 mm diameter by 20 mm length, that sat symmetrically inside a 1-mm-thick jacket, with external diameter and height of 32 mm each. During December 1989, a single tungsten probe, measuring 1 in. across with a vertical cross section of 2 × 2 in., was also included. The experiments done in November 1990 and October-November 1991 all had probes without a jacket. Typically, a probe measured 2 cm length × 2 cm diameter. Each probe was placed inside an evacuated vacuum chamber that measured 15 cm length × 10 cm diameter. The vacuum chamber had only 1 mm thick front wall.

During the June and December 1989 experimental periods, thermal sensors were placed as follows: thermistors on the front and back flat surfaces of the core plus close to its center: two RTD's, such that one was located — vertically to the axis of symmetry of the core — in the middle of the first half and the other one was placed in the middle of the latter half of the core.
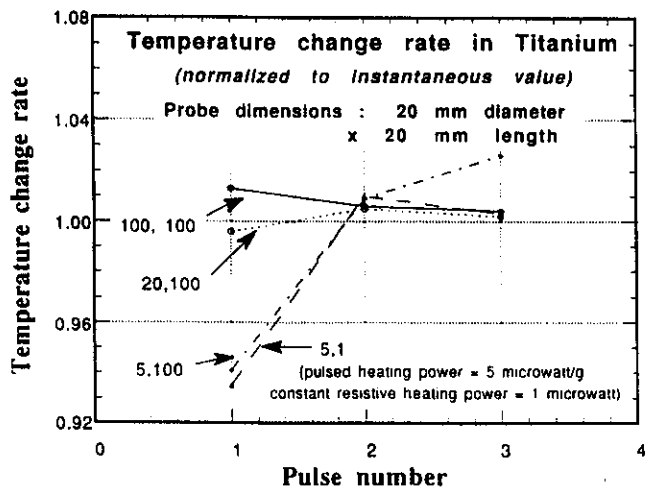
Fig. 11. Pulsewise temperature change rate, normalized to instantaneous value, versus pulse sequence number for a probe of titanium (20 mm diameter × 20 mm long). Variables include pulsed heating power, 5 to 100 μW/g, and constant resistive power, 1 to 100 μW.

In the case of tungsten, a 10 KΩ thermistor was placed at the center of the front surface and another thermistor of the same type was placed at the center of its back surface. Three additional thermistors and two RTD's were used for measurements outside the probes: (a) a 2.252 KΩ thermistor and an RTD were located on the target surface close to the source neutron generation area to follow the source temperature variation during the course of each experiment; (b) a 2.252 KΩ thermistor and an RTD were more than a metre away from the target to observe ambient temperature fluctuations; (c) a 2.252 KΩ thermistor was located on the inside of the front wall of the vacuum chamber. Apart from these additional sensors, three Nb foils were used in each experiment to monitor the source neutron flux across the probe. A Nb foil was located at the center of the front surface of the probe; another Nb foil was attached to the back surface. A third Nb foil was attached to outer surface of the front wall of the vacuum chamber. During the November 1990 and October-November 1991 experimental periods, only two niobium foils were used per probe: one in front and the other behind a probe. Each probe was kept in a vacuum chamber measuring 15 cm length by 10 cm diameter.

II.D. Instrumentation

The temperature change rate of interest could be as low as 1 μK/s for heat deposition rates in the range of 1 μW/g against a large background drift.[20-23] Measurement of such small temperature changes demands high precision and sophisticated instrumentation, in addition to highly sensitive and stable thermal sensors, for reliability and reproducibility.[10,13]

During the 1989 and 1990 experiments, we used a system configuration for picking up low-level voltage changes, developing on a thermal sensor, as shown in Figure 13 (Refs. 20 and 21). The controller was PC based: HP3497A or Macintosh SE (supplemented by
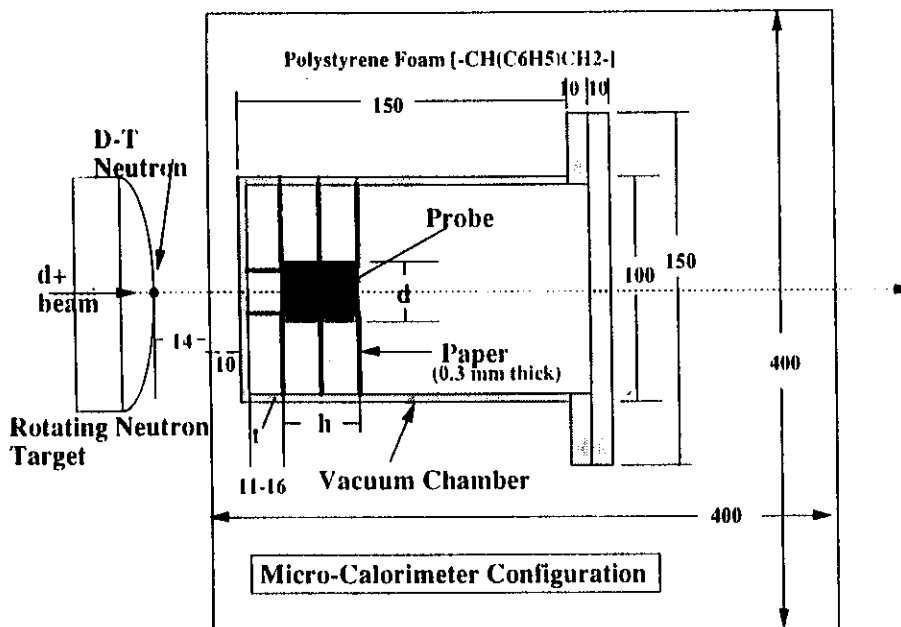

Fig. 12. Schematic arrangement for calorimetric nuclear heating measurements.
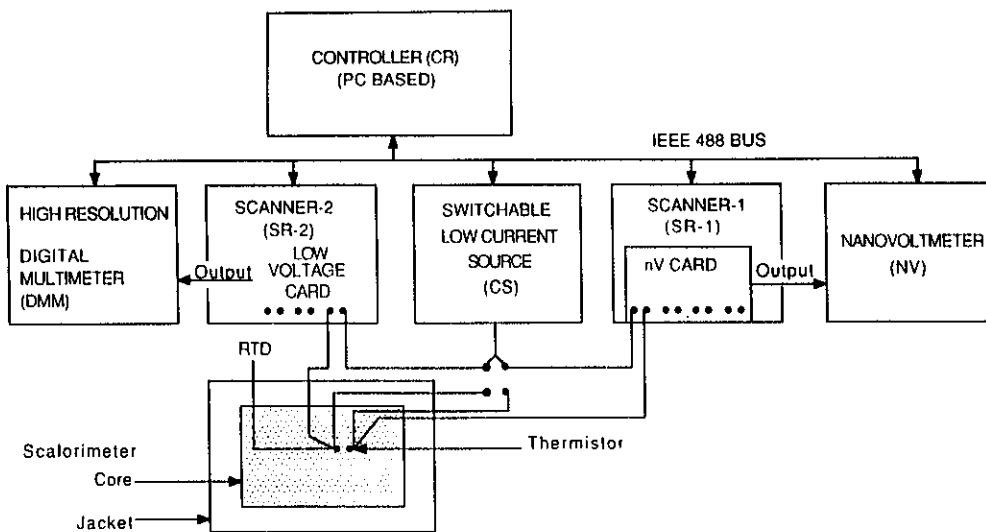
Fig. 13. A system configuration for low-voltage measurements.

a MacSCSI/IOtech interface and MacDriver488 driver software). While using the Macintosh SE, a programmable current source of HP3497A was used as such. Two scanners (model 705, Keithley) were used to separately switch TM's and RTD's. For TM switching, the model 7168 nV scanner card of Keithley was used. A single card could take up to 8 TM's. A current of 10 μA was passed through a TM to measure its voltage output by a nanovoltmeter with a resolution of 10 nV in 2mV range. A current of 1 mA was passed through an RTD to measure its output by Model 7081 precision voltmeter of Solatron. Also a rate meter was included to broadly monitor source neutron pulse history during an irradiation. The data acquisition process was driven by a BASIC program residing on the controller.

During the October-November 1991 experimental period, scanners were dropped[22] as shown in Fig. 14. This was done to have a better stability and a shorter
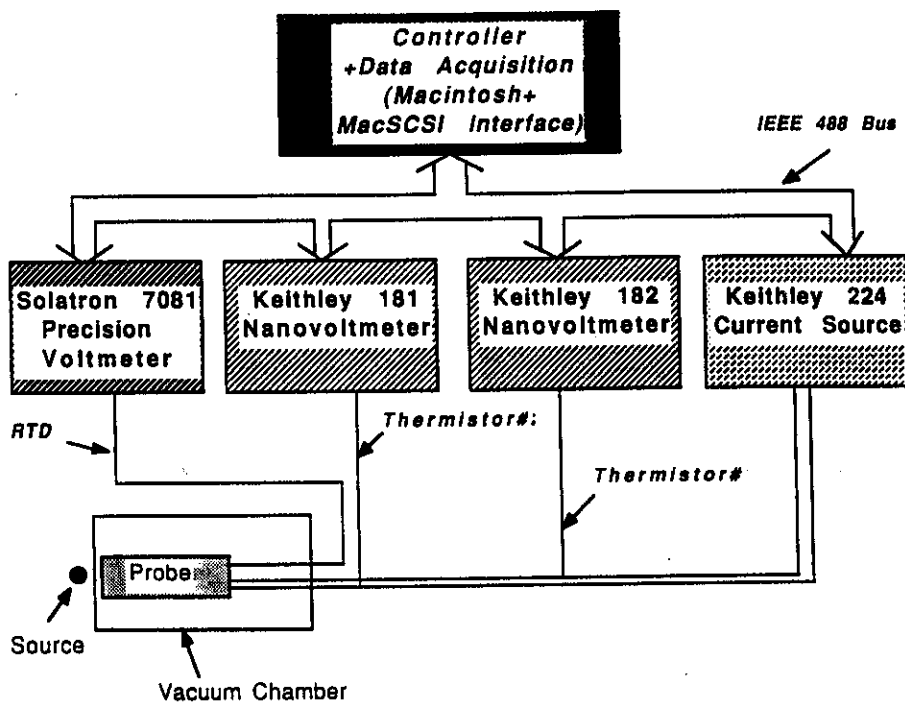

Fig. 14. A recent system configuration for nuclear heating measurements with microcalorimetric technique.

settling time for reading off voltage drop across the sensors due to constant current flow in all the sensors during an experiment. Loss of scanning was partially compensated by adding a Keithley 182 model of nanovoltmeter. It is a later but more sensitive version of the Keithley 181 model.[22]

II.E. Experimental Characteristics

Table I summarizes important characteristics of the single probe microcalorimetric measurements con-

ducted under the U.S. DOE/JAERI collaborative program. Probes with good thermal conductivity include graphite, titanium, aluminum, iron, nickel, stainless steel 304, copper, zinc, zirconium, niobium, molybdenum, tin, tungsten, and lead. A calorimetric probe of lithium carbonate was also used in October-November 1991. Five experimental periods have been identified as A, B, C, D, and E. They respectively identify June 1989, December 1989, November 1990, October-November 1991, and July 1992 periods. Graphite and

TABLE I

Characterization of Single Probe Nuclear Heating Experiments Done-to-Date

Probe Material	Experiment Identifier[a]	Probe Dimensions	Probe-Target Distance	On-Times of Pulse Sequence	Comments
Graphite	CA	2 cm ϕ × 2 cm l	7.3 cm	10 m	with jacket
	CB	2 cm ϕ × 2 cm l	4.2 cm	3 m/5 m/11 m	with jacket
	CC	2 cm ϕ × 2 cm l	3.8 cm	5 m	w/o jacket
	CD	2 cm ϕ × 2 cm l	3.9 cm	3 m	w/o jacket
	CD2[b]	2 cm ϕ × 2 cm l	4.4 cm	3 m	w/o jacket
Titanium	TIC	2 cm ϕ × 2 cm l	3.5 cm	5 m	w/o jacket
	TID	2 cm ϕ × 2 cm l	3.8 cm	3 m	w/o jacket
Aluminum	ALA	2 cm ϕ × 2 cm l	7.2 cm	3 m/5 m	with jacket
	ALB	2 cm ϕ × 2 cm l	4.6 cm	3 m/5 m	with jacket
Iron	FEA	2 cm ϕ × 2 cm l	7.7 cm	3 m/5 m/10 m/30 m	with jacket
	FEB	2 cm ϕ × 2 cm l	5.7 cm	3 m/5 m	with jacket
Nickel	NIC	2 cm ϕ × 2 cm l	3.6 cm	3 m/5 m	w/o jacket
	NID	2 cm ϕ × 2 cm l	4.0 cm	3 m/5 m	w/o jacket
SS304	SSC	2 cm ϕ × 2 cm l	3.5 cm	5 m	w/o jacket
	SSE[c]	cube of a side of 5.08 cm	3.6 to 25 cm	5 m	inside a SS304 assembly; w/o a vacuum chamber
Copper	CUA	2 cm ϕ × 2 cm l	7.8 cm	10 m	with jacket
	CUB	2 cm ϕ × 2 cm l	5.6 cm	3 m/5 m	with jacket
Zinc	ZND	2 cm ϕ × 2 cm l	3.8 cm	3 m	w/o jacket
Zirconium	ZRD	2 cm ϕ × 1.8 cm l	3.7 cm	3 m	w/o jacket
Niobium	NBD	2 cm ϕ × 2 cm l	3.8 cm	3 m	w/o jacket
Molybdenum	MOC	2 cm ϕ × 2 cm l	3.6 cm	5 m	w/o jacket
	MOD	2 cm ϕ × 2 cm l	4.0 cm	3 m	w/o jacket
Tin	SND	2 cm ϕ × 2 cm l	3.8 cm	3 m	w/o jacket
Tungsten	WB	2.5 cm l × 5 cm × 5 cm	4.2 cm	3 m/5 m	w/o jacket
	WC	2.1 cm ϕ × 2 cm l	3.6 cm	3 m	w/o jacket
	WD	2 cm ϕ × 2 cm l	3.7 cm	3 m	w/o jacket
	WD2[b]	2 cm ϕ × 2 cm l	4.4 cm	3 m	w/o jacket
Lead	PBD	2.1 cm ϕ × 2 cm l	3.7 cm	3 m	w/o jacket
Li_2CO_3	LCD	5 cm l × 5 cm × 5 cm	3.8 cm	10 m	w/o jacket

[a]A, B, C, D, E stand respectively for June '89, December '89, November '90, October-November '91, and July '92 experiments.

[b]With Li_2CO_3 enclosure around individual probes of graphite and tungsten.

[c]These measurements were done inside a SS304 assembly surrounded by Li_2CO_3. A thermistor each was attached to three insulated SS304 bricks stacked axially after one another. An RTD was attached to fourth SS304 brick.

tungsten probes were used for the largest number of experiments. During periods A and B, a 1 mm thick cylindrical jacket of the same material as the core was used for probes of graphite, aluminum, iron, and copper. During period D, a measurement each was made with graphite and tungsten calorimeters that were enclosed within a lithium carbonate shell assembly on all sides except the one facing the target. For a large majority of the measurements, the target to probe distance was ~4 cm. Usually, more than one run was made for each probe. In a single run, a probe was subjected to one to three D-T neutron pulses. The source neutron intensity ranged from 1.5×10^{12} to 3×10^{12} n/s. Usually, a pulse duration was either 3 m or 5 m, and two successive pulses were respectively separated by ~3 m to ~5 m. As mentioned earlier, most of the probes involved a simple cylindrical probe measuring 2 cm diameter by 2 cm length. However, during the periods A and B, a 1-mm-thick cylindrical jacket surrounded a probe. The outer dimensions of the jacket measured 32 mm diameter by 32 mm length.

III. FEATURES OF MEASURED AND PROCESSED DATA

III.A. Raw Resistance Change Data

Figures 15 through 21 show typical resistance change per cycle (length = 10 s) as a function of cycle no. for a TM (thermistor) or RTD attached to single probes of graphite, zirconium, niobium, molybdenum, tin, tungsten, and lead in experiments during October-November 1991. Figure 19 for a tin probe also shows relative 14-MeV neutron intensity as measured by rate meter. In Fig. 18 for a molybdenum probe, one can clearly observe differences in responses of the thermistors attached to front and rear surfaces of the probe.
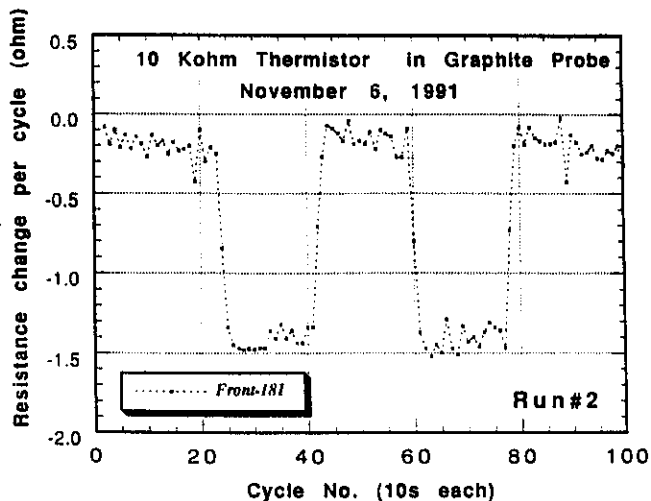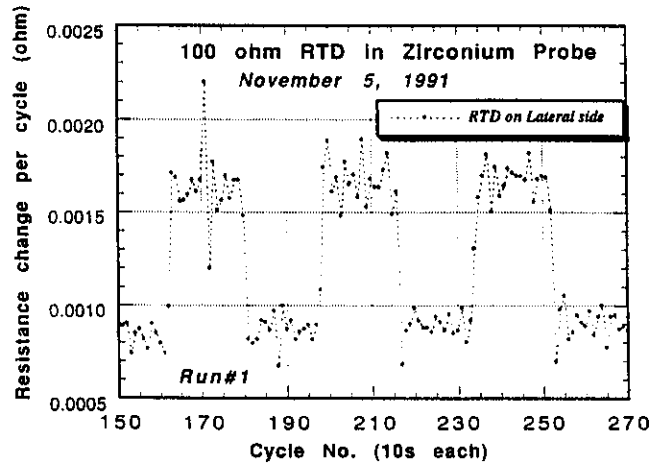

Fig. 16. Zirconium probe (November 91): Temporal profile of the temperature change rate observed via a 100 Ω RTD attached laterally.
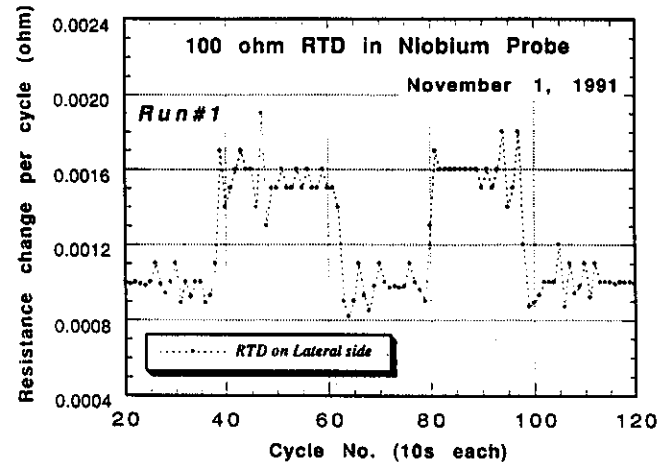

Fig. 17. Niobium probe (November 91): Temporal profile of the temperature change rate observed via a 100 Ω RTD attached laterally.

It is to be noted that the onset of the neutron source leads to an instantaneous drop in resistance of the front-TM that shows up as a dip in the drift curve. This is due to the larger instantaneous rise in temperature of the front end due to its shorter distance from the target. We call it overshooting of temperature, as depicted in the figure. It is to be noted that the temperature rises instantaneously everywhere inside the probe, but, due to rapidly decreasing D-T neutron flux as a function of distance from the target, the instantaneous rise in temperature at the rear end is significantly smaller than that at the front end. The overshooting of temperature is actually reflected as undershooting of resistance change in the figure. Then, the moment the neutron pulse is shut off, the front-TM senses it right away. This leads to an instantaneous drop in temperature increase. We

Fig. 15. Graphite probe (November 91): Temporal profile of the temperature change rate observed via a 10 KΩ thermistor kept in front.
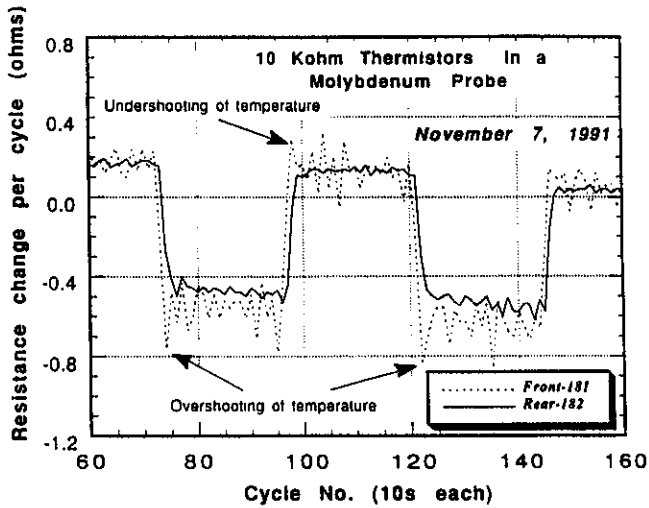
Fig. 18. Molybdenum probe (November 91): Temporal profile of the temperature change rate observed via a 10 KΩ thermistor each kept in front and rear.
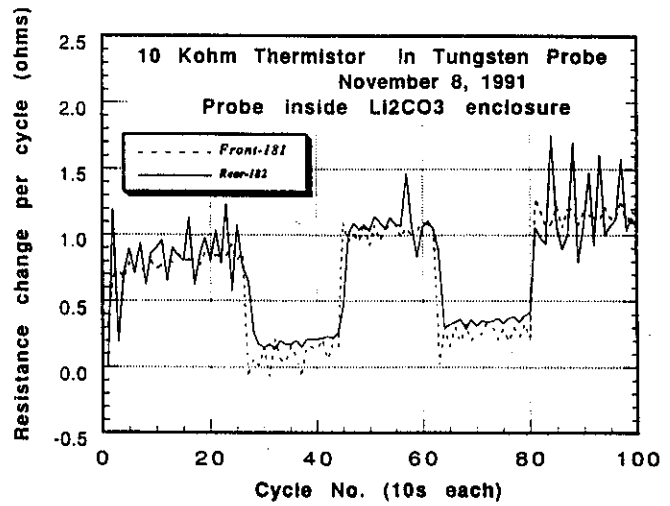

Fig. 20. Tungsten probe inside a Li_2CO_3 enclosure (November 91): Temporal profile of the temperature change rate observed via a 10 KΩ thermistor each kept in front and rear.
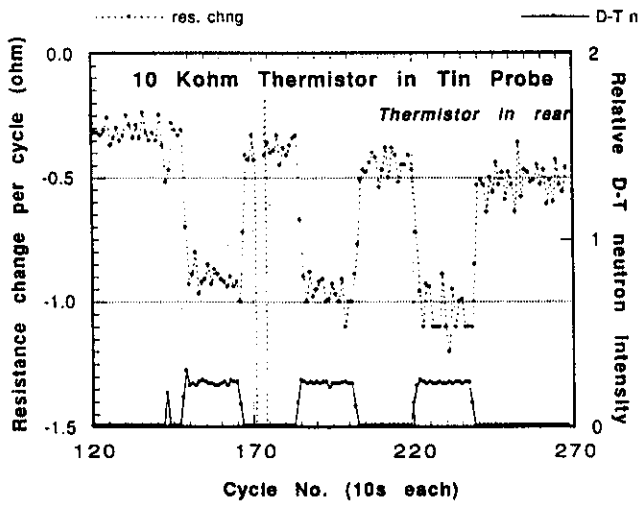

Fig. 19. Tin probe (October 91): Temporal profile of the temperature change rate observed via a 10 KΩ thermistor kept in rear.
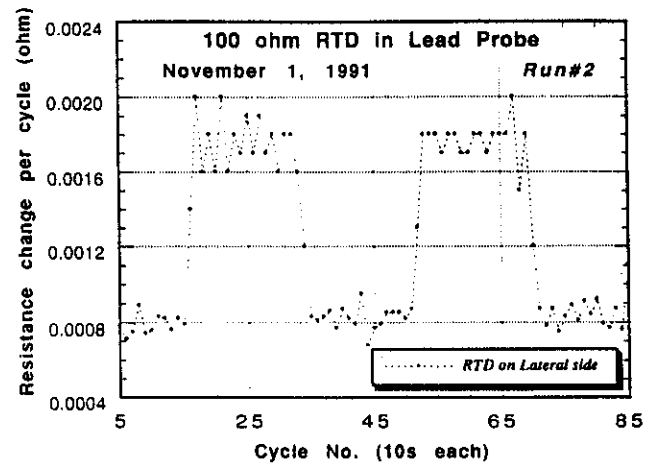

Fig. 21. Lead probe (November 91): Temporal profile of the temperature change rate observed via a 100 Ω RTD attached laterally.

call it undershooting of temperature, as shown on the figure. It translates into overshooting of resistance change in the figure. Abrupt and large changes seen in some curves are probably due to interference from stray electromagnetic signals.

III.B. Data Processing for Nuclear Heating Rate and Estimated Error

The raw resistance change data for a sensor is treated to obtain net resistance change rate, $\langle dR/dt \rangle_H^{net}$, as follows:

$$\left\langle \frac{dR}{dt} \right\rangle_H^{net} = \frac{1}{t_c} \left[\left\langle \frac{dR}{dc} \right\rangle_H - 0.5 \left\{ \left\langle \frac{dR}{dc} \right\rangle_{<H}^D + \left\langle \frac{dR}{dc} \right\rangle_{>H}^D \right\} \right],$$

(3)

where c represents a measuring cycle of length t_c; $\langle dR/dc \rangle_H$ is measuring cycle-averaged probe temperature derivative during the heat pulse; and $\langle dR/dc \rangle_{<H}^D$ and $\langle dR/dc \rangle_{>H}^D$ represent sensor resistance derivatives, averaged over measuring cycles, in the drift periods immediately preceding and succeeding a heat pulse of interest. The net temperature change rate during a heat

pulse is, then, obtained from the net resistance change rate as follows:

$$\left\langle \frac{dT}{dt} \right\rangle_H^{net} = \left\langle \frac{dR}{dt} \right\rangle_H^{net} \frac{C_{RT}}{(Y_n \times 10^{-12})} \ , \qquad (4)$$

where Y_n is the average source neutron intensity during the heat pulse and is expressed in units of 10^{12} to obtain a normalized net temperature change rate, and

$$C_{RT} = \frac{dT}{dR} \ .$$

For a 100 Ω RTD sensor used in the experiment, $C_{RT} = 2.53$ K/Ω. For a thermistor, however, C_{RT} is expressed as a function of temperature as follows:

$$C_{RT} = \frac{1}{\beta(T)R(T)} \ ,$$

where $\beta(T)$ is magnitude of the temperature coefficient of a thermistor at T. For a thermistor of 10 KΩ at 25°C,

$$\beta(T) \sim 0.044/°K \ ,$$

$$R(T) = 10^4 \Omega \ ,$$

and

$$C_{RT} \sim 2.27 \times 10^{-3} \ °K/\Omega \ .$$

Once $\langle dT/dt \rangle_H^{net}$ is known, the nuclear heating rate, H^{net}, can be obtained using Eq. (2). The two major likely sources of experimental error on the nuclear heating rate, H^{net}, are: (a) uncertainty on C_p and (b) experimental error on $\langle dT/dt \rangle_H^{net}$. The specific heat of the probe C_p has been known to vary for the same material from one piece of probe to another.[18] Also, the insertion of extraneous materials in a probe medium is likely to introduce additional uncertainty. We estimate this uncertainty to be usually less than 5%. However, for graphite, we found more than 25% difference between two sources of data.[22] The conventional way out of this source of uncertainty has been to experimentally determine the specific heat through an electric calibration process. However, we would like to add the following note of caution here. This process could hide systematic errors, on one hand, and might provide erroneous simulation of spatial distribution of nuclear heating, on the other. In the present work, we did not do electric calibration, and, instead, used the specific heat data available in literature. The estimated errors on various contributors to the experimental error are provided in Table II. The role of these contributions can be summarized as below:

1. Positioning of probe vis-a-vis neutron source: The probe of the calorimetric system was kept quite close to the target (3.5 to 4 cm). It was really difficult to know this distance very precisely. ^{93}Nb$(n,2n)^{92m}$Nb reaction rates of the niobium foils attached to front surface of each probe were utilized to derive the distance of the probe from the target. It is estimated[22] that

this procedure will contribute an error of 3 to 5% on $\langle dR/dt \rangle_H^{net}$.

2. Source neutron strength: The source neutron intensity is subject to change during the nuclear heating run due to tritium depletion in the target. It is estimated[22] that mean source strength will have ~2.5% uncertainty.

3. Error on $\langle dR/dt \rangle_H^{net}$ and $\langle dT/dt \rangle_H^{net}$: Change in the resistance of a sensor is derived from change in voltage drop across it as a function of time. The change in voltage drop across the sensor can arise due to (a) a change in the resistance of the sensor due to temperature change, and (b) numerous sources of noise that include source resistance noise (Johnson's noise), lack of close thermal contact between the sensor and the probe, degradation in the sensor quality, thermoelectric potentials at connections/junctions, varying magnetic fields in the vicinity, and radio frequency interference, among others. Care is taken to minimize the impact of these noise sources during the experiment. Flow of constant current in each sensor, use of Eq. (3), and long-enough nuclear heat source pulses help to further reduce the contributions of both low and high-frequency noise sources. Also, as mentioned earlier in Sec. II.A regarding $\langle dT/dt \rangle_H^{net}$ and instantaneous temperature change rate, there is an uncertainty involved in relating $\langle dR/dt \rangle_H^{net}$ to an ideal resistance change rate that is directly proportional to nuclear heating rate. A total uncertainty on $\langle dR/dt \rangle_H^{net}$ is expected to be in the range of 4 to 8% subject to getting a mean for this value over more than one nuclear heating pulse.

4. Total error on nuclear heating: As shown in Table II, one standard deviation of total uncertainty on nuclear heating is estimated to range from ~6 to ~12%. In principle, it is possible to further reduce uncertainties related to (a) positioning of the probe relative to the source, by better quality control of relative emplacement of the probe, the vacuum chamber, and

TABLE II

Estimated Uncertainty on Nuclear Heating Rate

Source of Uncertainty	Estimate of Uncertainty (%)
Positioning of probe relative to source	3 to 7
Source neutron intensity	2.5
Net temperature derivative, $\langle dT/dt \rangle_H^{net}$, determination from resistance drift curve	4 to 8
Specific heat, C_p, taken from published data[a]	1 to 5
Total uncertainty on nuclear heating	5.7 to 12.0

[a]In few cases, this uncertainty might significantly exceed 5%, though usually it is estimated to remain below this number.

outermost polystyrene foam box; (b) $\langle dT/dt \rangle_H^{net}$ determination, by developing and implementing a multi-layered probe such that it works in quasi-adiabatic mode[10] and better thermal contact of sensors to the probe medium; and (c) specific heat, by doing electrical heating calibration for each probe.

IV. ANALYTICAL PROCEDURE

Three-dimensional code MCNP (Ref. 24) was used for modeling the RNT geometry and the probe-vacuum chamber system. Whenever present, a cylindrical jacket surrounding the core of the probe was also modeled. The vacuum chamber was made of stainless steel 304. The background contribution was found negligible due to close proximity of the probe to the neutron source and hence it was subsequently ignored in all the computations. RMCCS library was used for neutron interactions and photon production in the whole system. This library has many cross sections based on ENDF/B-V. Particle transport computations were repeated with ENDL85 library, and differences were seen between neutron/photon energy spectra evaluated by the two libraries. Heating numbers from four libraries available[24] with MCNP, i.e., BMCCS, ENDL85, RMCCS, ENDF5T (or ENDF5U), were used for a comparison of nuclear heating rates. It is to be noted that ENDF5T/ENDF5U and RMCCS, to a large extent, originated from ENDF/B-V; ENDL85 was the latest library available from Lawrence Livermore National Laboratory; BMCCS contained older data, i.e., from ENDF/B-IV or ENDL73 files. RMCCS, ENDF5T/ENDF5U, and BMCCS (if from ENDF/B-IV) libraries contain heating numbers obtained by direct energy balance method. Some of these heating numbers have been known to be negative due to inconsistencies in evaluated nuclear data for a number of isotopes.[4,8,9,25,26] However, MCNP works with positive response functions only, and negative heating numbers, if originally present in a library, are equated to zero before being used for tallying.[25-27] ENDL85 has positive heating numbers that are used to adjust photon production cross sections and spectra for self-consistency.[4,7,27] MCPLIB was utilized for photon interactions and transport. The heat deposition rate drops very rapidly across the core due to its proximity to the source. However, as experimental conditions are designed to lead to quick thermal diffusion across core of an isolated probe, the heat deposition rate has to be averaged over the entire core to obtain the quantity that is to be compared to experimental measurements. The nuclear heat deposition rate, expressed in $\mu W/g$, is converted to temperature-change rate, expressed in $\mu K/s$, using specific heat data from Ref. 28.

The target and other important structural components attached to it were included in the modeling. The target structure does make a significant contribution to the γ-component of nuclear heating. Our calculations show that the fractional contribution of the target γ's to the γ-heating component in a probe is a very sensitive function of its atomic number (Z). This fraction rises as a function of Z, and is thus a lot more important for high Z probe than a low Z probe.[20] Previously, our calculations showed that for an iron calorimeter, used in the June 1989 experiment, the target structure accounted for as much as ~43% to γ-component of nuclear heating in the probe.[20]

Aside from the libraries available with MCNP, we have also used various other kerma factor libraries to obtain neutron and gamma-ray (or photon) heating rates, using RMCCS calculated neutron photon spectra for each experiment. ENDF/B-VI based MATXS library MATXS10, and ENDF/B-V based MATXS library MATXS5, are among those libraries.[5,29] Each library has 30 neutron groups and 12 photon groups.[29] In fact, there are two versions each for these two libraries, e.g., MATXS10-heat, MATXS10-kerma, MATXS5-heat, and MATXS5-kerma. The heat index stands for neutron kerma factors obtained through direct energy-balance method.[5,30] Basically, one subtracts the emitted neutron and photon energy from the available energy to get a neutron kerma factor in this method. The kerma index stands for "kinetic upper-estimate kerma."[5,30] The process used to generate this type of neutron kerma factor is similar to the one followed by MACK code[3] except that one assumes that the minimum kinematically possible amount of photons are produced. Thus, it is expected that heat kerma factor should generally be smaller than or equal to corresponding kerma value. However, we have observed that heat kerma factor is even larger than kerma value for some materials and neutron energies. In principle, it is expected that, for a large system, if one also uses each of these libraries for neutron and photon transport calculations, total heating rates for the two versions of a MATXS library would yield very close values due to overall conservation of energy.[5] In a small system, one could expect considerable differences between the heating rates using heat and kerma versions of a MATXS library as a good part of the energetic photons could escape from it.

Among other kerma factor libraries, KAOSLIB (Ref. 4), a new kerma factor library generated from ENDF/B-V library using KAOS-V code,[4] and a JENDL-3 based library were also used. In fact, we have used two variations of KAOSLIB library: (a) KAOSLIB-rec, recommended version, and (b) KAOSLIB-rec+cpd, recommended plus charged particle decay heat version. The latter variation includes decay heats from all radioactive charged particle products (or, in other words, recoiling products that are radioactive too) having half-lives up to 1 day. The JENDL-3 based library has 125 neutron groups, and it was obtained from basic JENDL-3 data files using NJOY processing code,[5,22,31,32] and the photon kerma factors came from DLC-99 (Ref. 33).

As shown in later sections, we have observed differences in photon heating rates, from various kerma

factor libraries, using same photon spectrum. To eliminate this source of discrepancy, we adopted the photon heating rates calculated with RMCCS library for all the libraries being compared.

V. ON CONTRIBUTORS TO DISCREPANCIES IN CALCULATED HEATING RATES AND UNCERTAINTY ESTIMATION

To understand the respective roles of various contributors to nuclear heating, let us look at the following relationship for total nuclear heating rate H:

$$\left|\frac{\Delta H}{H}\right|_{unc} = \sqrt{\sum_{i=1}^{ign} |P_n^i|^2 \left(\left|\frac{\Delta \phi_n^i}{\phi_n^i}\right|^2 + \left|\frac{\Delta k_n^i}{k_n^i}\right|^2\right) + \sum_{j=1}^{igp} |P_g^j|^2 \left(\left|\frac{\Delta \phi_g^j}{\phi_g^j}\right|^2 + \left|\frac{\Delta k_g^j}{k_g^j}\right|^2\right)} \qquad (8)$$

and

$$\left|\frac{\Delta H}{H}\right|_{max} = \sum_{i=1}^{ign} |P_n^i| \left(\left|\frac{\Delta \phi_n^i}{\phi_n^i}\right| + \left|\frac{\Delta k_n^i}{k_n^i}\right|\right) + \sum_{j=1}^{igp} |P_g^j| \left(\left|\frac{\Delta \phi_g^j}{\phi_g^j}\right| + \left|\frac{\Delta k_g^j}{k_g^j}\right|\right) . \qquad (9)$$

$$H = N\left(\sum_{i=1}^{ign} k_n^i \phi_n^i + \sum_{j=1}^{igp} k_g^j \phi_g^j\right) , \qquad (5)$$

where

N = nuclei density per unit mass or volume, depending on units chosen for H

ϕ_n^i, ϕ_g^j = neutron and gamma-ray (photon) flux in i and j energy groups, respectively

k_n^i = neutron kerma factor

k_g^j = photon kerma factor

ign = number of energy groups for neutrons

igp = number of energy groups for photons.

The relative prediction uncertainty in nuclear heating, $\Delta H/H$, is given by[34]

$$\frac{\Delta H}{H} = \sum_{i=1}^{ign} P_n^i \left(\frac{\Delta \phi_n^i}{\phi_n^i} + \frac{\Delta k_n^i}{k_n^i}\right) + \sum_{j=1}^{igp} P_g^j \left(\frac{\Delta \phi_g^j}{\phi_g^j} + \frac{\Delta k_g^j}{k_g^j}\right) , \qquad (6)$$

where

$$P_d^m = \frac{k_d^m \phi_d^m}{\sum_{i=1}^{ign} k_n^i \phi_n^i + \sum_{j=1}^{igp} k_g^j \phi_g^j} . \qquad (7)$$

In Eq. (7), $d = n$ or g, and m represents energy group. P_d^m is to be understood as (nuclear heating) integrated sensitivity for energy group (or bin) m for particle type d in keeping with widespread practice. It can be related

to sensitivity per unit lethargy (or differential sensitivity), say $P_d^m(u)$, through $P_d^m = P_d^m(u) \cdot \Delta u_d^m$. Here Δu_d^m represents lethargy-width of energy group (or bin) m for particle type d. Various considerations related to treatment, calculation, and discussion of sensitivity of a nuclear response in a fusion reactor have been presented in a number of publications and can be found in Refs. 34 through 42, among others. It is useful to have magnitudes of $|\Delta H/H|$ for (a) totally uncorrelated case, $|\Delta H/H|_{unc}$, and (b) fully correlated (or maximum) case, $|\Delta H/H|_{max}$. These are respectively given by:[34]

In the event of negative P_n^i or P_g^j, one can get less conservative estimates of $|\Delta H/H|_{unc}$ [Eq. (8)] and $|\Delta H/H|_{max}$ [Eq. (9)] by putting those negative numbers to zero. To get uncertainty estimates on total nuclear heating, Eqs. (8) and (9), it is required to know relative uncertainties on k_n^i, k_g^j, ϕ_n^i, and ϕ_g^j. In principle, one can utilize perturbation theory to obtain $|\Delta \phi_n^i/\phi_n^i|$ and $|\Delta \phi_g^j/\phi_g^j|$ provided one is able to have a good geometrical model of the entire experimental system and the uncertainties on the model, transport cross sections and energy, and angular distributions of secondary neutrons are rather small. The uncertainties on k_n^i and k_g^j could be estimated by nuclear data evaluators subject to availability of all required data files. Currently, the uncertainty files on kerma factors are unavailable. In what follows, an effort is being made to highlight the status of kerma factor data in different libraries, on one hand, and neutron and photon spectra calculations using different cross-section libraries, on the other. This comparative study will help in understanding and obtaining estimates of uncertainties on kerma factors and neutron and photon spectra. Then, all this information can be pieced together to get estimates of prediction uncertainty of nuclear heating for selected cases.

V.A. Kerma Factors

Kerma factors from BMCCS, ENDL-85, RMCCS, ENDF5, MATXS10 (heat and kerma), MATXS5 (heat and kerma), KAOSLIB(rec > recommended, rec+ cpd > recommended plus charged product decay heat), and JENDL-3 have been compared for graphite, titanium, copper, zirconium, niobium, molybdenum, tin, tungsten, and lead, among other materials. Generally, large differences have been found for neutron kerma factors as a function of energy. Even for photons, differences have been observed for kerma factors from

different libraries. As one eventually looks at heating rates, which involves an integration of product of kerma factor and flux over energy range, it is meaningful to see if kerma factors from different libraries all differ significantly in some kind of integral sense. In this respect, we propose to look at lethargy-wise integration of kerma factor as follows:

$$KI = \int_{E_{max}}^{E_{min}} k(E)\, du(E) , \qquad (10)$$

where KI is to be understood as kerma factor integral and $k(E)$ and $u(E)$ are kerma factor and lethargy at energy E. In multigroup formulation, one can express neutron and photon kerma factor integrals, say, KI_n and KI_g, as below:

$$KI_n = \sum_{i=1}^{ign} k_n^i \Delta u_n^i \qquad (11a)$$

and

$$KI_g = \sum_{j=1}^{igp} k_g^j \Delta u_g^j . \qquad (11b)$$

We express kerma factors and integrals in units of Joule barn (or simply J·b). Tables III and IV list KI_n's for respective energy ranges of 14.92 to 13.5 MeV (covering a good part of D-T neutron energy spread) and 14.92 to 0.1 MeV. Except for niobium, a dash indicates the absence of neutron kerma factors in that particular library. (This data was not at hand for niobium while writing this paper.) It is to be noted that for MATXS10 library, that is based on ENDF/B-VI, kerma integrals are smaller than heat integrals for zirconium and tungsten. It appears that this contradictory result could be ascribable to lack of overall energy balance when considering all reaction channels.[5,30] Also, integrals are negative for molybdenum in MATXS10 (heat) as well as MATXS5 (heat). Note that KAOSLIB and MATXS5 (kerma) integrals are usually close, but they differ very widely for titanium, even though the basic data base is ENDF/B-V for both. JENDL-3 and ENDL-85 integrals lie close enough except for molybdenum and zirconium. Whereas MATXS10 (kerma) and JENDL-3 integrals are close for graphite, copper, tungsten, and lead, they differ very widely for titanium, zirconium, niobium, and molybdenum. Due to non-availability of uncertainty files on neutron kerma factors, we have opted to use ENDF/B-VI based MATXS10 (heat) and ENDF/B-V based MATXS5 (heat) groupwise neutron kerma factors to estimate groupwise uncertainties on neutron kerma factors. Of course, others might follow a different approach. Figure 22 displays an estimate of fractional standard deviation on neutron kerma factors for graphite, titanium, and niobium, using heat kerma factors from MATXS10 and MATXS5. For the most part, the estimated standard deviation is below 10% for graphite and tungsten. However, for niobium, the estimated standard deviation is more than 50% in most
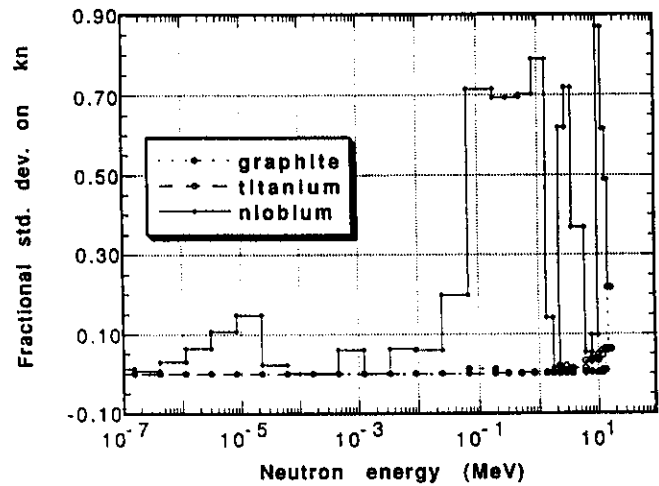

Fig. 22. Estimated uncertainty on neutron kerma factors from MATXS10 ('heat') for graphite, titanium, and niobium as a function of neutron energy.

of the neutron energy range above 0.1 MeV. Interestingly, for molybdenum, the kerma factors from the two libraries are identical for higher neutron energies. It implies that for molybdenum, relative deviation on kerma factors is zero! But, this is in direct contradiction with the fact that, for many energy groups, MATXS10 (heat) kerma factors continue to be negative—a sure sign of the inadequate state of the art. It is to be thus stressed that the estimated standard deviation values obtained using MATXS10 and MATXS5 possibly provide only a rather low estimate of the actual numbers, as will become quite clear in Sec. VI of this paper, from quite large differences observed in energywise neutron kerma factors from different libraries.

Kerma factor integrals for photons are listed for MCPLIB and MATXS10 in Table V. The integrals are not listed for zirconium, niobium, and molybdenum for MCPLIB, even though they can be obtained. It is to be remarked that there appears to be a baseline trend that the difference between the integrals from the two libraries is going up as a function of atomic number of the material, and, systematically, MATXS10 KI_g's are larger. Probably, it is due to just one very coarse energy group below 0.5 MeV in MATXS10. It is a critical energy region due to the fact that kerma factor undergoes a large change in this energy range. Note that even as the two sets of integrals differ by just ~4% for graphite, the difference rises to ~38% for lead. The difference is too large, and the solution obviously lies in having finer energy groups below ~0.5 MeV for the MATXS library.

V.B. Flux

Calculated neutron and photon energy spectra carry uncertainty due to inexact geometric modeling, the

TABLE III

Intercomparison of Neutron Kerma Factor Integrals in Various Nuclear Data Libraries

(Energy range > 14.92 through 13.5 MeV)

	Neutron Kerma Factor Integrals (J·b) (Energy range > 14.92 through 13.5 MeV)										
Material	bmccs[a]	endl-85[a]	rmccs[a]	endf/b-v[a]	matxs10 'heat'	matxs10 'kerma'	matxs5 'heat'	matxs5 'kerma'	kaoslib 'rec'	kaoslib 'rec + cpd'	jendl-3
Graphite	5.202E−14[b]	4.557E−14	5.030E−14	5.030E−14	4.142E−14	4.142E−14	4.397E−14	4.397E−14	4.426E−14	4.426E−14	4.308E−14
Titanium	1.583E−14	2.208E−14	2.209E−14	2.209E−14	1.965E−14	3.525E−14	1.845E−14	3.404E−14	5.273E−15	5.485E−15	2.198E−14
Copper	2.819E−14	3.250E−14	3.847E−15	3.847E−15	3.195E−14	3.195E−14	3.673E−14	4.335E−14	4.384E−14	5.167E−14	3.063E−14
Zirconium	2.684E−15	8.807E−15	1.173E−13	1.173E−13	1.253E−13	1.544E−14	1.253E−13	1.544E−13	1.492E−14	1.507E−14	1.344E−14
Niobium	---	---	---	---	4.716E−15	2.045E−14	1.335E−14	1.889E−14	1.349E−14	1.349E−14	1.404E−14
Molybdenum	4.392E−17	7.021E−15	0.0	0.0	−3.337E−15	6.105E−15	−3.337E−15	6.105E−15	6.460E−15	6.997E−15	1.682E−14
Tin	1.216E−13	5.899E−15	---	---	---	---	---	---	---	---	---
Tungsten	---	5.043E−15	6.433E−15	---	6.400E−15	5.080E−15	6.402E−15	5.080E−15	5.252E−15	5.268E−15	4.634E−15
Lead	4.150E−14	4.656E−15	6.728E−14	6.728E−14	5.085E−15	5.085E−15	4.295E−14	4.397E−15	4.615E−15	4.620E−15	4.733E−15

[a]Continuous energy libraries used with MCNP.
[b]Read as 5.202×10^{-14}.

TABLE IV

Intercomparison of Neutron Kerma Factor Integrals in Various Nuclear Data Libraries

(Energy range > 14.92 through 0.1 MeV)

	Neutron Kerma Factor Integrals (J·b) (Energy range > 14.92 through 0.1 MeV)										
Material	bmccs[a]	endl-85[a]	rmccs[a]	endf/b-v[a]	matxs10 'heat'	matxs10 'kerma'	matxs5 'heat'	matxs5 'kerma'	kaoslib 'rec'	kaoslib 'rec + cpd'	jendl-3
Graphite	5.036E−13[b]	5.134E−13	4.961E−13	4.961E−13	4.754E−13	4.754E−13	4.805E−13	4.805E−13	4.809E−13	4.809E−13	4.701E−13
Titanium	2.108E−13	1.978E−13	1.864E−13	1.862E−13	1.921E−13	2.481E−13	1.864E−13	2.424E−13	1.496E−13	1.507E−13	1.642E−13
Copper	3.702E−13	2.359E−13	3.068E−13	3.068E−13	2.631E−13	2.631E−13	3.098E−13	2.975E−13	3.011E−13	3.194E−13	2.274E−13
Zirconium	1.607E−13	1.171E−13	2.018E−12	2.018E−12	1.995E−12	1.373E−13	1.997E−12	1.373E−13	1.380E−13	1.387E−13	1.183E−13
Niobium	---	---	---	---	7.747E−14	1.497E−13	−1.058E−13	1.585E−13	1.264E−13	1.264E−13	1.264E−13
Molybdenum	6.090E−14	1.068E−13	3.369E−14	3.369E−14	−4.393E−14	1.067E−13	−4.410E−14	1.067E−13	1.075E−13	1.094E−13	1.278E−13
Tin	2.566E−12	1.296E−11	---	---	---	---	---	---	---	---	---
Tungsten	---	5.775E−14	1.258E−13	---	1.245E−13	6.471E−14	1.245E−13	6.471E−14	6.494E−14	6.999E−14	5.035E−14
Lead	1.807E−13	6.105E−14	2.085E−13	2.085E−13	7.006E−14	7.006E−14	9.867E−14	6.959E−14	6.933E−14	6.947E−14	5.959E−14

[a]Continuous energy libraries used with MCNP.
[b]Read as 5.03×10^{-13}.

TABLE V

Gamma-Ray Kerma Factor Integrals

| Material	Gamma-Ray Kerma Factor Integrals (J·b) (Energy range > 10 MeV through 0.1 MeV)	
	mcplib	matxs10
Graphite	5.882E−13[a]	6.131E−13
Titanium	2.699E−12	2.851E−12
Copper	3.944E−12	4.216E−12
Zirconium	---	7.130E−12
Niobium	---	7.453E−12
Molybdenum	---	7.788E−12
Tin	9.759E−12	---
Tungsten	2.164E−11	2.745E−11
Lead	2.605E−11	3.594E−11

[a]Read as 5.882×10^{-13}.

Fig. 23. Comparison of neutron spectra per unit lethargy in a graphite probe (November 90 experiment) computed by RMCCS and ENDL-85 Transport Libraries used with MCNP.
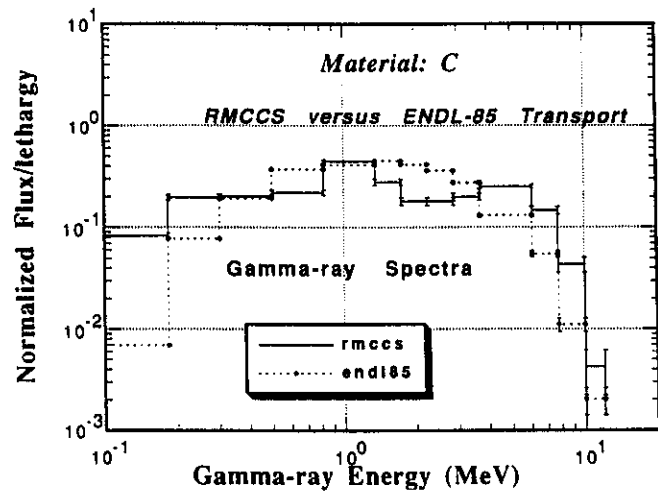

Fig. 24. Comparison of gamma-ray spectra per unit lethargy in a graphite probe (November 90 experiment) computed by RMCCS and ENDL-85 Transport Libraries used with MCNP.

uncertainties carried by transport cross sections and energy-angular distribution of secondary neutrons/ photons, and the additional calculational error associated with the transport code used. The additional calculational error due to MCNP, used in analog mode for our calculations, is statistical due to a limited number of particle histories followed and varies for each energy group.

For neutron transport calculations, various cross-section libraries were available with MCNP including RMCCS, ENDF5, and ENDL-85. RMCCS is largely adapted from ENDF/B-V (or ENDF5), even though it has evaluations by the T-2 group of LANL for a number of materials. ENDL-85 is an independent cross-section library from LLNL. We have done separate calculations with RMCCS and ENDL-85 for a number of experiments and compared the neutron and photon energy spectra obtained from the two libraries. This comparison can be utilized to obtain mean particle spectra and energy-wise relative deviation of RMCCS (or ENDL-85) spectrum from this mean. In particular, we want to discuss the two sets of energy spectra for four experiments done during the 1990 period, using individual probes of graphite, titanium, molybdenum, and tungsten, respectively. Figures 23, 24, and 25 for graphite, show typical neutron and gamma-ray spectra and relative standard deviations on these quantities for these probes. The normalized spectra plotted in these figures have been obtained from particle flux by dividing it by lethargy width for each energy-bin. Energy-bin boundaries correspond to 30 neutron energy groups of MATXS10 library. A few common observations regarding both RMCCS and ENDL-85 are in order: First, for neutron spectra, the spectrum in source neutron groups is as much as 2 orders larger compared to any other energy group for all the probes (see Fig. 23). This
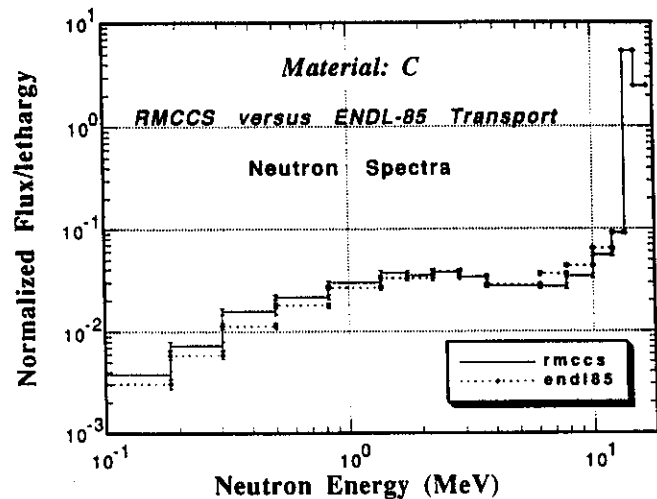
can be expected, as the probe thickness of 2 cm is not enough to slow down a significant number of source neutrons. In addition, the closeness of the probe to the target ensures that there is an imperceptible contribution from room-returning neutrons to lower neutron energy groups. Apart from source energy, there is a broad peak of inelastically scattered neutrons around 1 to 2 MeV. Second, gamma-ray energy spectra are relatively flat in the energy range extending from ~0.2 to ~6 MeV, and appear to have a bell shape with a broad peak around ~1 MeV (see Fig. 24). These photons
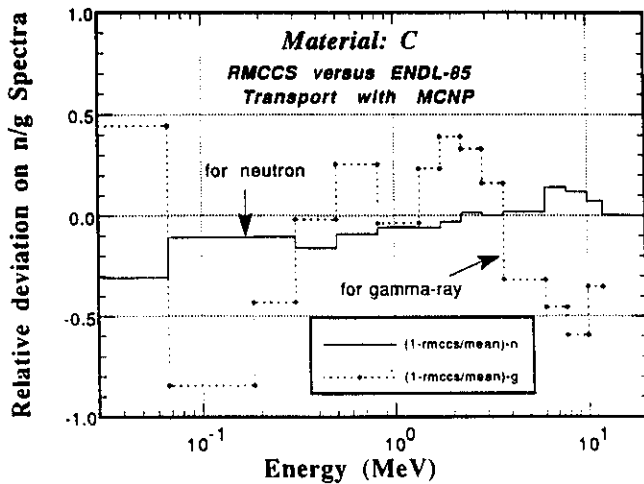
Fig. 25. Relative deviation of neutron and gamma-ray spectra with respect to their means for the graphite probe.

could result from inelastic and/or capture reactions of neutrons. As for differences in spectra from the two libraries (see Fig. 25), the following remarks apply: (a) a relatively large relative deviation is observed for both neutron and gamma-ray spectra for all the probes, 20 to 40% deviation looking quite common; (b) as for neutron spectra, 10 to 20% deviation is observed for the source energy groups; (c) as for photon spectra, the largest discrepancies are observed for graphite and tungsten media.

In view of large relative deviations obtained for the photon spectra, it is quite crucial to note that photon-producing neutron capture reactions assume quite an importance. These capture reactions are essentially dominated by the lower energy component of the neutron spectrum. Interestingly, the same component of the neutron spectrum makes an insignificant contribution to the neutron heating due to overwhelming dominance of the source neutron component. In spite of best modeling efforts, it is quite probable that neutron capture driven photon production might carry large uncertainty that would be difficult to estimate. In other words, the relative deviations on photon spectra presented above have to be understood as optimistic estimates only.

V.C. Prediction Uncertainty Estimation

Once estimated uncertainties on kerma factors and particle flux are available along with the sensitivity profiles, one can use Eqs. (6), (8), and (9) to obtain estimated prediction uncertainties on total nuclear heating rates. To understand and compare the individual prediction uncertainties from various kerma factor libraries, we have used two sets of transport cross-section libraries for four single-probe experiments done in

1990 — the experiments related to graphite, titanium, molybdenum, and tungsten (as already referred to in Sec. V.B). Two independent approaches have been followed to get prediction uncertainty on nuclear heating rate. In the first approach, individual prediction uncertainty for each of the four MCNP libraries, i.e., BMCCS, ENDL-85, RMCCS, and ENDF5, was obtained with two sets of neutron/photon flux: (a) with RMCCS transport calculation, and (b) with ENDL-85 transport calculation. For each set of neutron/photon flux, mean C, say $\langle C \rangle$, was first obtained by taking an arithmetic average of individual heating rates through each of the four kerma factor libraries. Then $C/\langle C \rangle - 1$ was obtained for both RMCCS and ENDL-85 flux based heating rates for all the four libraries.

The second approach was based on using RMCCS based flux with neutron and photon kerma factors of MATXS10 (heat). First of all, neutron and photon heating sensitivity profiles were obtained for each probe medium. Thereafter, Eqs. (8) and (9) were used to get fully correlated (maximum or max) and totally uncorrelated (unc) uncertainties in nuclear heating rates (see the previous sections on obtaining uncertainties on kerma factors and neutron/photon flux). It is to be noted that we have assumed that there is no uncertainty on photon kerma factors from MATXS10. This omission will act to drive down the uncertainty estimates from the second approach. Table VI provides $C/\langle C \rangle - 1$ from the first approach for each of the four kerma factor libraries, as well as max and unc estimates of heating uncertainty from the second approach. Some of these numbers are plotted in Fig. 26. If BMCCS based
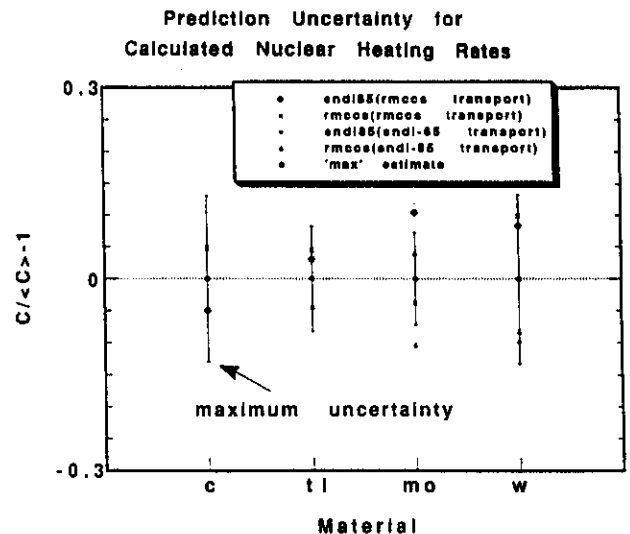

Fig. 26. Deviation from unity of ratio of computed to "mean computed" nuclear heating, $C/\langle C \rangle - 1$, in graphite, titanium, molybdenum, and tungsten probes, and fully correlated (maximum) sensitivity estimate.

TABLE VI

Deviation from Unity of Ratio of Computed to "Mean Computed" Nuclear Heating Rates

Material	$C/\langle C \rangle - 1$, Ratio of Computed to "Mean Computed" Heating Rate $- 1$								Sensitivity Estimate $\frac{\|\Delta H/H\|_{max}}{(\|\Delta H/H\|_{unc})}$
	rmccs Flux				endl-85 Flux				
	bmccs[a]	endl-85[a]	rmccs[a]	endf/b-v[a]	bmccs[a]	endl-85[a]	rmccs[a]	endf/b-v[a]	
Graphite	0.080	−0.05	0.048	0.047	0.082	−0.048	0.048	0.048	0.130 (0.079)
Titanium	−0.134	0.031	0.045	0.045	−0.208	−0.045	−0.045	−0.031	0.082 (0.028)
Molybdenum	−0.031	0.104	−0.038	−0.038	−0.096	0.038	−0.103	−0.103	0.072 (0.024)
Tungsten	---	0.083	0.099	---	---	−0.099	−0.083	---	0.132 (0.070)

[a]Continuous energy libraries used with MCNP.

numbers are excluded from consideration, the *max* estimate appears reasonable for all materials except molybdenum. Both RMCCS and ENDL-85 estimates from the first approach are significantly larger than the *max* estimate from the second approach for molybdenum! This apparent contradiction results directly from large differences in total heating rates calculated through RMCCS and ENDL-85 for this particular probe.

In the next section, both the approaches outlined above will be followed with an important difference: $\langle C \rangle$ will be replaced by E, the experimentally measured total nuclear heating rate. Only RMCCS flux will be used to obtain sensitivity profiles for each kerma factor library considered for comparison. The uncertainties on neutron and photon spectra were not available for all probes covered in the following section. We used four available uncertainty sets of neutron and photon spectra (for graphite, titanium, molybdenum, and tungsten) for each probe material other than these four and calculated the maximum uncertainty estimate of total nuclear heating for each set. Out of these four maximum estimates, we picked up the one with the largest magnitude and termed it the sensitivity estimate.

VI. RESULTS AND DISCUSSION

We will first present trends of C/E's, ratio of calculated to experimentally measured nuclear heating rates, for nine materials: graphite, titanium, copper, zirconium, niobium, molybdenum, tin, tungsten, and lead. Different kerma factor libraries have been employed with RMCCS based neutron and photon flux. Later, C/E − 1 will be compared to the sensitivity estimate of uncertainty on total nuclear heating (see Sec. V.C for explanation) for each of the nine materi-

als. In Secs. VI.A through VI.I, neutron/photon kerma factors and nuclear heating sensitivity profiles for different kerma factor libraries will be presented and discussed to clarify C/E trends for each material.

Table VII presents C/E's for single probe experiments done in 1991 for all materials except for copper, which was carried out in December 1989. This table shows results from practically all the response function libraries mentioned earlier. This table also shows the ratio of neutron heating to total nuclear heating for RMCCS, ENDL-85, MATXS10 (heat), and MATXS10 (kerma) response functions. An experimental error of ~10% is estimated for each material. The C/E's range from 0.43 ($1\sigma \approx 10\%$) to 3.41 ($1\sigma \approx 10\%$). Tungsten shows excellent agreement among all libraries used, and C/E's are very close to unity. Zirconium has the largest C/E spread from different libraries. The kerma factors are absent for tin in most of the libraries. The ratio of neutron heating to total nuclear heating varies from 95% (graphite) to −11% (molybdenum). Generally, this ratio drops as atomic number (Z) of the material rises. The negative number obtained for molybdenum, with MATXS10 (heat), is indicative of serious problems with neutron kerma factors for this material. In fact, the ratios for all four response functions disagree among themselves for this material.

VI.A. Graphite

Nuclear heating measurements were made with graphite single probes during experimental periods A, B, C, and D. During the period D, measurements were made for two geometric arrangements: (a) graphite microcalorimeter kept close to the target without any surrounding enclosure (bare, or without Li_2CO_3 enclosure), and (b) graphite microcalorimeter enclosed within

TABLE VII

Ratio of Computed to Experimental Nuclear Heating in Single Probes by Different Response Function Libraries

| Material | C/E, Ratio of Computed to Experimentally Measured Nuclear Heating Rates[a] | | | | | | | | | | |
	bmccs[b]	endl-85[b] (n to total)[c]	rmccs[b] (n to total)	endf/b-v[b]	matxs10 'heat' (n to total)	matxs10 'kerma' (n to total)	matxs5 'heat'	matxs5 'kerma'	kaoslib 'rec'	kaoslib 'rec + cpd'	jendl-3
Graphite	1.36 (0.96)[c]	1.20 (0.95)[c]	1.32 (0.95)[c]	1.32 (0.95)[c]	1.14 (0.94)[c]	1.14 (0.94)[c]	1.27	1.27	1.22	1.22	1.16 (0.94)[c]
Titanium	0.83 (0.45)	0.99 (0.54)	1.00 (0.54)	1.00 (0.54)	1.00 (0.54)	1.39 (0.66)	0.97 (0.53)[c]	1.35 (0.66)[c]	0.59 (0.24)[c]	0.60 (0.25)[c]	1.02 (0.56)
Copper	1.15 (0.42)	1.15 (0.42)	0.77 (7.3E−2)	0.77 (7.3E−2)	1.24 (0.42)	1.24 (0.42)	1.33	1.42	1.41	1.54	1.20
Zirconium	0.26 (0.14)	0.34 (0.34)	1.77 (0.88)	1.77 (0.88)	1.83 (0.87)	0.45 (0.47)	1.83	0.45	0.44	0.44	0.43
Niobium	0.75 (4.8E−2)	0.90 (0.20)	1.00 (0.28)	1.00 (0.28)	0.87 (0.17)	1.10 (0.35)	0.98	1.06	0.97	0.97	0.98
Molybdenum	0.81 (1.1E−2)	0.92 (0.13)	0.80 (3.8E−3)	0.80 (3.8E−3)	0.71 (−0.13)	0.91 (0.11)	0.71	0.91	0.91	0.92	1.08
Tin	3.41 (0.76)	0.95 (0.13)	0.95 (0.13)	---	---	---	---	---	---	---	---
Tungsten	---	1.00 (0.045)	1.01 (0.059)	---	1.01 (0.060)	1.00 (0.050)	1.01	1.00	1.00	1.00	0.99
Lead	1.63 (0.35)	1.11 (0.050)	1.60 (0.34)	1.60 (0.34)	1.14 (0.059)	1.14 (0.059)	1.33	1.13	1.13	1.13	1.13

[a]Experimental error ~10%.
[b]Continuous energy libraries used with MCNP.
[c]The bracketed numbers for a number of response function libraries yield ratios of neutron heating to total heating calculated by these respective libraries using flux through rmccs transport cross sections.

an annular enclosure made up of Li_2CO_3 and polyethylene, but such that there is no extraneous material between the target and the calorimeter (with Li_2CO_3 enclosure). The Li_2CO_3 enclosure was used simply to understand its impact on nuclear heating in the graphite probe. It was expected that there might be significant contributions coming from both neutrons and photons sent by the surrounding enclosure, on one hand, and a possible drop in nuclear heating due to reduction in room return, on the other. Figures 27 and 28 show how the neutron and gamma-ray spectra change in the presence of a Li_2CO_3 enclosure around the graphite calorimeter. Also shown for comparison in these figures are source spectra and spectra for a bare Li_2CO_3 probe (measuring 5.08 cm × 5.08 cm × 5.08 cm). All the spectra have been normalized to neutron flux, in the energy range of 15 to 13.5 MeV, so that one can compare the shapes of the spectra in the four cases considered. As for neutron spectrum changes, one can observe that, below source energy peak, there is a large enhancement in the neutron spectrum. However, the source neutrons still dominate the overall neutron spectrum. As for gamma-ray spectra, there is an enhancement in overall number of photons. But, there is very small increase in energy range with most of the photons lying between ~0.1 to ~6 MeV. On the whole, one

expects little change in nuclear heating in the graphite probe with or without the Li_2CO_3 enclosure.

As shown in Table VII, C/E's for graphite range from 1.14 (MATXS10) to 1.36 (BMCCS). The BMCCS
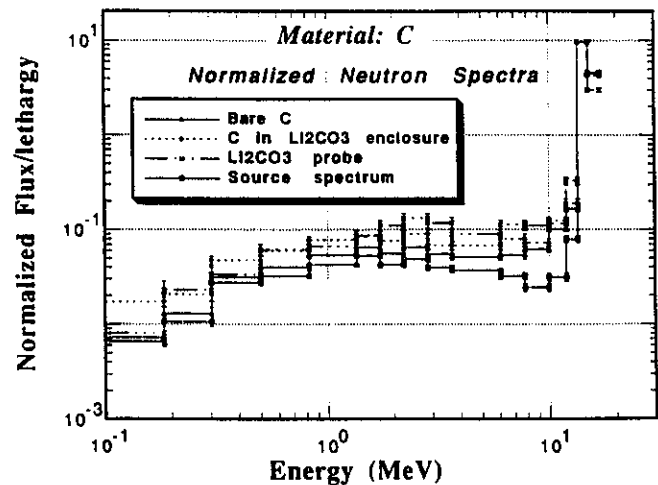

Fig. 27. Normalized neutron spectra for a graphite probe with and without Li_2CO_3 enclosure and its comparison to source spectrum.
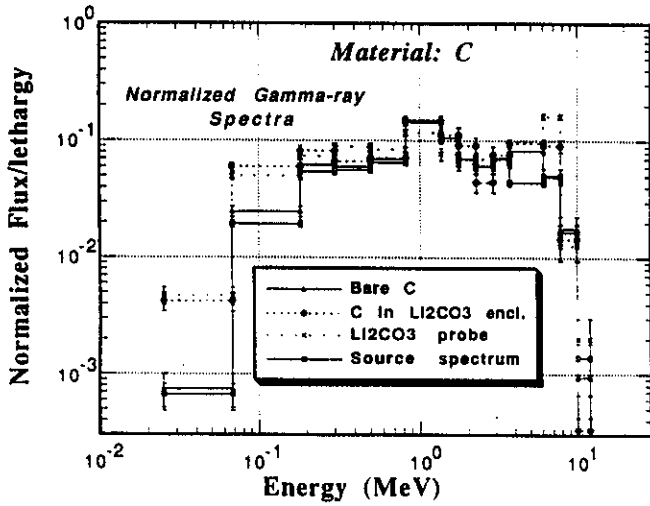
Fig. 28. Normalized gamma-ray spectra for a graphite probe with and without Li_2CO_3 enclosure and its comparison to source spectrum.

overprediction can be ascribed to the largest neutron kerma factors for this library in the important energy region above 10 MeV. Neutron kerma factors are compared in Fig. 29 for ENDL-85, MATXS10-heat, MATXS5-heat, and JENDL-3 libraries. The kerma factors have very strong dependence on neutron energy: the kerma factor is $\sim 2 \times 10^{-13}$ J·b close to 10 MeV and drops by five orders to $\sim 10^{-18}$ J·b as neutron energy drops by six orders to 10^{-5} MeV. There is a region of large differences between ~ 3 to ~ 10 MeV energy region. MATXS10-heat and ENDL-85 are generally close to each other. JENDL-3 kerma factors are systematically lower than those from MATXS10-heat in energy
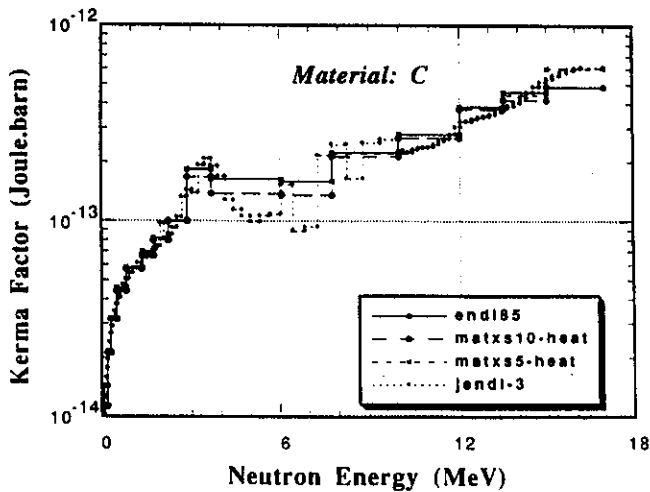
range extending from ~ 10 to ~ 13 MeV, but the trend reverses above ~ 14 MeV. MATXS5-heat kerma factors are close to those from MATXS10-heat except above 15 MeV. In the topmost energy group, from 15 to 17 MeV, the kerma factor in the former is almost 20% larger than the one in the latter. Let us now look at relative values of neutron kerma factor integrals (see Tables III and IV). Table III shows that BMCCS has the largest KI_n of 5.20×10^{-14} J·b, as against the lowest value of 4.14×10^{-14} J·b for MATXS10, explaining largely the reason for discrepancies among various libraries.

The kerma factors for photons are shown in Fig. 30 for MATXS10, MCPLIB, and JENDL-3. It is to be noted that the lowest photon kerma factor is above $\sim 3 \times 10^{-15}$ J·b for photon energy lying in the range of ~ 0.02 to ~ 0.1 MeV. It is to be compared to neutron kerma factor of $\sim 10^{-15}$ J·b at $\sim 10^{-2}$ MeV. Thus, whereas the neutron kerma factor for graphite continues to drop rapidly below $\sim 10^{-2}$ MeV, the photon kerma factor starts rising once again as photon energy continues to fall below ~ 0.02 MeV. This difference in energy dependence of kerma factors is found to exist for all materials being discussed in this work. Its implications are very important for situations where photon heating is an important component of total nuclear heating. In these situations, it is important to compute photon energy spectra in the entire energy range. For example, if one were to ignore lower energy neutrons, say below 10^{-3} MeV, for their contribution to neutron heating due to quite low kerma factors, it might lead to underprediction of photons resulting from (n,γ) reactions, and, hence, overall photon heating in a probe. Eventually, it might lead to underprediction of C/E for total heating in certain situations.

Fig. 29. Neutron kerma factors for graphite as a function of energy for ENDL-85, MATXS10-heat, MATXS5-heat, and JENDL-3 libraries.
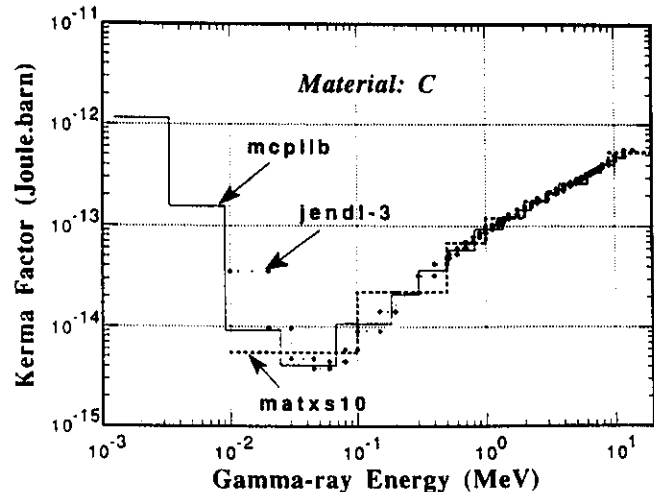

Fig. 30. Gamma-ray kerma factors for graphite as a function of energy for MCPLIB, MATXS10, and JENDL-3 libraries.

Sensitivity profiles for total nuclear heating for neutrons and photons are quite important in understanding possible sources of discrepancies between calculations and measurements. Figure 31 shows nuclear heating sensitivity profile, $P_n^j(u)$'s, for graphite as a function of neutron energy for ENDL-85, MATXS10-heat, and JENDL-3. It is important to see that the sensitivity drops more than two orders as neutron energy drops to 10 MeV. In other words, source neutron energy groups essentially determine the neutron component of total nuclear heating. A sensitivity profile for the photon component of the nuclear heating, say $P_g^j(u)$, is produced in Fig. 32 for MCPLIB and MATXS10. The largest γ-sensitivity occurs between ~3 to ~9 MeV, but it is two orders lower than the largest n-sensitivity. In other words, total nuclear heating in graphite is dominated by neutrons. This is also borne out by the fractional neutron heating values provided in Table VII, which show as much as ~95% contribution to total heating from neutrons.

The preponderance of neutron heating fraction in total heating in graphite could be exploited to develop and calibrate a graphite based calorimeter to obtain the neutron heating fraction of total heating in any other probe material subjected to D-T neutron field.

VI.B. Titanium

Nuclear heating measurements were made with titanium single probes during experimental periods C and D. As shown in Table VII, C/E's for titanium range from 0.62 (KAOSLIB-rec) to 1.41 (MATXS10-kerma). It appears that this large variation is mostly attributable to large differences in neutron kerma factors for different libraries. As shown in Table III, the neutron kerma factor integrals for different libraries show large
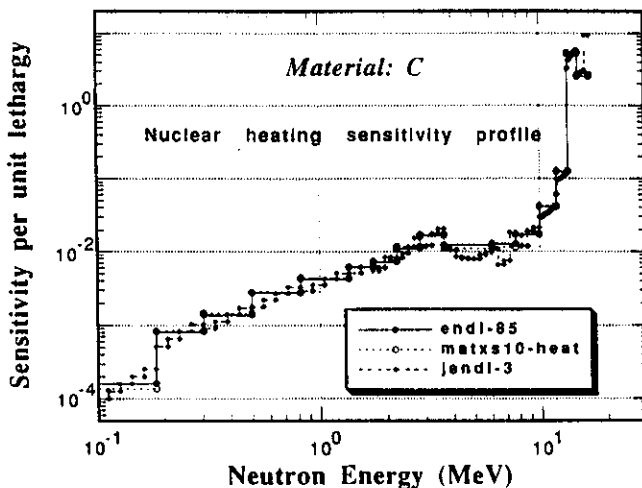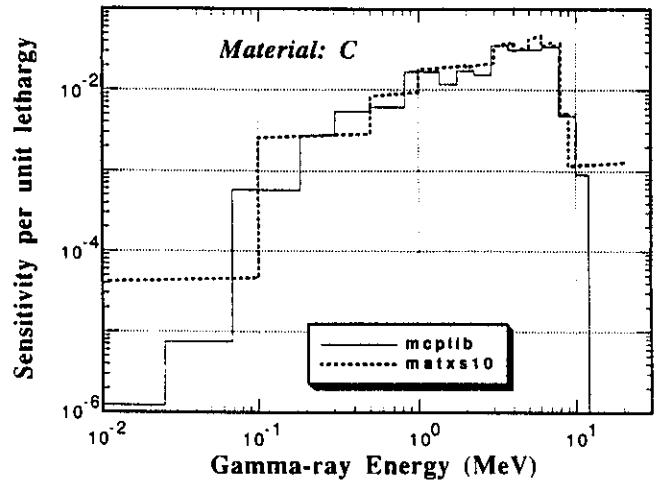

Fig. 32. Nuclear heating sensitivity profile, $P_g^j(u)$, for graphite as a function of gamma-ray energy for MCPLIB, and MATXS10 libraries.

differences, from the lowest value of 5.27×10^{-15} J·b for KAOSLIB-rec, to the largest value of 3.525×10^{-14} J·b for MATXS10-kerma. Neutron kerma factors are compared in Fig. 33 for ENDL-85, MATXS10-heat, MATXS10-kerma, and JENDL-3 libraries. JENDL-3 and ENDL-85 kerma factors appear to be close above 9 MeV. MATXS10-heat and ENDL-85 kerma factor curves cross around 12 MeV and 15 MeV, and below 10 MeV the difference between them rises. MATXS10-kerma values are as much as 30-50% higher above those from MATXS10-heat in the energy range above 8 MeV. KAOSLIB kerma factors show very odd behavior. In fact, the kerma factors from this library start declining beginning at 12 MeV and rise again at 15 MeV, whereas for all other libraries the kerma factors continue to rise between 12 and 17 MeV.

The kerma factors for photons are shown in Fig. 34 for MCPLIB, MATXS10, and JENDL-3. It is to be noted that the lowest photon kerma factor is above $\sim 10^{-13}$ J·b for photon energy lying in the range of ~0.2 to ~0.3 MeV. It is to be compared to the neutron kerma factor of $\sim 10^{-13}$ J·b at 9 MeV. The photon kerma factor integral for MATXS10 is 5.6% larger than the one for MCPLIB (see Table V). Comparing the photon kerma factor integral for the 10 MeV to 0.1 MeV range (see Table V) to the neutron kerma factor integral for 14.92 to 13.5 MeV (see Table III) for MATXS10-heat library, one finds a ratio of 145. It implies that even a small amount of photon flux, say a percent of the neutron flux, in the titanium medium can give rise to photon heating rates comparable to those for the neutron heating.

Figure 35 shows the nuclear heating sensitivity profile, $P_n^j(u)$'s, for titanium as a function of neutron energy for ENDL-85, MATXS10-heat, and JENDL-3. As noted earlier for graphite, sensitivity drops more than
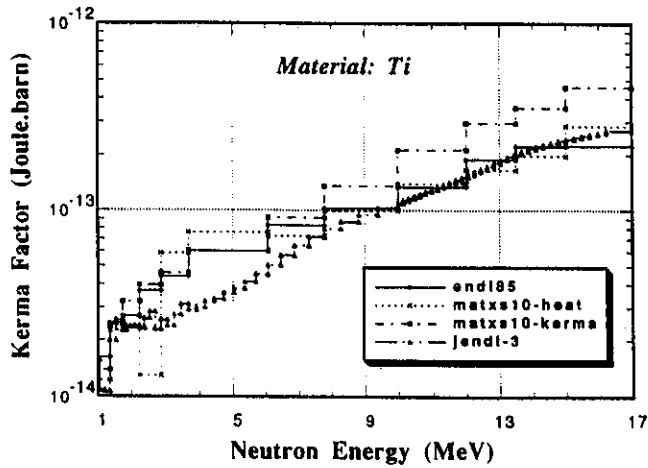

Fig. 31. Nuclear heating sensitivity profile, $P_n^j(u)$, for graphite as a function of neutron energy for ENDL-85, MATXS10-heat, and JENDL-3 libraries.

Fig. 33. Neutron kerma factors for titanium as a function of energy for ENDL-85, MATXS10-heat, MATXS10-kerma, and JENDL-3 libraries.

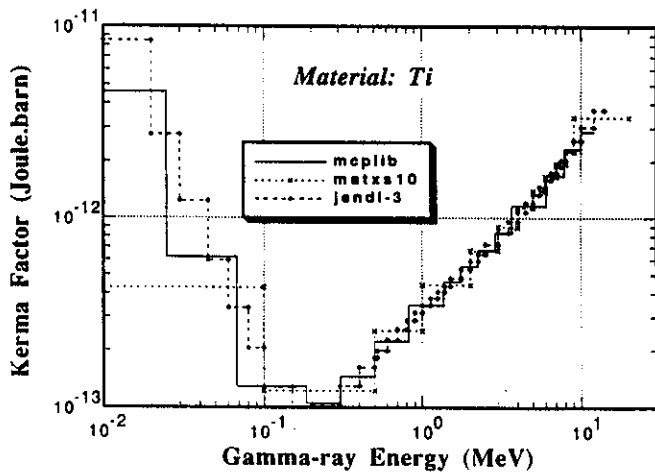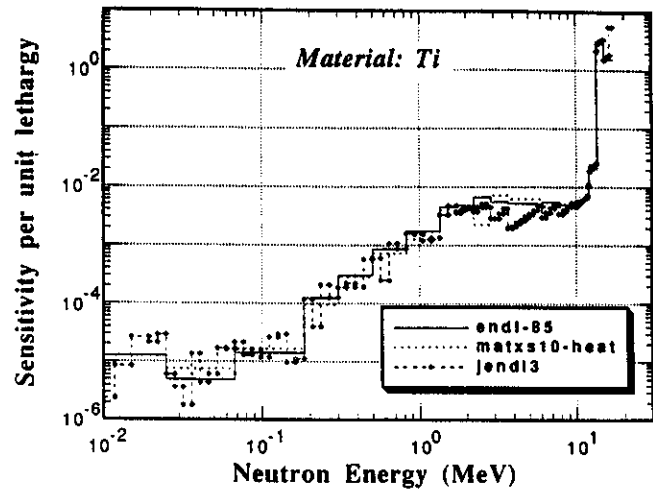Fig. 35. Nuclear heating sensitivity profile, $P_n^j(u)$, for titanium as a function of neutron energy for ENDL-85, MATXS10-heat, and JENDL-3 libraries.
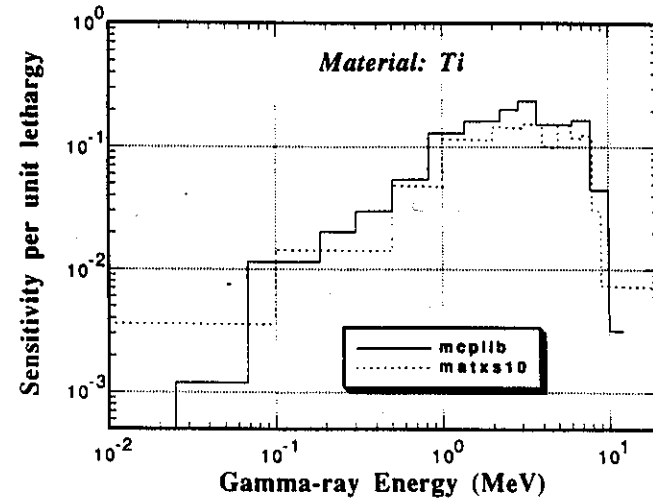

Fig. 34. Gamma-ray kerma factors for titanium as a function of energy for MCPLIB, MATXS10, and JENDL-3 libraries.

Fig. 36. Nuclear heating sensitivity profile, $P_g^j(u)$, for titanium as a function of gamma-ray energy for MCPLIB, and MATXS10 libraries.

two orders as neutron energy drops to 10 MeV. It is relatively flat from 10 to 2 MeV, and thereafter it drops speedily. A sensitivity profile for the photon component of the nuclear heating, $P_g^j(u)$, is provided in Fig. 36 for MCPLIB and MATXS10. The largest γ-sensitivity occurs between ~3 to ~4 MeV, and it is only one order lower than the largest n-sensitivity. In other words, though total nuclear heating in titanium is largely contributed to by neutrons, there is an appreciable contribution from photons too. This is also borne out by the fractional neutron heating values provided in Table VII, which show as much as ~46% contribution to total heating from photons.

VI.C. Copper

Measurements were made with copper single probes during experimental periods A and B. As shown in Table VII, C/E's for copper range from 0.77 (RMCCS/ENDF5) to 1.54 (KAOSLIB-rec+cpd). This large variation arises due to large differences in neutron kerma factors for different libraries. As shown in Table III, the neutron kerma factor integrals for different libraries show large differences. They range from 3.85 × 10^{-15} J·b for RMCCS/ENDF5 to 5.17 × 10^{-14} J·b

for KAOSLIB-rec+cpd. Neutron kerma factors are compared in Fig. 37 for ENDL-85, RMCCS, MATXS10-heat, MATXS5-heat, and JENDL-3 libraries. JENDL-3 and ENDL-85 kerma factors are close above ~0.2 MeV. RMCCS values oscillate a lot about ENDL-85 curve. Surprisingly, RMCCS hits a peak around 10 to 12 MeV and then drops precipitously between 13.5 to 15 MeV. MATXS5-heat oscillates around ENDL-85 and even turns negative around 1.5 MeV.

The photon kerma factors are shown in Fig. 38 for MCPLIB and MATXS10. It is to be noted that the lowest photon kerma factor is ~2 × 10⁻¹³ J·b for photon energy lying in the range of ~0.2 to ~0.3 MeV. It is to be compared to neutron kerma factor of ~2 × 10⁻¹³ J·b at 10 MeV (for ENDL-85). The photon kerma factor integral for MATXS10 is 6.9% larger than the one for MCPLIB (see Table V). Comparing the photon

kerma factor integral for 10 MeV to 0.1 MeV range (see Table V) to the neutron kerma factor integral for 14.92 to 13.5 MeV (see Table III), for ENDL-85 library, one finds a ratio of 121. It implies that even a little photon flux, say one percent of the neutron flux, in the copper medium can give rise to a photon heating rate comparing favorably to that for neutron heating.

Nuclear heating sensitivity profile, $P_n^i(u)$, is shown in Fig. 39 for copper as a function of neutron energy for ENDL-85, MATXS10-heat, and JENDL-3. The neutron-sensitivity to total nuclear heating falls more than two orders as neutron energy drops to 10 MeV. The peak sensitivity value of ~2.5 per unit lethargy occurs at a source neutron group (15 to 13.5 MeV) for ENDL-85. It has a relatively flat value of ~3 × 10⁻³ per unit lethargy, in the energy range extending from ~10 to ~2 MeV, and thereafter it starts declining quite fast. The photon component of the nuclear heating sensitivity profile, $P_g^j(u)$, is provided in Fig. 40 for MCPLIB and MATXS10. The highest γ-sensitivity of ~0.4 per unit lethargy occurs between ~3 to ~4 MeV, and it is just a factor of ~6 lower than the largest neutron-sensitivity. Thus photons can also be anticipated to contribute fairly to total nuclear heating. This is further reinforced by the fractional neutron heating values provided in Table VII, which show as much as ~58% contribution to total heating from photons (for ENDL-85). Note that the rather low value of neutron heating fraction for RMCCS is directly related to its abysmally low neutron kerma factors in the source neutron energy region.

VI.D. Zirconium

The measurements of total nuclear heating were done with a single probe of zirconium during experimental period D. It is to be noted that unlike single
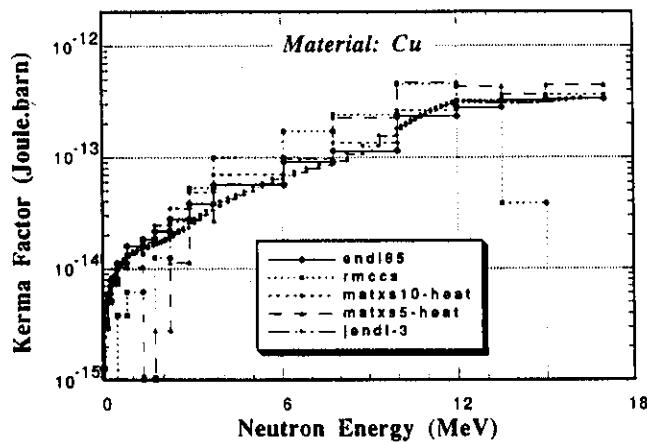

Fig. 37. Neutron kerma factors for copper as a function of energy for ENDL-85, RMCCS, MATXS10-heat, MATXS5-heat, and JENDL-3 libraries.

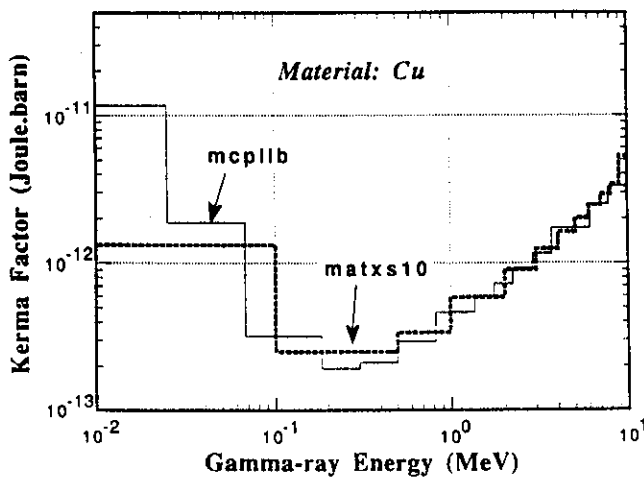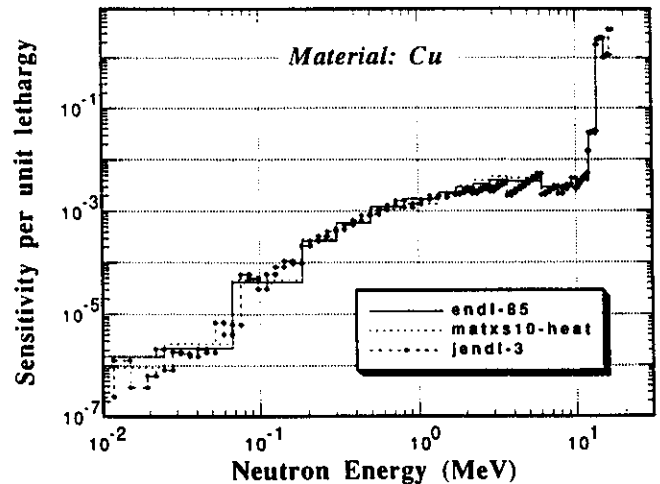Fig. 38. Gamma-ray kerma factors for copper as a function of energy for MCPLIB, and MATXS10 libraries.

Fig. 39. Nuclear heating sensitivity profile, $P_n^i(u)$, for copper as a function of neutron energy for ENDL-85, MATXS10-heat, and JENDL-3 libraries.
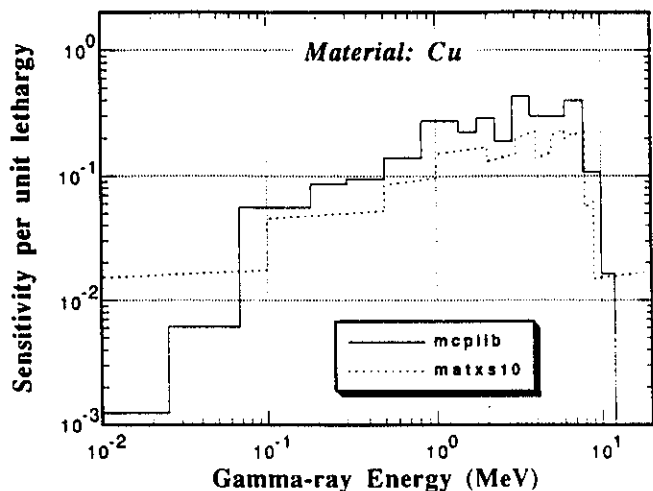
Fig. 40. Nuclear heating sensitivity profile, $P_g^j(u)$, for copper as a function of gamma-ray energy for MCPLIB, and MATXS10 libraries.

The problems with zirconium kerma factors are exemplified by the fact that MATXS10-heat are an order or so larger than MATXS10-kerma even though the latter are designed to exceed the former. This is probably due to lack of energy conservation in ENDF/B-VI files.[5,30]

The photon kerma factors are shown in Fig. 42 for MATXS10. It is to be noted that the lowest photon kerma factor is ~5 × 10⁻¹³ J·b for photon energy lying in the range of 0.5 to 1 MeV. It is to be compared to neutron kerma factor of ~9 × 10⁻¹⁴ J·b at 14 MeV (for ENDL-85). While comparing photon kerma factor integral for 10 MeV to 0.1 MeV range for MATXS10 (see Table V) to neutron kerma factor integral for 14.92 to 13.5 MeV (see Table III), for ENDL-85 library, one finds a ratio of 810. The similar ratio for MATXS10-heat is only 57. It appears that none of the two ratios is reasonable. Perhaps a more realistic ratio will lie between these two. In other words, more sensible neutron

pieces of material for most of the probes, we used a stack of multiple small but identical pieces of material for constructing the probe of zirconium. Due to lack of proper thermal conduction from one piece to another in the zirconium probe thus constructed, differences were observed in spatial heat deposition rates inside this probe. For this reason, we will be considering only RTD measurements as the appropriate data for comparison to the calculation. This is justified as the RTD sensor was placed laterally along the entire length of the probe and was in good thermal contact with each component piece of the probe. In a sense, the RTD provides correct volumic average of total heat deposition. As shown in Table VII, C/E's for zirconium range from 0.3 (BMCCS/ENDL-85) to 1.8 (RMCCS/MATXS10-heat/MATXS5-heat). This enormous difference is due to large variations in neutron kerma factors for various libraries. There appear to be two distinct groups of C/E's. The first group has C/E's ranging from 0.26 to 0.44 and contains 7 libraries that include ENDL-85, BMCCS, MATXS10-kerma, MATXS5-kerma, KAOS-LIB-rec, KAOSLIB-rec+cpd, and JENDL-3. The second group has C/E's ranging from 1.77 to 1.83 and has 4 libraries including RMCCS, MATXS10-heat, and MATXS5-heat. The neutron kerma factor integrals (see Table III) show large differences. They range from 2.68 × 10⁻¹⁵ J·b for BMCCS to 1.25 × 10⁻¹³ J·b for MATXS10-heat and MATXS5-heat. Neutron kerma factors are compared in Fig. 41 for ENDL-85, RMCCS, MATXS10-heat, MATXS10-kerma, and JENDL-3 libraries. JENDL-3, ENDL-85, and MATXS10-kerma values are close above ~0.2 MeV. RMCCS and MATXS10-heat values are quite close to each other and lie way above ENDL-85 curve in the entire neutron energy range of interest. Also, RMCCS hits a broad peak between 8 and 10 MeV and then drops on either side.
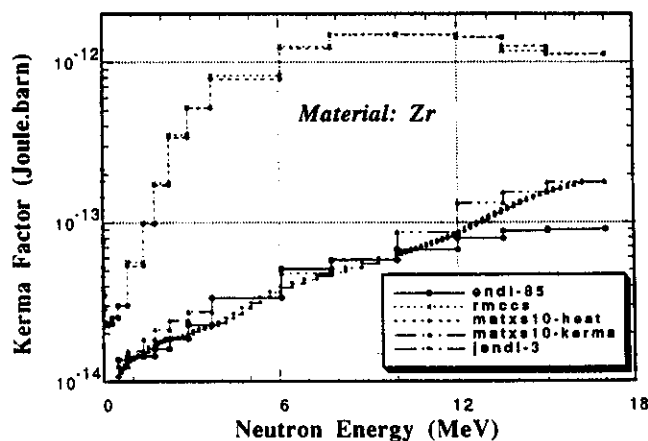

Fig. 41. Neutron kerma factors for zirconium as a function of energy for ENDL-85, RMCCS, MATXS10-heat, MATXS10-kerma, and JENDL-3 libraries.
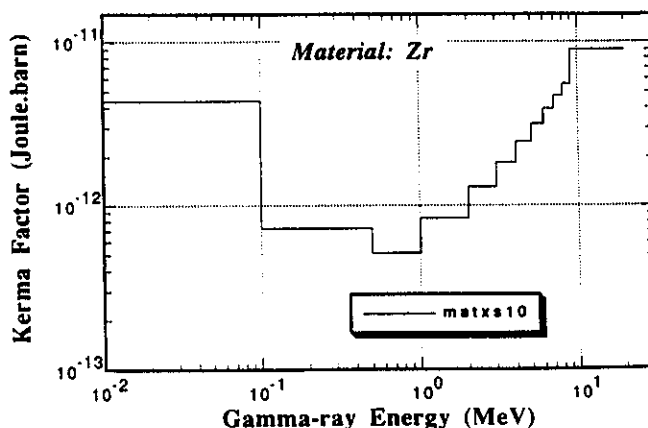

Fig. 42. Gamma-ray kerma factors for zirconium as a function of energy for MCPLIB library.

kerma factors will lie between the two sets of the neutron kerma factors as discussed earlier.

Neutron component of nuclear heating sensitivity profile, $P_n^i(u)$, is shown in Fig. 43 for zirconium as a function of neutron energy for ENDL-85, MATXS10-heat, and JENDL-3. The neutron-sensitivity tumbles more than two orders as neutron energy goes down to 10 MeV from 14 MeV. The peak sensitivity value of ~6 per unit lethargy occurs at a source neutron group (15 to 13.5 MeV) for MATXS10-heat. It has a relatively flat value of ~3 × 10^{-2} per unit lethargy, in the energy range extending from ~8 to ~2 MeV, and then it starts dropping rapidly as the neutron energy drops further. The gamma-ray component of nuclear heating sensitivity profile, $P_g^j(u)$, is provided in Fig. 44 for MATXS10. The highest γ-sensitivity of ~0.3 per unit lethargy occurs between ~7 to ~8 MeV, and it is a factor of ~20 lower than the largest neutron-sensitivity. Thus photons are capable of making significant contribution to total nuclear heating in zirconium. This inference is further strengthened by the fractional neutron heating values provided in Table VII, which show neutron contributions varying from 13% (BMCCS) to 88% (RMCCS/MATXS10-heat). The rather high value of the neutron heating fraction for RMCCS/MATXS10-heat is directly related to the abnormally high neutron kerma factors in the entire neutron energy region of significance.

VI.E. Niobium

Nuclear heating measurements were made with niobium single probes during experimental period D. As shown in Table VII, C/E's for niobium range from 0.75 (BMCCS) to 1.10 (MATXS10-kerma). The C/E differ-
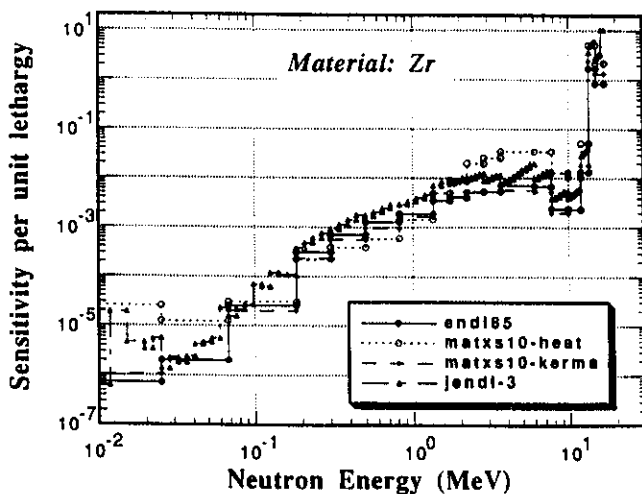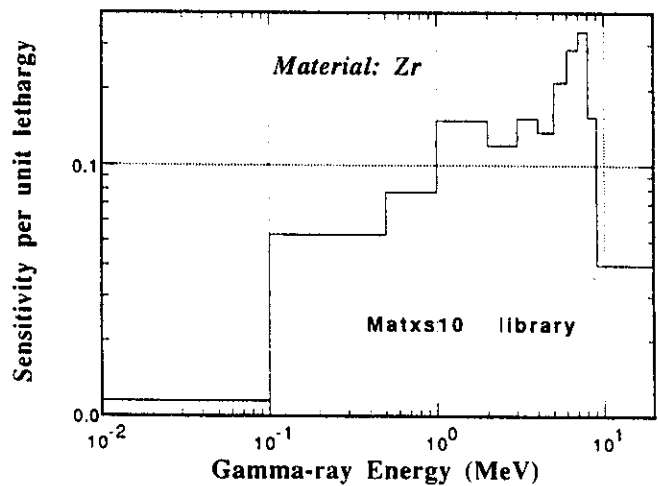

Fig. 44. Nuclear heating sensitivity profile, $P_g^j(u)$, for zirconium as a function of gamma-ray energy for MCPLIB library.

ences are rather moderate. The observed variation is attributable to differences in neutron kerma factors for various libraries. Tables III and IV show neutron kerma factor integrals for some of the libraries. As seen from Table III, the neutron kerma factor integrals range from 4.72 × 10^{-15} J·b for MATXS10-heat to 2.05 × 10^{-14} J·b for MATXS10-kerma. Neutron kerma factors are compared in Fig. 45 for MATXS10-heat, MATXS10-kerma, KAOSLIB-rec, and JENDL-3 libraries. The JENDL-3 and KAOSLIB-rec kerma factors are generally close. The MATXS10-kerma values lie much above JENDL-3 in the energy region from 10 to 17 MeV. In fact, for 14.92 to 13.5 MeV, the MATXS10-kerma

Fig. 43. Nuclear heating sensitivity profile, $P_n^i(u)$, for zirconium as a function of neutron energy for ENDL-85, MATXS10-heat, MATXS10-kerma, and JENDL-3 libraries.
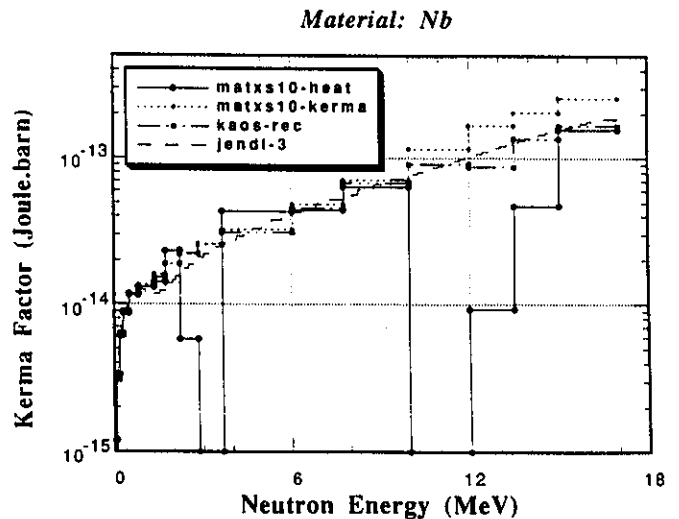

Fig. 45. Neutron kerma factors for niobium as a function of energy for MATXS10-heat, MATXS10-kerma, KAOSLIB-rec, and JENDL-3 libraries.

value is as much as ~46% larger. As for MATXS10-heat, it oscillates violently. For example, it is close to JENDL-3 between 17 and 15 MeV and then starts dropping fast and turns negative between 12 and 10 MeV. It rises again at 10 MeV and hovers around JENDL-3, MATXS10-kerma, and KAOSLIB-rec before turning negative once more between 3.6 and 2.9 MeV.

The photon kerma factors for MATXS10 are shown in Fig. 46. It is to be noted that the lowest photon kerma factor is $\sim 5 \times 10^{-13}$ J·b for photon energy lying in the range of 0.5 to 1 MeV. Compare it to JENDL-3 neutron kerma factor of 1.4×10^{-13} J·b for 14.92 to 13.5 MeV. The dominance of photons stands out. While comparing the photon kerma factor integral for MATXS10 for the 10 MeV to 0.1 MeV range (see Table V) to the neutron kerma factor integral for 14.92 to 13.5 MeV (see Table III) for the JENDL-3 library, one finds a ratio of 531! It implies that even a tiny amount of photon flux, say one or two percent of the neutron flux, in the niobium medium can produce a photon heating rate that is comparable to the neutron heating.

Figure 47 shows the nuclear heating sensitivity profile, $P_n^j(u)$'s, for niobium as a function of neutron energy for MATXS10-heat, MATXS10-kerma, KAOSLIB-rec, and JENDL-3. These profiles are largely driven by the respective kerma factors. Peak sensitivity value of ~2, for MATXS10-kerma, occurs in 15 to 13.5 energy region. The profile is almost flat from 10 to ~0.5 MeV, and thereafter it drops. The sensitivity is $\sim 10^{-3}$ in this region. Sensitivity profile for photon component of the nuclear heating, $P_g^j(u)$, is provided in Fig. 48 for MATXS10. The largest γ-sensitivity of ~0.25 occurs between ~3 to ~2 MeV, and it is approximately one order lower than the largest neutron-sensitivity. This portends relatively significant contribution from the γ's. This is also borne out by the
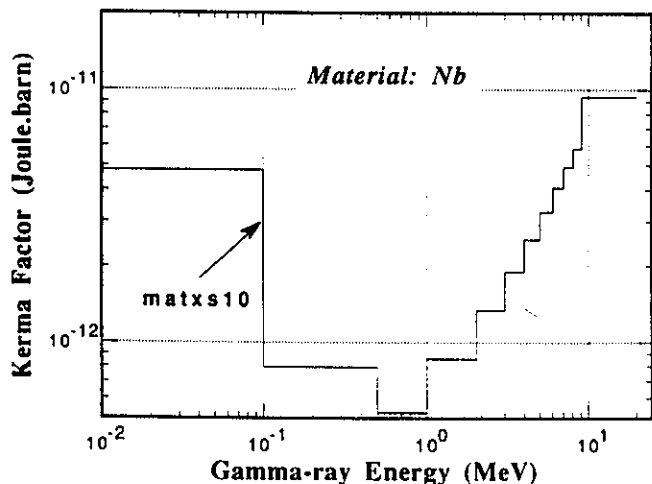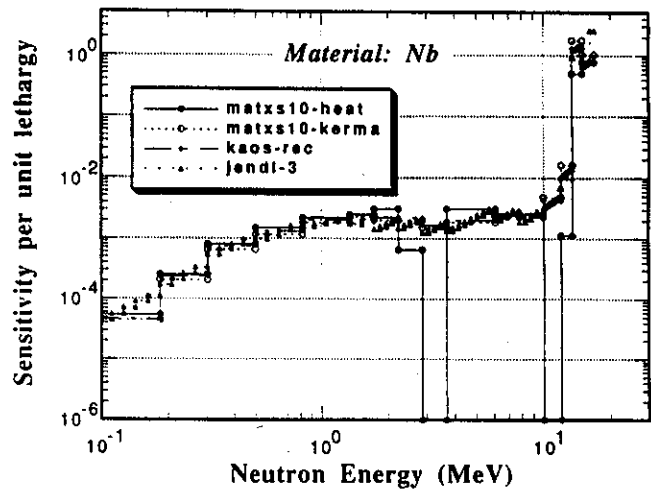

Fig. 47. Nuclear heating sensitivity profile, $P_n^j(u)$, for niobium as a function of neutron energy for MATXS10-heat, MATXS10-kerma, KAOSLIB-rec, and JENDL-3 libraries.
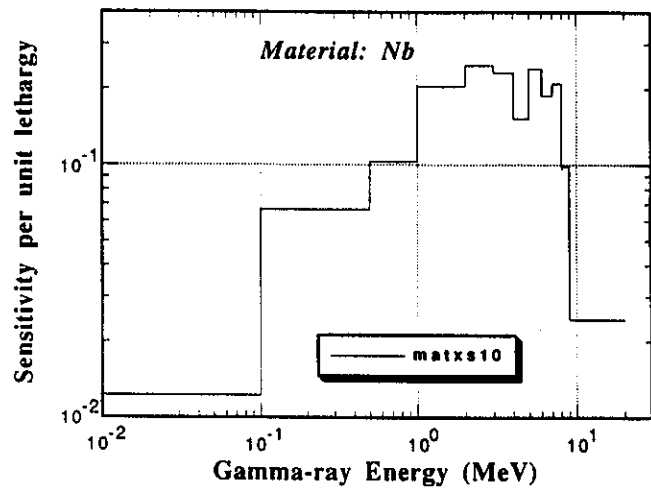

Fig. 48. Nuclear heating sensitivity profile, $P_g^j(u)$, for niobium as a function of gamma-ray energy for MATXS10 library.

fractional neutron heating values provided in Table VII, which range from 4.8% (BMCCS) to 35% (MATXS10-kerma). Obviously, neutron heating component has a large discrepancy among different libraries, and needs improvement. The ENDF/B-VI kerma factors provided in the form of MATXS10-heat are inadequate.

VI.F. Molybdenum

The nuclear heating measurements were made with single molybdenum probes during experimental periods C and D. As shown in Table VII, C/E's for molybdenum range from 0.71 (MATXS10-heat,

Fig. 46. Gamma-ray kerma factors for niobium as a function of energy for MATXS10 library.

MATXS5-heat) to 1.08 (JENDL-3). This variation is attributable to very large differences in neutron kerma factors for different libraries. As shown in Table III, neutron kerma factor integrals go from -3.34×10^{-15} J·b for MATXS10-heat to 1.68×10^{-14} J·b for JENDL-3. Neutron kerma factors are compared in Fig. 49 for ENDL-85, RMCCS, MATXS10-heat, MATXS10-kerma, and JENDL-3 libraries. MATXS10-kerma and ENDL-85 kerma factors appear to be quite close. JENDL-3 stays around ENDL-85 from $\sim 10^{-2}$ through ~ 1 MeV, and is considerably below ENDL-85 between 2 to 3 MeV. It rises rapidly and overtakes ENDL-85 and is significantly larger at 6 MeV. Above 12 MeV, JENDL-3 kerma is way above. RMCCS and MATXS10-heat kerma factors oscillate wildly. RMCCS drops to zero between 15 to 13.5 MeV. MATXS10-heat stays continuously negative from 17 to 7.8 MeV!

The kerma factors for photons are shown in Fig. 50 for MATXS10. It is to be noted that the lowest photon kerma factor is $\sim 5 \times 10^{-13}$ J·b for photon energy lying in the range of ~ 0.1 to ~ 0.5 MeV. It is to be compared to neutron kerma factor of $\sim 7 \times 10^{-14}$ J·b for 14.92 to 13.5 MeV. When we compare photon kerma factor integral, for MATXS10, for 10 MeV to 0.1 MeV range (see Table V) to neutron kerma factor integral for 14.92 to 13.5 MeV (see Table III), for ENDL-85 library, one finds a ratio of 1109! It is obvious that there will always be a significant contribution from γ's to total nuclear heating.

Nuclear heating sensitivity profiles, $P_n^i(u)$'s, for molybdenum as a function of neutron energy are shown in Fig. 51 for ENDL-85, RMCCS, MATXS10-heat, MATXS10-kerma, and JENDL-3. The peak sensitivity has a value of ~ 0.7 for 15 to 13.5 MeV for ENDL-85. The sensitivity for ENDL-85 averages $\sim 2 \times 10^{-3}$ in relatively flat region extending from 10 to 0.5 MeV,
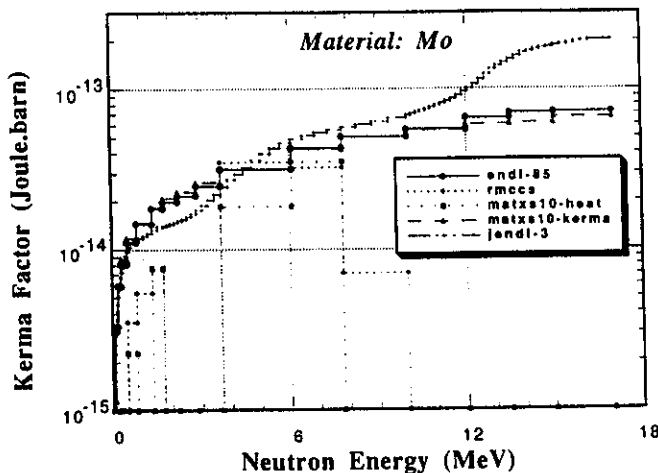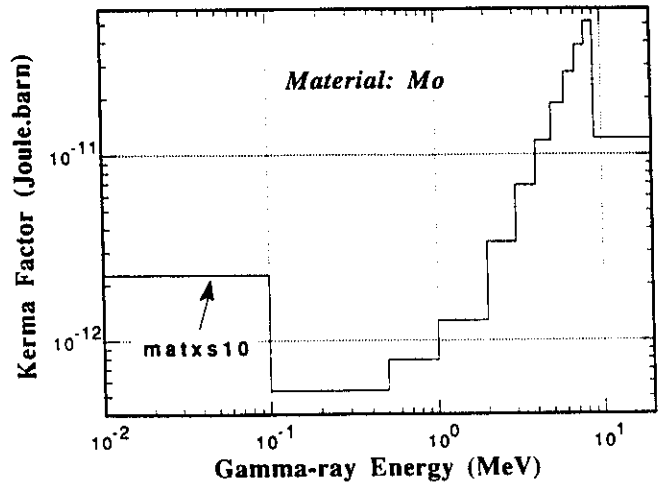

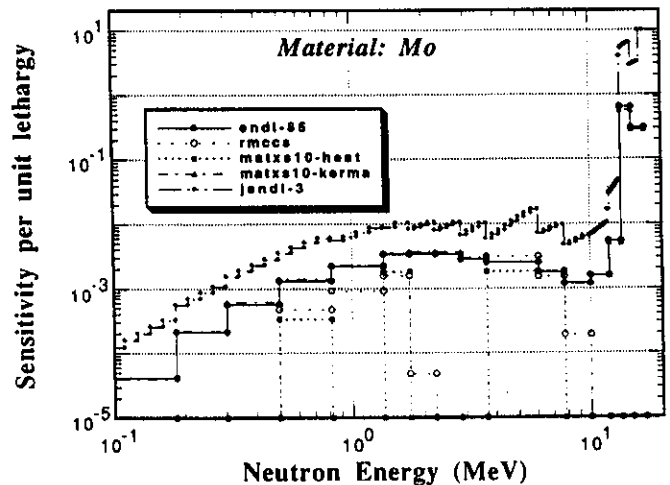Fig. 50. Gamma-ray kerma factors for molybdenum as a function of energy for MATXS10 library.

Fig. 51. Nuclear heating sensitivity profile, $P_n^i(u)$, for molybdenum as a function of neutron energy for ENDL-85, RMCCS, MATXS10-heat, MATXS10-kerma, and JENDL-3 libraries.

and thereafter it drops continuously. Sensitivity profile for photons appears in Fig. 52 for MATXS10. The largest γ-sensitivity value of ~ 0.4 occurs between 6 to 5 MeV, and it is almost a factor of 2 lower than the largest neutron sensitivity. The strong component of photon heating to total nuclear heating is evident for molybdenum. Also the fractional neutron heating values provided in Table VII confirm the important role of the γ's. The neutron heating varies from -13% (MATXS10-heat) to 13% (ENDL-85). MATXS10-heat prediction of neutron heating is definitely wrong as kerma factors were negative for a range of neutron energies, including the source energy range!
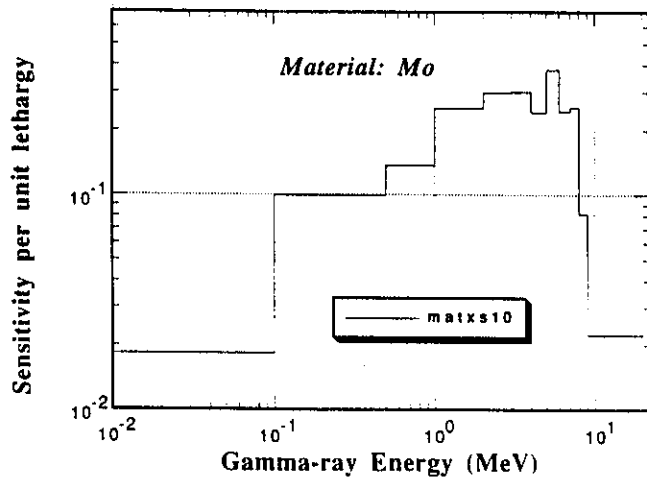

Fig. 49. Neutron kerma factors for molybdenum as a function of energy for ENDL-85, RMCCS, MATXS10-heat, MATXS10-kerma, and JENDL-3 libraries.

Fig. 52. Nuclear heating sensitivity profile, $P_g^j(u)$, for molybdenum as a function of gamma-ray energy for MATXS10 library.

VI.G. Tin

Total nuclear heating measurements in single probes of tin were carried out during experimental period D. Only two libraries were available for tin: ENDL-85, and BMCCS (or ENDL-73). C/E's for tin are respectively 0.95 (ENDL-85) and 3.41 (BMCCS), as shown in Table VII. The huge discrepancy between the two libraries is due to large differences in their neutron kerma factors. Neutron kerma factor integrals for the two libraries differ by a factor of 20 (see Table III), the integrals being 5.90×10^{-15} J·b (ENDL-85), and 1.22×10^{-13} J·b (BMCCS). BMCCS KI_n appears to be excessively high! Figure 53 shows plots of neutron kerma factors from ENDL-85 and BMCCS. BMCCS values are systematically larger than those by ENDL-
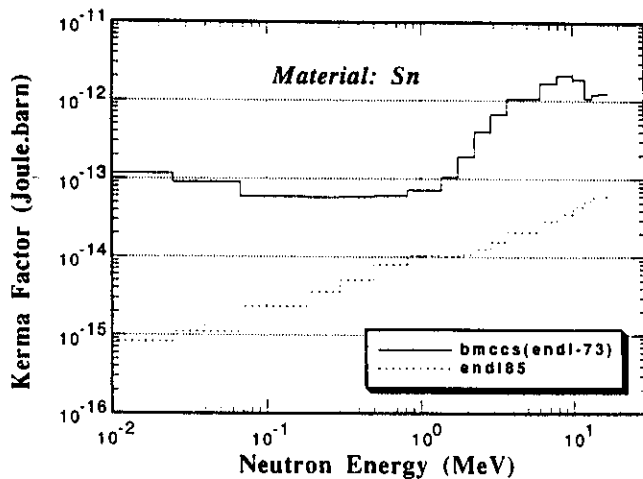
85. The kerma factors are closest around ~1 MeV and differ by a factor of ~7 only. The BMCCS values become as much as 100 times those by ENDL-85!

Figure 54 shows photon kerma factors from MCPLIB. The lowest photon kerma factor is above $~6.5 \times 10^{-13}$ J·b for photon energy lying in the range of 0.8 to 0.5 MeV. For perspective, it is important to note that it is even larger than the largest neutron kerma factor value of $~5.9 \times 10^{-14}$ J·b (15 to 13.5 MeV group) for ENDL-85. From comparison of photon kerma factor integral for 10 MeV to 0.1 MeV range (see Table V) to neutron kerma factor integral for 14.92 to 13.5 MeV (see Table III), for ENDL-85, one finds a ratio of 1654. It follows that photons are destined to contribute, in a very significant measure, to overall nuclear heating in a tin probe .

Figure 55 shows nuclear heating sensitivity profile, $P_n^j(u)$'s, for tin as a function of neutron energy for ENDL-85 and BMCCS. Peak sensitivity of ~0.7 per unit lethargy, for ENDL-85, occurs for a source neutron group going from 15 to 13.5 MeV. Sensitivity profile for photon component of the nuclear heating, $P_g^j(u)$, is plotted in Fig. 56 for MCPLIB. The largest γ-sensitivity value of ~0.4 per unit lethargy occurs between ~8 to ~6 MeV, and it is approximately a factor of two lower than the largest neutron sensitivity. Clearly, photons contribute strongly to total nuclear heating for our experimental conditions. The fractional neutron heating values from Table VII support this observation. The photon heating is 88% by ENDL-85. BMCCS prediction of only 25% photon contribution appears off due to apparently large neutron kerma factors that act to raise neutron heating.

VI.H. Tungsten

Nuclear heating measurements were made with graphite single probes during experimental periods B,

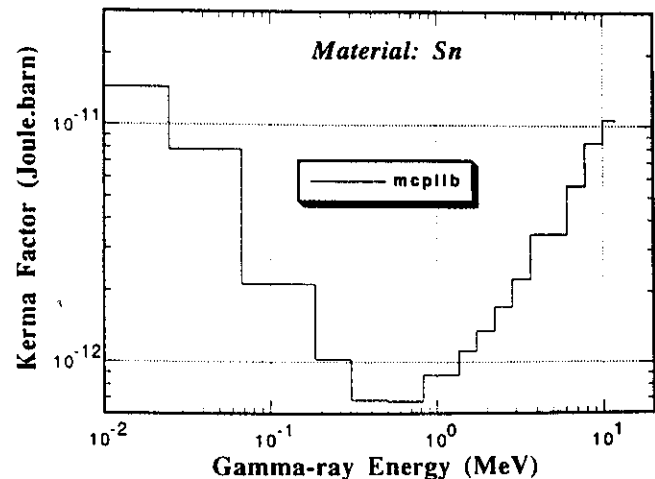Fig. 53. Neutron kerma factors for tin as a function of energy for ENDL-85, and BMCCS libraries.

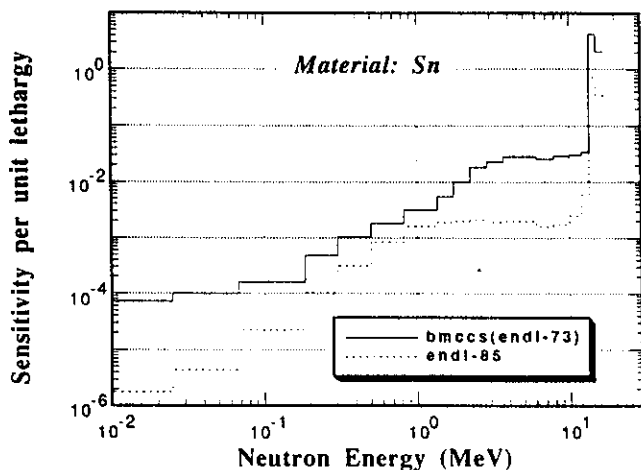Fig. 54. Gamma-ray kerma factors for tin as a function of energy for MCPLIB library.

Fig. 55. Nuclear heating sensitivity profile, $P_n^i(u)$, for tin as a function of neutron energy for ENDL-85, and BMCCS libraries.
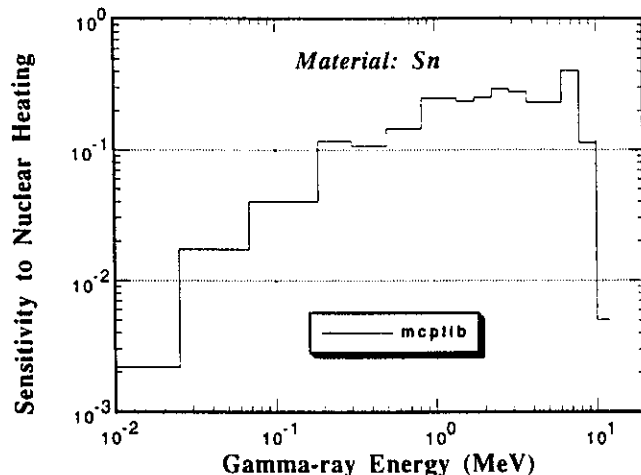

Fig. 56. Nuclear heating sensitivity profile, $P_g^j(u)$, for tin as a function of gamma-ray energy for MCPLIB library.

C, and D. During the period D, measurements were made for two geometric arrangements, as for graphite: (a) tungsten microcalorimeter kept close to the target without any surrounding enclosure (bare or without Li_2CO_3 enclosure), and (b) tungsten microcalorimeter enclosed within an annular enclosure made up of Li_2CO_3 and polyethylene, but such that there is no extraneous material between the target and the calorimeter (with Li_2CO_3 enclosure). Refer to earlier discussion for graphite probe for rationale behind use of Li_2CO_3 enclosure. As for tungsten, the change in nuclear heating was negligible due to this enclosure. As shown in Table VII, C/E's for tungsten range from 0.99 (JENDL-3) to 1.01 (MATXS10-heat/RMCCS/MATXS5-heat).

This closeness in C/E values masks the large differences in neutron kerma factors for different libraries. Photon heating is taken to be identical for all libraries. As shown in Table III, the neutron kerma factor integrals, from 14.92 to 13.5 MeV, for different libraries show large differences. These integrals range from 4.63×10^{-15} J·b (JENDL-3) to 6.43×10^{-15} J·b (RMCCS). In fact, the integrals over larger range (14.92 to 0.1 MeV), as provided in Table IV, show that the differences accentuate further. The neutron kerma factors are compared in Fig. 57 for ENDL-85, RMCCS, MATXS10-heat, MATXS10-kerma, and JENDL-3 libraries above 5 MeV. ENDL-85 and JENDL-3 kerma factors are close to one another. RMCCS, and MATXS10-heat kerma factors are close to each other, but lie much above ENDL-85 beyond 2 MeV. At 14 MeV, MATXS10-heat kerma is ~30% larger than ENDL-85 kerma. The largest difference in kerma factors is found around 7 MeV, where MATXS10-heat value is almost 4 times of ENDL-85 value! MATXS10-kerma values lie between the preceding two sets, but are closer to the ENDL-85 set.

The photon kerma factors are plotted in Fig. 58 for MCPLIB, MATXS10 and JENDL-3. There is large disagreement among the two libraries below 0.5 MeV, and above 9 MeV. The kerma factor integrals, over 10 to 0.1 MeV range, for the two libraries differ widely (see Table V). The MATXS10 KI_g is 27% larger than that for MCPLIB. The lowest photon kerma factor from MCPLIB is ~1.5×10^{-12} J·b for photon energy lying in the range of ~1.5 to ~0.5 MeV. It is to be compared to neutron kerma factor of ~5×10^{-14} J·b at 14 MeV. This clearly brings out the importance of photons to nuclear heating for tungsten. Comparing photon kerma factor integral for 10 MeV to 0.1 MeV range for MCPLIB (see Table V) to neutron kerma factor integral for 14.92 to 13.5 MeV (see Table III), for ENDL-85
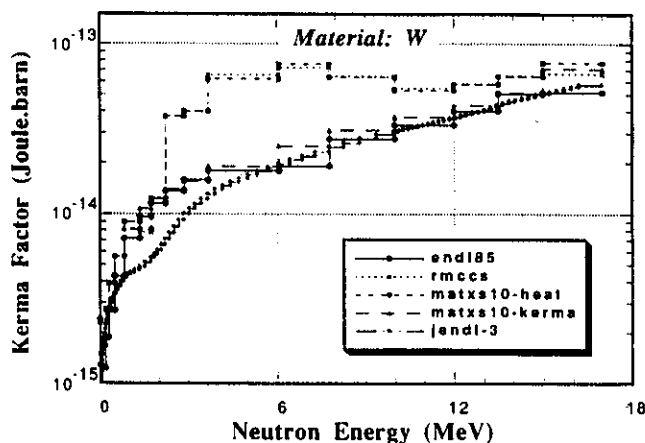

Fig. 57. Neutron kerma factors for tungsten as a function of energy for ENDL-85, RMCCS, MATXS10-heat, MATXS10-kerma, and JENDL-3 libraries.
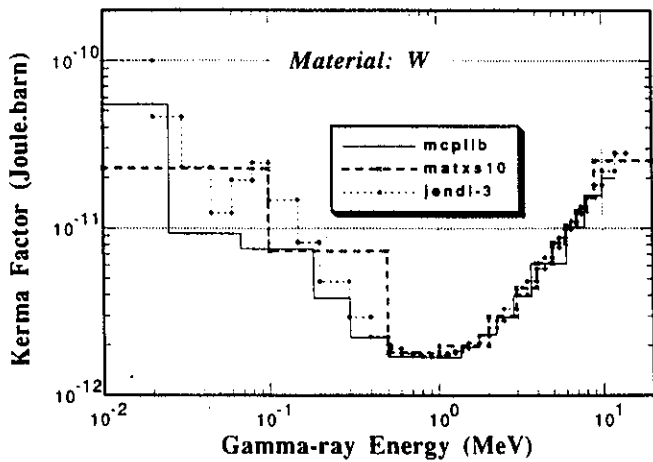
Fig. 58. Gamma-ray kerma factors for tungsten as a function of energy for MCPLIB, MATXS10, and JENDL-3 libraries.
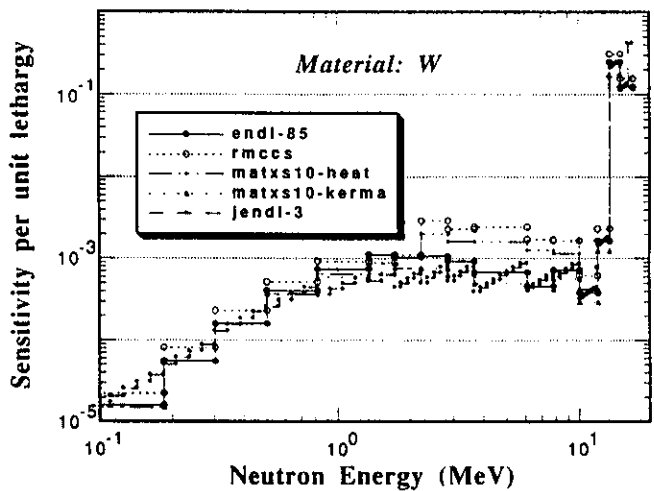

Fig. 59. Nuclear heating sensitivity profile, $P_n^j(u)$, for tungsten as a function of neutron energy for ENDL-85, RMCCS, MATXS10-heat, MATXS10-kerma, and JENDL-3 libraries.

library, one finds a huge ratio of 4291. It follows that photons will always contribute substantially to nuclear heating in a reasonably sized tungsten probe, even when incident field is somehow tailored to be 100% 14 MeV D-T neutrons! A reasonably sized probe will ensure that a great majority of the energetic electrons released in nuclear energy deposition process is absorbed in the probe itself for ensuring charged particle equilibrium (CPE) through most of the probe-volume. As range for even 1 MeV electrons in tungsten is 0.77 g/cm², a probe of tungsten at full theoretical density (19.3 g/cm³) will measure at least 2 mm a side. We assume here that there are no electrons above 1 MeV and that it is adequate to have a probe dimension 5 times the range to keep the violation of CPE to an acceptably low level. Compare a probe dimension of 2 mm to a 14 MeV neutron mean free path of ~50 mm in tungsten. Evidently, there is an appreciable probability of producing γ-rays even for a 2-mm-thick tungsten probe!

Figure 59 shows nuclear heating sensitivity profile, $P_n^j(u)$'s, for tungsten as a function of neutron energy for ENDL-85, RMCCS, MATXS10-heat, MATXS10-kerma and JENDL-3. Largest sensitivity, for ENDL-85, occurs for 15 to 13.5 MeV group, and is ~0.3 per unit lethargy. Sensitivity drops more than two orders as neutron energy drops to 10 MeV from 14 MeV. It has relatively flat value of ~10^{-3} per unit lethargy from 10 to ~0.8 MeV, and thereafter it comes down fast. RMCCS profile lies way above that with ENDL-85. Sensitivity profile for photon component of the nuclear heating, $P_g^j(u)$, is provided in Fig. 60 for MCPLIB and MATXS10. The largest γ-sensitivity, ~0.3 per unit lethargy, occurs between ~3 to ~4 MeV (for MCPLIB), and it is of the same order as largest neutron sensitivity, but it is ~300 times the neutron sensitivity in the flat response region. Thus, total nuclear heating for our experimental conditions is controlled by photons. This

Fig. 60. Nuclear heating sensitivity profile, $P_g^j(u)$, for tungsten as a function of gamma-ray energy for MCPLIB, and MATXS10 libraries.

is also supported by the fractional neutron heating values provided in Table VII, which show as low as 4 to 6% contribution to total heating from neutrons.

The preponderance of photon heating fraction in total heating in tungsten could be exploited to develop and calibrate a tungsten based calorimeter to obtain photon heating fraction of total heating in any other probe material subjected to D-T neutron field.

VI.I. Lead

Nuclear heating measurements were made with lead single probes during experimental period D. As shown

in Table VII, C/E's for lead range from 1.1 (ENDL-85/MATXS5-kerma) to 1.6 (RMCCS/BMCCS/ENDF5). This large variation is mostly attributable to large differences in neutron kerma factors for different libraries, as photon heating is taken to be identical. In fact, one can look at the fractional neutron heating rates for different libraries provided in Table VII. The libraries with the largest C/E's are those that have abnormally large neutron heating fractions. For example, BMCCS (C/E = 1.63), RMCCS (C/E = 1.60), and ENDF5 (C/E = 1.60), have rather large, fractional neutron heating values of 0.35, 0.34, and 0.34 respectively. On the other hand, ENDL-85, MATXS10-heat (C/E = 1.14), and MATXS10-kerma (C/E = 1.14) have low, fractional neutron heating values of 0.050, 0.059, and 0.059, respectively.

As shown in Table III, the neutron kerma factor integrals for different libraries show large differences-lowest value of 4.40×10^{-15} J·b for MATXS5-kerma, and largest value of 6.73×10^{-14} J·b for RMCCS. Neutron kerma factors are compared in Fig. 61 for ENDL-85, RMCCS, MATXS10-heat, MATXS5-heat, and JENDL-3 libraries. ENDL-85, MATXS10-heat, and JENDL-3 kerma factors are close to one another. RMCCS, and MATXS5-heat kerma factors show large deviations from the other three. Additionally, MATXS5-heat kerma factors are negative for many energy groups above 2 MeV. RMCCS kerma factors show oscillatory behavior above 2 MeV. RMCCS kerma factors are almost the largest above 10 MeV. Interestingly, RMCCS value peaks for 15 to 13.5 MeV group and decreases on either side of this group, and this peak value is more than an order larger than that for any other library.

The kerma factors for photons are shown in Fig. 62 for MCPLIB, and MATXS10. There is large disagree-
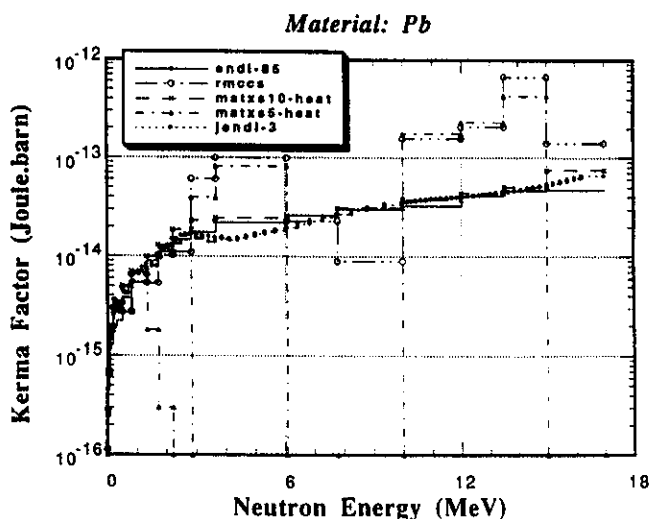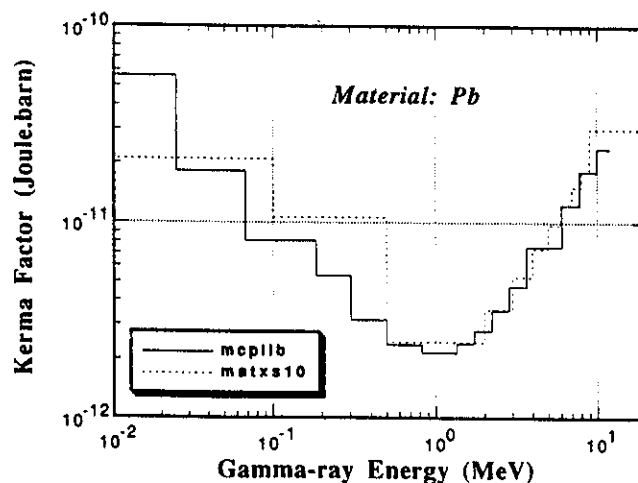
Fig. 62. Gamma-ray kerma factors for lead as a function of energy for MCPLIB, and MATXS10 libraries.

ment between the two libraries below 0.5 MeV and above 9 MeV. The kerma factor integrals, over 10 to 0.1 MeV range, for the two libraries differ widely (see Table V). The MATXS10 KI_g is 38% larger than that for MCPLIB. The lowest photon kerma factor from MCPLIB is $\sim 2 \times 10^{-12}$ J·b for photon energy lying in the range of ~ 1.5 to ~ 0.8 MeV. It is to be compared to neutron kerma factor of $\sim 5 \times 10^{-13}$ J·b at 14 MeV. This clearly brings out the importance of photons to nuclear heating for lead. Comparing photon kerma factor integral for 10 MeV to 0.1 MeV range for MCPLIB (see Table V) to neutron kerma factor integral for 14.92 to 13.5 MeV (see Table III), for MATXS10-heat library, one finds a ratio of 5122! It implies that photons will invariably make large contribution to nuclear heating in a finite-size lead probe.

Figure 63 shows nuclear heating sensitivity profile, $P_n^i(u)$'s, for lead as a function of neutron energy for ENDL-85, RMCCS, MATXS10-heat, MATXS5-heat and JENDL-3. Largest sensitivity occurs for 15 to 13.5 MeV group for ENDL-85 and MATXS10-heat and is ~ 0.3 per unit lethargy. Generally, sensitivity drops two to three orders as neutron energy drops to 10 MeV from 14 MeV. It has relatively flat value of $\sim 10^{-3}$ per unit lethargy from 10 to ~ 1 MeV, and thereafter it comes down fast. RMCCS and MATXS5-heat sensitivity profiles are driven by the oscillatory behaviors of their kerma factors. Sensitivity profile for photon component of the nuclear heating, $P_g^j(u)$, is provided in Fig. 64 for MCPLIB and MATXS10. The largest γ-sensitivity, ~ 0.2 per unit lethargy, occurs between ~ 0.5 to ~ 8 MeV (for MCPLIB), and it is of the same order as largest neutron sensitivity, but it is ~ 200 times the neutron sensitivity in the flat response region. In other words, total nuclear heating for our experimental conditions is largely dominated by photons. This is also

Fig. 61. Neutron kerma factors for lead as a function of energy for ENDL-85, RMCCS, MATXS10-heat, MATXS5-heat, and JENDL-3 libraries.

Fig. 63. Nuclear heating sensitivity profile, $P_n^j(u)$, for lead as a function of neutron energy for ENDL-85, RMCCS, MATXS10-heat, MATXS5-heat, and JENDL-3 libraries.
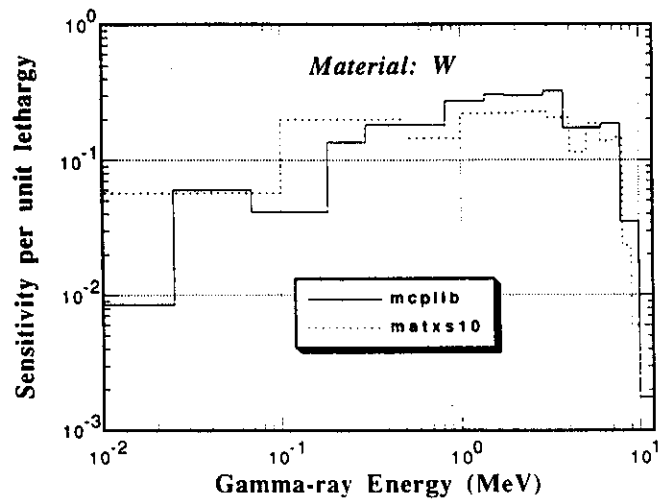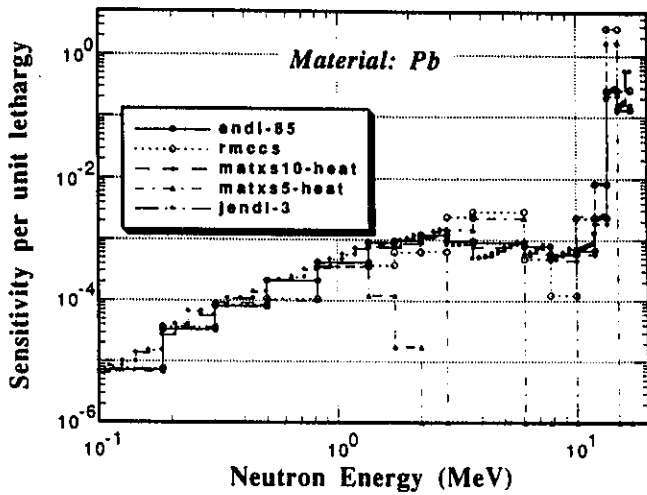

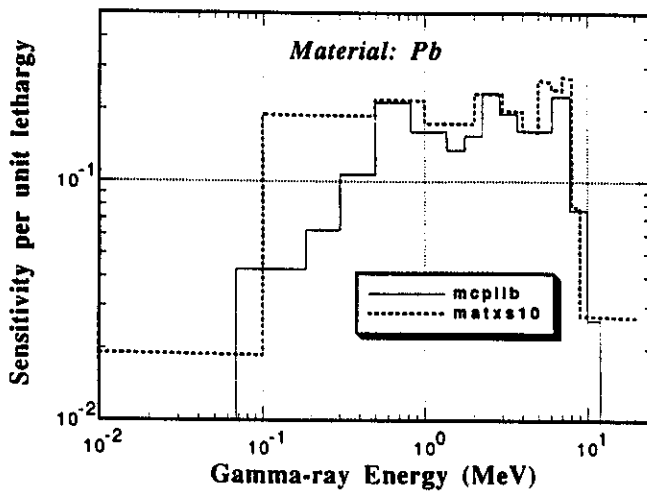
Fig. 64. Nuclear heating sensitivity profile, $P_g^j(u)$, for lead as a function of gamma-ray energy for MCPLIB, and MATXS10 libraries.

borne out by the fractional neutron heating values provided in Table VII, which show as low as ~6% contribution to total heating from neutrons (for MATXS10-heat).

VII. STATUS OF PREDICTION UNCERTAINTY

Let us look at the C/E results for various materials and libraries of the preceding section in the light of sensitivity estimation discussed earlier in Sec. V. We have used RMCCS spectra for neutrons and γ-rays

(photons) and kerma factors from MATXS10-heat library. Uncertainties on n and γ-spectra have been obtained using RMCCS and ENDL-85 spectra for the same experiment, wherever available, and using the procedure highlighted in Sec. V. Whenever we do not have these spectra, we calculate sensitivity estimates, $|\Delta H/H|_{max}$, using the uncertainty files for four reference experiments, namely, graphite, titanium, molybdenum, and tungsten, and retain the largest sensitivity estimate out of the four. The materials that fall under this category include: copper, zirconium, niobium, tin, and lead. Figure 65 shows prediction uncertainty in total nuclear heating, say, C/E − 1, for all the materials. The materials are arranged in the order of increasing Z, going from graphite (Z = 6) to lead (Z = 82). The figure shows results from ENDL-85, RMCCS, MATXS10-heat, MATXS10-kerma, JENDL-3, along with sensitivity estimate. Zirconium has the lowest sensitivity estimate, and lead has the largest estimate. It is to be noted that sensitivity estimates appear to satisfactorily explain the uncertainty predictions from most of the libraries for titanium, niobium, molybdenum, tin, tungsten, and lead. However, for graphite, copper, and zirconium, the uncertainty predictions are considerably larger than the sensitivity estimates. In the case of zirconium, the uncertainties on neutron kerma factors are expected to be much larger than those used (refer to Sec. V.C). As for graphite and copper, uncertainties on neutron kerma factors, and photon production cross sections may be much larger than those reflected in the sensitivity estimates, directly in neutron kerma factors for the former and indirectly in photon flux for

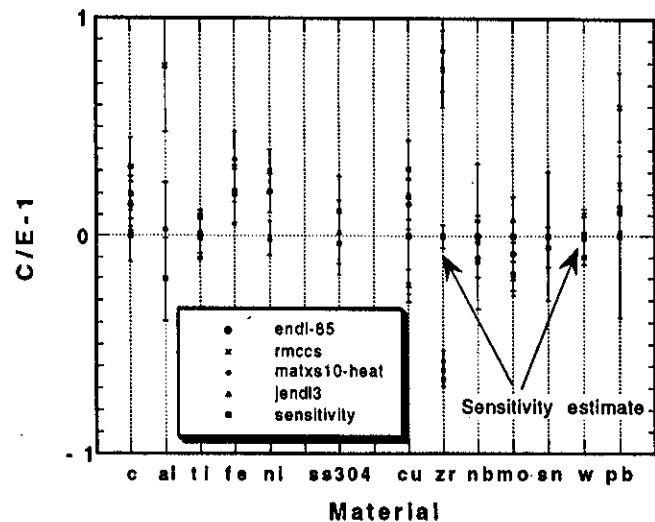Fig. 65. Prediction uncertainty in nuclear heating, expressed as C/E − 1, for various plasma-facing material probes subjected to D-T neutrons; materials include graphite, titanium, copper, zirconium, niobium, molybdenum, tin, tungsten, and lead; various libraries are included.

ever, there will be very little improvement for zirconium. In other words, both neutron kerma factors and photon production cross sections for zirconium need drastic improvement.

VIII. QUALITY FACTORS FOR NUCLEAR HEATING

It is clear from the previous sections that, in general, there is significant disagreement between calculation and the experimental measurement of total nuclear heating for almost all the materials covered in this work. Obviously, the calculated neutron and photon energy spectrum, the neutron kerma factors, and the photon kerma factors used in the nuclear heating calculations contribute to the disagreement. The inadequacies in radiation transport cross sections, photon production cross sections and geometrical/material modeling of the irradiated assembly, including the probe and its surroundings, are notable contributors to the uncertainties in the calculated neutron and photon energy spectra. In principle, it is possible to mitigate these inadequacies. However, the task of bringing out significant improvement in the whole range of neutron and photon kerma factors, and photon production cross sections requires enormous amount of effort spread over many years, as one has to patiently await availability of improved partial cross sections, and energy and angular distributions of recoiling nuclei, and emitted neutrons, photons, and light charged particles.

The designers of a fusion machine need reliable information on total nuclear heating in its various components. Entire range of neutron and photon energy spectra are involved in the heating calculations. The machine-component closest to the D-T plasma sees the hardest neutron spectrum; the one farthest from the plasma usually sees the softest spectrum. It is to be reminded that (n,γ)-reactions are preferably provoked by low-energy part of the neutron energy spectrum, unlike $(n,2n)$, (n,p), $(n,np/d)$, (n,t), (n,α) reactions that are preferably provoked by high-energy part of the spectrum. The neutron kerma factors fall rapidly as the neutron energy drops. Thus, most of the contribution to neutron component of total nuclear heating comes from hardest part of the spectrum. But, even a small fraction of low energy neutrons could lead to sizeable production of photons through (n,γ)-reaction, which might, in turn, lead to relatively significant amount of photon heating, even for a machine-component close to D-T plasma. The designers accept the inadequacies of modeling and the cross-section data and incorporate safety factors to come up with a somewhat conservative design.[43,44]

Sizable underprediction or overprediction of nuclear heating by calculation is undesirable due to its implications for large overheating or underheating of

affected structure. On the other hand, large underheating might be unacceptable in fusion machines that employ structural materials having high Ductile to Brittle Transition Temperature (DBTT), close to room temperature or higher. Ideally, one needs to correct the calculation, using a multiplier, such that the corrected prediction is equal to actual (experimental) amount of total nuclear heating. This correction factor for a code (and library) can be defined as

$$\text{ideal correction factor (ICF)} = 1/(C/E) = E/C \ ,$$

where inverse of observed C/E's defines correction factor for a given material. As long as one has access to very large amount of C/E data for each material, one can obtain the ICF and associated confidence level. The ICF can also be seen as a quality factor that is indicative of the quality of the ensemble of transport cross-sectional library, photon production cross sections, computed neutron and photon spectra, neutron and photon kerma factors, and experimental data.

In practice, it is almost impossible to obtain the ICF as defined above due to problems associated with (a) impossibility of exact modeling of the experimental assembly, (b) non-vanishing errors of the calculational method/code, and (c) finite experimental error. Thus, one will rather be dealing with a distribution of correction factors.[45] If this distribution is statistically reliable, one can set a confidence level and obtain a correction factor which, when multiplied to the calculated value, yields a corrected calculational result that will be equal to or greater than the experimental value for ensuring overprediction, or the reverse if underprediction of total nuclear heating will be required. We prefer to call such a multiplier as a quality factor.

The quality factor is a good indicator of the quality of the ensemble of the experimental data, the calculated neutron and photon spectra, and the kerma factor library. It is evident that the said quality factor will reduce to an ICF only when the associated probability distribution is a delta-function centered at the ICF; then the confidence level in such a quality factor is 100%. However, it is almost impossible to obtain a delta-function probability distribution of the quality factor (or correction factor). The realistic probability distributions could at best be Gaussian-like. The C/E results discussed in the preceding sections can be utilized directly to estimate quality factors for prediction of nuclear heating in each material. But, the associated confidence level in the estimated quality factor for a material may suffer due to limited number of neutron and photon energy spectra covered during measurements. In other words, such quality factors might change under different neutron and photon spectra. More reliable quality factors can be generated by conducting measurements under wide range of neutron and photon spectra.

At times, a designer may simply be interested in ascertaining general trends for a code/library, regarding its prediction capability of total nuclear heating in a given material. In this regard, in the following, we will be focusing on quality factors that ensure overprediction of total nuclear heating, rather than its underprediction. In what follows, we have attempted to discern some collective and individual trends for all the kerma factor libraries used in the present work. In principle, we can introduce two kinds of quality factors: (a) Materialwise quality factor can be associated with a given material, where available C/E data on that particular material from all libraries is utilized to get probability density distribution of C/E's, (b) Librarywise quality factor can be associated with a given library, where available C/E data for all probe materials, and that particular library is used to obtain probability density distribution of C/E's. For either type of quality factor, we first obtain a normalized distribution of C/E data in C/E bins spanned over 0 to infinity, such that, when summed over the entire C/E range, one obtains unity.[45] Errors associated with each C/E data are duly factored in to obtain this normalized C/E distribution. Widths of each C/E bin are then used to obtain probability density distribution of C/E's.

First of all, let us look at shape of a consolidated probability density distribution of C/E's. This distribution is obtained from all the C/E data provided in Table VII, irrespective of material or library.[45] Figure 66 shows a plot of this consolidated probability density distribution. Also plotted alongside is a Gaussian distribution. This Gaussian distribution is obtained such that (a) C/E of its peak is same as that of the peak in the actual distribution, (b) its full width at half maximum (FWHM) is same as that of the peak in the actual distribution. The latter condition leads to obtention

of the standard deviation of the Gaussian distribution. The total number of C/E data points is 89. The peak and standard deviation of the Gaussian distribution are 1.04 and 0.23, respectively. Though the actual probability density distribution is remarkably similar to the Gaussian distribution, one can observe significant differences in the two on either side of the peak. On lower end of C/E's, one can, in fact, notice a secondary peak in C/E range of 0.4 to 0.5. Zirconium and, to some extent, titanium contribute predominantly to this secondary peak. On higher end of C/E's, one notices rising discrepancy between the two distributions beyond 1.5. Lead, zirconium, and to some extent, copper and titanium, contribute to this discrepancy. Notice that the actual density distribution in Fig. 66 is subject to large uncertainties due to limited number of C/E data used in getting this distribution. However, all the qualitative observations made above are perfectly valid. Figure 67 shows fractional confidence level as a function of quality factor for all the materials and kerma factor libraries taken together. This figure is based on actual consolidated probability density distribution shown in Fig. 66. One can observe an error bar (one standard deviation) associated with each confidence level. This is directly related to the limited number of C/E data points used, as already pointed out earlier. The maximum possible confidence level is unity. It is clear from the figure that we would need to include many more C/E data points if we desired to go beyond a confidence level of ~80 to 100%. Already, the quality factor is close to 3 for ~80 to 100% confidence level! In other words, if we took any of the eleven kerma factor libraries used for any of the nine plasma-facing materials, we would need to multiply the calculated total nuclear heating rate by a factor of 3 to have ~80 to 100% confidence level so that the modified calculated
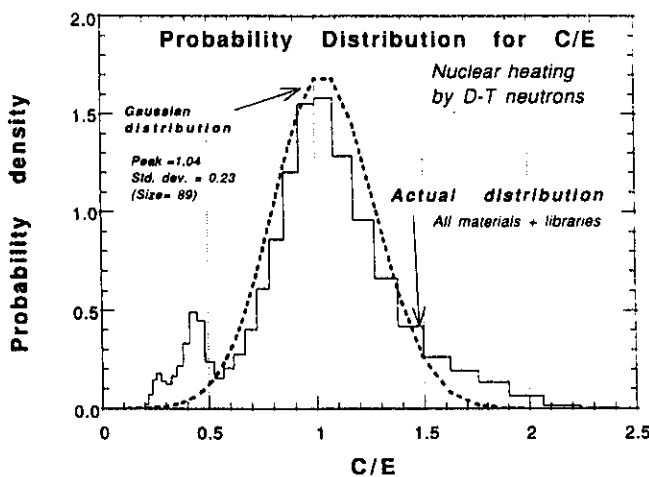

Fig. 66. Consolidated probability density distribution of C/E's, for nuclear heating produced by D-T neutrons, for all materials and kerma factor libraries.
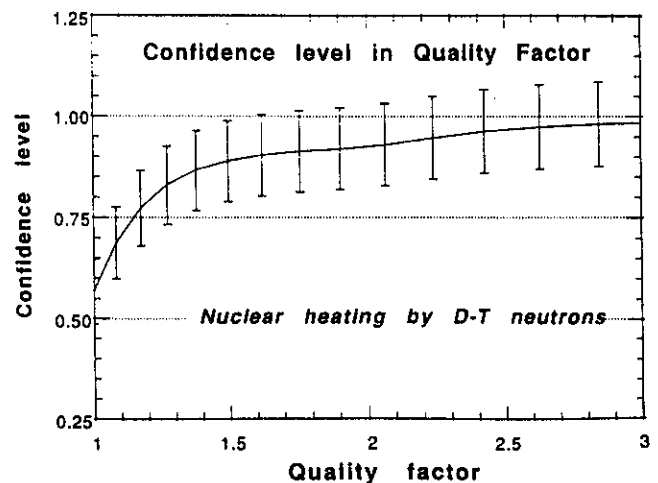

Fig. 67. Fractional confidence level, and associated uncertainty, as a function of a quality factor, using consolidated probability density distribution of C/E's.

heating rate does not fall below the actual heating rate in that particular material.

VIII.A. Materialwise Quality Factors

Even though, the materialwise probability density distributions carry large uncertainty due to few C/E data points, it is still very informative to study these distributions to assess current status for each material.[45] Table VIII summarizes conclusions of the statistical analysis based on materialwise probability density distributions for all nine materials. The mean C/E's range from 0.43 (zirconium) to 1.22 (graphite/copper). For zirconium, there are two groups of C/E's, larger set (7 members) peaks around 0.4, and the smaller set (4 members) peaks around 1.8. In the results included in the table, the larger set dominates. However, if one were to take a simple mean and standard deviation of a single set of all 11 points, one would, instead, get respective values of 1.07 and 0.75. For tin, only 3 C/E data points are available. As a result, one needs to be very careful while using these numbers. Table VIII also shows a quality factor for 90% confidence level for each material. This number needs to be accepted with caution due to scanty C/E data. Figure 68 shows fractional confidence levels for graphite, molybdenum, tungsten, and lead. It is clear that for any confidence level above 90%, the quality factors will have the following ascending order: graphite, lead, tungsten, and molybdenum. As seen from Table VIII, the quality factors range from 1.0 to 3.3. Qualitatively speaking, graphite and lead have quality factor of unity. In other words, no correction of computed heating rates is
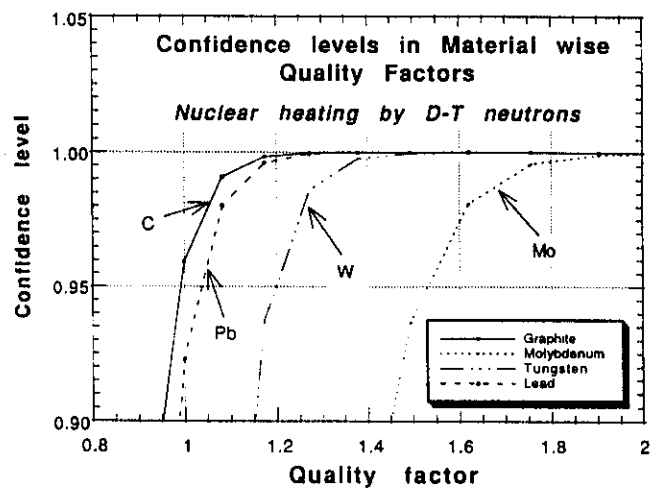

Fig. 68. Materialwise fractional confidence levels as a function of quality factor, for graphite, molybdenum, tungsten, and lead, using individual probability density distributions for each material.

needed for ensuring overprediction of the total heating rates with a confidence level of 90%, if one were not to know which of the eleven kerma factor libraries is used. Zirconium, obviously, qualifies for largest quality factor of 3.3!

VIII.B. Librarywise Quality Factors

Table IX summarizes conclusions of the statistical analysis based on librarywise probability density

TABLE VIII

Materialwise Conclusions from Statistical Analysis of C/E Results by Different Libraries for Nuclear Heating

Item	Probe Material								
	Graphite	Titanium	Copper	Zirconium	Niobium	Molybdenum	Tin	Tungsten	Lead
Number of C/E results used (N)	11	11	11	11	11	11	3	9	11
Mean (m)	1.22	1.04	1.22	0.43[a] (1.07)[b]	0.96	0.89	1.04[c]	1.04	1.13
Standard deviation (σ)	0.13	0.14	0.18	0.05[a] (0.75)[b]	0.14	0.12	0.10[c]	0.11	0.12
Quality factor — a conservative estimate[d]	1.0	1.7	1.3	3.3[a]	1.3	1.5	1.2[c]	1.2	1.0

[a]Both m and σ for zirconium might appear misleading, but they have to be seen in the light of two groups of C/E results. The numbers here reflect the C/E-group lying below unity.
[b]The bracketed numbers have been obtained by usual method of obtaining m and σ from a set of numbers.
[c]Results to be taken with extreme caution.
[d]Quality factor has been defined for 90% confidence level. However, due to only limited number of C/E data being available from Table VII, a more realistic quality factor will be larger than the one provided in this table.

TABLE IX

Librarywise Conclusions from Statistical Analysis of C/E Results for Nuclear Heating

	Response Function Library Used for Calculation of Neutron Heating[a]					
Item	ENDL-85	MATXS10 'Heat'	MATXS10 'Kerma'	MATXS5 'Heat'	MATXS5 'Kerma'	JENDL-3
Number of C/E results used (N)	9	8	8	8	8	8
Mean (m)	0.96	1.13	1.13	1.04	1.04	1.04
Standard deviation (σ)	0.19	0.19	0.20	0.29	0.29	0.16
Quality factor — a conservative estimate[b]	2.6	1.4	2.1	1.4	2.1	2.2

[a]Gamma-heating calculated with MCNP γ kerma factor library, MCPLIB, was added to neutron heating calculated with other libraries to get total nuclear heating.

[b]Quality factor has been defined for 90% confidence level. However, due to only limited number of C/E data being available from Table VII, a more realistic quality factor will be larger than the one provided in this table.

distributions for only six kerma factor libraries, namely, ENDL-85, MATXS10-heat, MATXS10-kerma, MATXS5-heat, MATXS5-kerma, and JENDL-3. The mean C/E's range from 0.96 (ENDL-85) to 1.13 (MATXS10). Even though MATXS5, 'heat' as well 'kerma', and JENDL-3 have same mean of 1.04, the standard deviation is almost a factor of 2 smaller for JENDL-3. In fact, JENDL-3 yields the smallest standard deviation. Table IX also shows a quality factor for 90% confidence level for each library. Figure 69 shows fractional confidence levels for ENDL-85, MATXS10-heat, and JENDL-3. It is obvious that for any confidence level above 90%, the quality factors will have the following ascending order: MATXS10-heat, JENDL-3, and ENDL-85. As provided in Table IX, the quality factors range from 1.4 to 2.6. The lowest quality factor

of 1.4 applies both to MATXS10-heat and MATXS5-heat. This means that if one were to use either of these two libraries for any of the nine materials, the calculated heating rate would have to be multiplied by 1.4 to ensure that the modified heating rate carries 90% confidence level. Largest quality factor of 2.6 is obtained for ENDL-85. Very low C/E (0.34) for zirconium by ENDL-85 is largely responsible for such a high quality factor for ENDL-85.

IX. RECOMMENDATIONS

In view of significantly large discrepancies observed between calculations and the experimentally measured nuclear heating rates, it is evident that a lot of work needs to be undertaken, both in area of neutron kerma factor and photon production cross-section evaluation and the experimental measurement of the nuclear heating. Transport cross sections, and spectrum weighting functions, and spectrum calculation methods need to be improved too for bringing the discrepancies between the calculations and the measurements under control.

Large C/E discrepancies have been observed for all materials except tungsten. It is to be remembered that these discrepancies have been observed for very hard neutron energy spectrum. For larger span of neutron energy spectrum, it is highly probable that C/E-range will expand too. Thus the observed discrepancies are only indicative of the problems that lie ahead. New materials are also likely to be added to this list as the experimentation and the analysis is further strengthened in future. The future experimental work should continue on all the materials covered in the present work if one desires smaller quality factors and larger confidence levels at the same time.

The following suggestions are recommended to be implemented for enhancing the effectiveness and the quality of the future work:
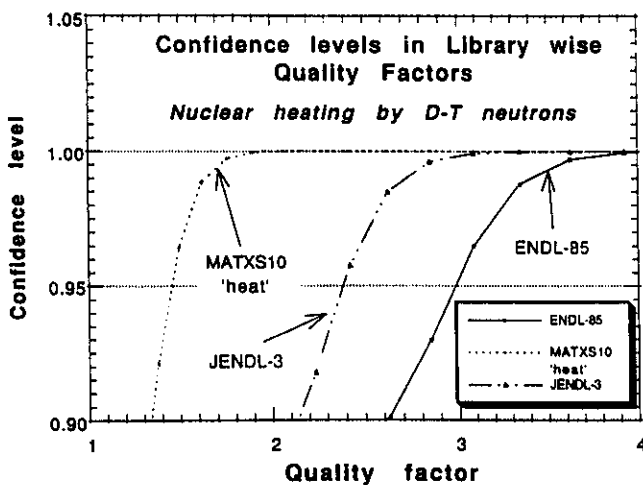

Fig. 69. Librarywise fractional confidence levels as a function of quality factor, for ENDL-85, MATXS10-heat, and JENDL-3, using individual probability density distributions for each library.

1. There is a need to have a unique and complete transport cross-section and kerma factor library, using most recent and available cross-section data. This library should also have associated uncertainty levels on total cross sections, secondary particle (neutron/photon) energy and angular distributions, and neutron and photon kerma factors. The evaluators can develop a materialwise priority list so as to make best possible use of the available resources.

2. Very fine energy group structure should be adopted for this library. A reasonable compromise for the total number of energy groups may be somewhere near 200.

3. There is a need to perform nuclear heating experiments for all the materials under a large number of neutron and photon energy spectra. The net accuracy of the experimental measurements needs to be better than 5%, a factor of 2 improvement over the average level attained in the measurements covered in this work. This will help in checking the validity of this library over large neutron energy range with raised confidence.

4. It will be highly desirable to develop and calibrate graphite as a neutron heating sensitive probe and tungsten as a photon heating sensitive probe for eventually getting separate estimations of neutron and photon heating rates in various probe materials. This will be very helpful in obtaining more reliable quality factors, on one hand, and improving selected parts of the nuclear data library, on the other hand.

X. SUMMARY AND CONCLUSIONS

Direct nuclear heat deposition rate measurements done using microcalorimetric technique in single probes of graphite, titanium, copper, zirconium, niobium, molybdenum, tin, tungsten, and lead have been discussed along with their analysis using various kerma factor libraries. These measurements were carried out under U.S. DOE/JAERI collaborative program during 1989 through 1992. Temperature-change rates as low as $30 \mu K/s$ have been measured. Heat deposition rates as low as $35 \mu W/g$ have been measured. Thermistors and RTD's have generally provided matching experimental results. The point-sized bead thermistors used in the present experiments have opened up a whole range of possibilities for their extensive use to obtain nuclear heat deposition rates within thin material zones too.

Analysis of the measured data for single probes of all nine materials was done using neutron and photon spectra obtained from MCNP using RMCCS cross-section library, and eleven kerma factor libraries including BMCCS, ENDL-85, RMCCS, ENDFB5, MATXS10-heat, MATXS10-kerma, MATXS5-heat, MATXS5-kerma, KAOSLIB-rec, KAOSLIB-rec+cpd, and JENDL-3. Except for tungsten, all other materials have large C/E spreads. Sensitivity profiles for neutrons and photons were also obtained for all the nine

materials. In addition, neutron and photon kerma factors from different libraries were compared. The kerma factor integrals over various energy ranges were also defined and tabulated. Large discrepancies were observed for neutron kerma factors for all the nine materials. We have also seen differences in kerma factors for photons from different libraries. Significant differences in photon kerma factors were seen below ~0.5 MeV. Also, the discrepancy in photon kerma factor integrals increased as a function of Z of the probe material.

Upper limits of sensitivity estimates were obtained for all materials using the respective sensitivity profiles and the uncertainty files. Smallest and largest estimates were found for zirconium and lead, respectively. The sensitivity estimates were found adequate for covering prediction uncertainty spread, from various libraries, for titanium, niobium, molybdenum, and tungsten. For graphite, copper, and lead, the situation agreement would become acceptable if one were to take three times the sensitivity estimate for covering the prediction uncertainty. For tin, the improvement is seen right away if BMCCS library is dropped. For zirconium, there is no way to improve the agreement unless uncertainties on kerma factors and neutron/photon spectra were raised drastically. In fact, the neutron kerma factors from various libraries were already shown to carry large uncertainties for zirconium.

From a reactor designer standpoint, it is important to know which library is most suitable for doing nucleonic design of a fusion reactor. The designer will like to make sure that nuclear heating rates are predicted accurately enough so that the fusion reactor structural materials operate within a temperature window extending from DBTT to melting point. Conventionally, the designers have only worried about not exceeding the melting point of the structure, and they have incorporated engineering safety factors to ensure that the calculated numbers can assure overprediction of nuclear heating. In the present work, an attempt has been made to outline an approach to define a confidence level with a quality factor for total nuclear heating, employing the C/E results discussed in this work. The quality factor defined in this work is akin to the conventional engineering safety factor, but differs from it sharply due to the former applying only to the limited set of parameter space covered in our experimental work. This parameter space includes neutron spectrum, photon spectrum, neutron and photon transport library, neutron and photon kerma factors. It is also pointed out that a given confidence level generally carries an uncertainty. Quality factors for total nuclear heating have been defined. Two kinds of quality factors have been defined and discussed: materialwise and librarywise. Materialwise, quality factor is lowest for graphite, just 1.0, and largest for zirconium, say, 3.3, for a 90% confidence level. As for libraries, lowest quality of 1.4 applies to MATXS10-heat, and the largest one, say, 2.6, for ENDL-85, for 90% confidence level.

More experimentation is required to further improve the experimental accuracy obtained, on one hand, and accumulate more data on various probe materials, on the other. This two-pronged approach will enable us to mitigate the concerns emanating from lack of testing of the computed kerma factors and related methodologies[3-11] and assumptions, apart from neutron and photon cross-section libraries for particle transport.

A number of recommendations have been made for directing the future effort in the areas of nuclear heating measurements and analyses for maximizing the resultant gains. Strong international coordination will be needed to sincerely implement these recommendations.

REFERENCES

1. M. A. ABDOU and C. W. MAYNARD, "Calculational Methods for Nuclear Heating—Part I: Theoretical and Computational Algorithms," *Nucl. Sci. Eng.*, 56, 360 (1975).

2. M. A. ABDOU and C. W. MAYNARD, "Calculational Methods for Nuclear Heating—Part II: Applications to Fusion-Reactor Blankets and Shields," *Nucl. Sci. Eng.*, 56, 381 (1975).

3. M. A. ABDOU, C. W. MAYNARD, and R. Q. WRIGHT, "MACK: A Computer Program to Calculate Neutron Energy Release Parameters (Fluence-to-Kerma Factors) and Multigroup Reaction Cross Sections from Nuclear Data in ENDF Format," ORNL-TM-3994, Oak Ridge National Laboratory (July 1973).

4. Y. FARAWILA, Y. GOHAR, and C. MAYNARD, "KAOS-V Code: An Evaluation Tool for Neutron Kerma Factors and Other Nuclear Responses," ANL/FPP/TM-240, Argonne National Laboratory (Sep. 1989); see also Y. FARAWILA, Y. GOHAR, and C. MAYNARD, "KAOS/LIB-V: A Library of Nuclear Response Functions Generated by KAOS-V Code from ENDF/B-V and other Data Files," ANL/FPP/TM-241, Argonne National Laboratory (Apr. 1989).

5. R. E. MacFARLANE, D. W. MUIR, and R. M. BOICOURT, "The NJOY Nuclear Data Processing System, Vol. II: The NJOY, RECONR, BROADR, HEATR, and THERMR Modules," LA-9303-M, Los Alamos National Laboratory (May 1982).

6. R. S. CASWELL and J. J. COYNE, "Kerma Factors for Neutron Energies Below 30 MeV," *Radiat. Res.*, 83, 217 (1980).

7. R. J. HOWERTON, "Calculated Neutron Kerma Factors Based on the LLNL ENDL Data File," UCRL-50400, Vol. 27, Lawrence Livermore National Laboratory (Jan. 1986).

8. P. D. SORAN and R. E. SEAMON, "Graphs of the Cross Sections in the Recommended Monte Carlo Cross-Section Library at the Los Alamos Scientific Laboratory," 8374-MS, Los Alamos National Laboratory (May 1980).

9. H. M. FISCHER, "A Nuclear Cross Section Data Handbook," LA-11711-M, Los Alamos National Laboratory (Dec. 1989).

10. S. R. DOMEN, "Advances in Calorimetry for Radiation Dosimetry," *The Dosimetry of Ionizing Radiation*, Vol. II, p. 245, K. R. KASE, B. E. BJARNGARD, and F. H. ATTIX, Eds., Academic Press, Inc., Orlando (1987).

11. S. R. GUNN, " Radiocalorimetric Calorimetry: A Review," *Nucl. Instrum. Methods*, 29, 1 (1964); see also *Nucl. Instrum. Methods*, 85, 285 (1970); see also *Nucl. Instrum. Methods*, 135, 251 (1976).

12. S. R. DOMEN and P. J. LAMPERTI, "A Heat-Loss-Compensated Calorimeter: Theory, Design, and Performance," *J. Res. Natl. Bur. Stand.*, 78A, 5, 595 (1974).

13. J. S. LAUGHLIN and S. GENNA, "Calorimetry," *Radiation Dosimetry*, Vol. II, p. 380, F. H. ATTIX and W. C. ROESCH, Eds., Academic Press, Inc., New York (1966).

14. J. C. MCDONALD, I-CHANG MA, B. J. MIJNHEER, and H. ZOETELIEF, "Calorimetric and Ionimetric Dosimetry Intercomparisons II; d+T Neutron Source at the Antoni Van Leeuwenhoek Hospital," *Med. Phys.*, 8, 1 (1981).

15. Y. I. ALEKSENKO, G. V. MUKHIMA, L. P. ROKHLOVA, and V. A. KHRAMCHENKOV, "The Use of Quasi-Adiabatic Calorimeters for Interreactor Dosimetry," *At. Energ.*, 26, 328 (1969).

16. A. W. BOYD and A. KEDDAR, "Intercomparison of Reactor Calorimeters," *At. Energy Rev.*, 8, 949 (1970).

17. R. M. CARROLL, R. B. PEREZ, and O. SISMAN, "Measurements of Nonfission Heating in a High Neutron Flux Reactor," *Nucl. Sci. Eng.*, 36, 232 (1969).

18. F. H. ATTIX, *Introduction to Radiological Physics and Radiation Dosimetry*, John Wiley & Sons, New York (1986).

19. A. KUMAR, M. A. ABDOU, Y. IKEDA, and C. KONNO, "Radioactivity and Nuclear Heating Measurements for Fusion Applications," *Fusion Technol. 1990*, p. 872, B. E. KEEN, M. HUGUET, R. HEMSWORTH, Eds., Elsevier Science Publishers B.V. (1991).

20. A. KUMAR, Y. IKEDA, and C. KONNO, "Experimental Measurements and Analysis of Nuclear Heat Deposition Rates in Simulated D-T Neutron Environment: JAERI/US-DOE Collaborative Program on Fusion Neutronics Experiments," *Fusion Technol.*, 19, 1979 (1991).

21. A. KUMAR, M. Z. YOUSSEF, M. A. ABDOU, Y. IKEDA, C. KONNO, K. KOSAKO, Y. OYAMA, and T. NAKAMURA, "Direct Nuclear Heating Measurements in Fusion Neutron Environment and Analysis," *Fusion Eng. Des.*, **18**, 397 (1991).

22. Y. IKEDA, C. KONNO, K. KOSAKO, Y. OYAMA, F. MAEKAWA, H. MAEKAWA, A. KUMAR, M. Z. YOUS-SEF, and M. A. ABDOU, "Measurement and Analysis of Nuclear Heat Depositions in Structural Materials Induced by D-T Neutrons," *Fusion Technol.*, **21**, 2190 (1992).

23. A. KUMAR, M. A. ABDOU, M. Z. YOUSSEF, Y. IKEDA, C. KONNO, K. KOSAKO, Y. OYAMA, T. NAKAMURA, and H. MAEKAWA, "Salient Features of Induced Radioactivity and Nuclear Heating Measurements and Analysis," *Proc. Int. Workshop on Fusion Neutronics*, Karlsruhe, Germany, June 7, 1991, p. 68 (1991).

24. "MCNP—A General Monte Carlo Code for Neutron and Photon Transport: Version 3A," LA-7396-M, Rev. 2, J. F. BREISMEISTER, Ed., Los Alamos National Laboratory (Sep. 1988).

25. R. E. SEAMON, Los Alamos National Laboratory, Private Communication (Dec. 1990).

26. R. LITTLE and R. SEAMON, "Negative Heating Numbers," Los Alamos National Laboratory, Memorandum to P. YOUNG and E. ARTHUR, CSEWG Evaluations Committee (June 17, 1981).

27. R. E. MacFARLANE, "Energy Balance of ENDF/B-V," *Trans. Am. Nucl. Soc.*, **33**, 681 (1979).

28. Y. S. TOULOUKIAN and E. H. BUYCO, "Specific Heat: Metallic Elements and Alloys," *Thermophysical Properties of Matter*, Vol. 4, IFI/Plenum, New York (1970); see also Y. S. TOULOUKIAN and E. H. BUYCO, "Specific Heat: Nonmetallic Solids," *Thermophysical Properties of Matter*, Vol. 5, IFI/Plenum, New York (1970).

29. R. E. MacFARLANE, "TRANSX-CTR: A Guide for Interfacing MATXS Cross-section Libraries to Nuclear Transport Codes for Fusion Systems Analysis," LA-9863-MS, Los Alamos National Laboratory (Feb. 1984).

30. R. E. MacFARLANE, Los Alamos National Laboratory, Private Communication (Oct. 1993).

31. K. SHIBATA et al., "Japanese Evaluated Nuclear Data Library, Version-3," JAERI-1319, Japan Atomic Energy Research Institute (1990).

32. K. MAKI, K. KOSAKO, Y. SEKI, and H. KAWASAKI, "Nuclear Group Constant Set FUSION-J3 for Fusion Reactor Nuclear Calculations Based on JENDL-3," JAERI-M91-072, Japan Atomic Energy Research Institute (1991).

33. R. W. ROUSSIN, J. R. KNIGHT, J. H. HUBBELL, and R. J. HOWERTON, "Description of DLC99/HUGO Package of Photon Interaction Data in ENDF/B-V For-mat," ORNL/RSIC-46 (ENDF-335), Oak Ridge National Laboratory (1983).

34. S. A. W. GERSTL, D. J. DUDZIAK, and D. W. MUIR, "Cross-Section Sensitivity and Uncertainty Analysis with Application to a Fusion Reactor," *Nucl. Sci. Eng.*, **62**, 137 (1977).

35. D. W. MUIR, "COVFILS-2: Neutron Data and Covariances for Sensitivity and Uncertainty Analysis," *Fusion Technol.*, **10**, 1461 (1986).

36. P. G. YOUNG, J. W. DAVIDSON, and D. W. MUIR, "Evaluation of the ^{7}Li$(n,n't)^4$He Cross Section for ENDF/B-VI and Application to Uncertainty Analysis," *Fusion Technol.*, **15**, 440 (1989).

37. D. W. MUIR, "Review of Uncertainties in the Results of Nuclear Model Calculations," *Proc. Computation and Analysis of Nuclear Data Relevant to Nuclear Energy and Safety*, Trieste, Italy, February 10–March 13, 1992, M. K. MEHTA and J. J. SCHMIDT, Eds., World Scientific Publishing Company (Mar. 1993).

38. D. W. MUIR, "ENDF-6 File 30: Data Covariances Obtained from Parameter Covariances and Sensitivities," *Proc. OECD Seminar-Workshop on NJOY and THEMIS and the NEA Data Bank*, Paris, France, June 20–21, 1989, p. 91, CONF-8906162, Nuclear Energy Agency (1989).

39. P. M. SONG, M. Z. YOUSSEF, and M. A. ABDOU, "A New Approach and Computational Algorithm for Sensitivity/Uncertainty Analysis for SED and SAD with Application to Beryllium Integral Experiments," *Nucl. Sci. Eng.*, **113**, 339 (1993).

40. Y. IKEDA and M. Z. YOUSSEF, "Two-Dimensional Cross-Section Sensitivity and Uncertainty Analysis for Tritium Production Rate in Fusion-Oriented Integral Experiments," *Fusion Technol.*, **13**, 616 (1988).

41. M. Z. YOUSSEF, "Status of Methods, Codes and Applications for Sensitivity and Uncertainty Analysis," *Fusion Technol.*, **8**, 1552 (1985).

42. A. HOGENBIRK, "Energy Self-Shielding and SED/SAD Effects in Sensitivity Calculations of a NET Shielding Blanket," *Fusion Eng. Des.*, **18**, 331 (1991).

43. M. E. SAWAN and L. A. EL-GUEBALY, "Three-Dimensional Neutronics Analysis for the U.S. Magnet Shield of ITER," *Fusion Technol.*, **19**, 1469 (1991).

44. L. A. EL-GUEBALY, "Overview of the US-ITER Magnet Shield: Concept and Problems," *Fusion Technol.*, **19**, 1475 (1991).

45. A. KUMAR and Y. IKEDA, "On Disagreement Between Measurements and Calculations of D-T Neutron Driven Induced Radioactivity and Nuclear Heating," *Proc. Int. Conf. Nuclear Data for Science and Technology*, Gatlinburg, Tennessee, May 9–13, 1994, p. 883, American Nuclear Society (1994).

Anil Kumar (PhD, University of Bombay, India, 1981) is senior development engineer at the University of California, Los Angeles (UCLA). His current research interests include fusion reactor nucleonics experiments and analysis, technique development for nuclear heating, decay heat measurements, biological dose, fusion diagnostics, safety factor methodology for fusion reactor design parameters, low-activation materials, inertial confinement fusion, and sequential reactions. He has conducted experiments at leading facilities such as the Fusion Neutronics Source (FNS) facility in Japan, the Tokamak Fusion Test Reactor (TFTR) at Princeton University, and LOTUS in Switzerland.

Yujiro Ikeda (PhD, nuclear engineering, Nagoya University, Japan, 1981) is head of the Fusion Neutronics Laboratory in the Department of Reactor Engineering at the Japan Atomic Energy Research Institute (JAERI). He has worked in the areas of fusion neutronics experiments, induced radioactivity experiment and analysis, direct nuclear heating measurements, activation cross-section measurements, and fusion dosimetry.

Mohamed A. Abdou is a professor in the Department of Mechanical, Aerospace, and Nuclear Engineering at UCLA and also is the director of fusion technology at UCLA. His research interests include neutronics, thermomechanics, fusion technology, and reactor design and analysis. He served as the U.S. leader of the JAERI/U.S. Department of Energy (DOE) collaboration on fusion blanket neutronics.

Mahmoud Z. Youssef (PhD, nuclear engineering, University of Wisconsin, 1980) is a senior research engineer in the Department of Mechanical, Aerospace, and Nuclear Engineering at UCLA. He participated in several conceptual magnetic fusion energy and inertial fusion energy reactor design studies with emphasis on nuclear analysis and blanket/shield design. His research interests are in the areas of blanket/shield design optimization, nuclear data, sensitivity/uncertainty studies, neutronics methods and code development, tritium fuel cycle, radioactivity and safety aspects of fusion, integral experiments, neutronics testing, and research and development for fusion reactors, particularly the International Thermonuclear Experimental Reactor (ITER).

Chikara Konno (MS, physics, Kyoto University, Japan, 1985) is a research scientist in the Department of Reactor Engineering at JAERI. He has worked in the areas of fusion neutronics experiments, cross-section measurements, and neutron spectrum measurements using a proton-recoil counter.

Kazuaki Kosako (BE, atomic engineering, Tokai University, Japan, 1984) has worked at Sumitomo Atomic Energy Industries since 1994. He worked in the Department of Reactor Engineering at JAERI from 1984 to 1992 where he was involved mainly in fusion neutronics. He is currently interested in the area of radiation damage of materials.

Yukio Oyama (BS, physics, 1975; MS, nuclear physics, 1977; and Dr. Eng., 1989, Osaka University, Japan) is a principal scientist at JAERI. He has worked in the area of fusion neutronics experiments since 1978. He is currently involved in intense and high-energy neutron source projects.

Tomoo Nakamura (BS, physics, Kyoto University, Japan, 1957) is currently director of the Public Acceptance Database Center, Research Organization for Information Science and Technology. His research background includes experimental reactor physics on fast breeder reactors and nuclear technology on fusion reactor blankets. He served as the former Japanese leader of the JAERI/U.S. DOE collaboration on fusion blanket neutronics.

Hiroshi Maekawa (BE, 1965; MS, 1967; and Dr. Eng., 1970, nuclear engineering, Tokyo Institute of Technology, Japan) is the deputy director of the Department of Reactor Engineering and the head of the Intense Neutron Source Laboratory at JAERI. He has worked on fusion neutronics for more than 20 years, and he planned and constructed the FNS facility. He served as the Japanese leader of the JAERI/U.S. DOE collaboration on fusion blanket neutronics. His recent research has focused on International Fusion Materials Irradiation Facility conceptual design activities.